DOT/FAA/AR-xx/xx

Federal Aviation Administration
William J. Hughes Technical Center
Aviation Research Division
Atlantic City International Airport
New Jersey 08405

The FAA's Center of Excellence for UAS Research
ASSURE
Alliance for System Safety of UAS through Research Excellence

Annex B to Task A17: NIAR/WSU sUAS Numerical Model Validation (Component and Full-Scale Level) for Engine Ingestion Analysis

September 15th, 2022

Final Report

U.S. Department of Transportation
Federal Aviation Administration

NOTICE

THIRD PARTY RESEARCH. PENDING FAA REVIEW.

The FAA's Center of Excellence for UAS Research
ASSURE
Alliance for System Safety of UAS through Research Excellence

Technical Report Documentation Page

1. Report No.	2. Government Accession No.	3. Recipient's Catalog No.
FAA A11L.UAS.58		

4. Title and Subtitle	5. Report Date
Annex B to Task A17: NIAR/WSU sUAS Numerical Model Validation (Component and Full-Scale Level) for Engine Ingestion Analysis	09/2022
	6. Performing Organization Code ASSURE: NIAR

7. Author(s)	8. Performing Organization Report No.
Hoa Ly (NIAR) Gerardo Olivares (NIAR) Luis Gomez (NIAR) Luis Castillo (NIAR) Gerardo Arboleda (NIAR) Armando De Abreu (NIAR)	

9. Performing Organization Name and Address	10. Work Unit No. (TRAIS)
National Institute for Aviation Research (NIAR) Wichita State University 1845 Fairmount St. Wichita, KS 67260-0123	11. Contract or Grant No.

12. Sponsoring Agency Name and Address	13. Type of Report and Period Covered
U.S. Department of Transportation Federal Aviation Administration Office of Aviation Research Washington, DC 20591	Final Report
	14. Sponsoring Agency Code 5401

15. Supplementary Notes

The Federal Aviation Administration Aviation William J. Hughes Technical Center Research Division COR was

16. Abstract

17. Key Words	18. Distribution Statement
Crashworthiness, Engine Ingestion, UAS, National Institute for Aviation Research, NIAR	This document is available to the U.S. public through the National Technical Information Service (NTIS), Springfield, Virginia 22161. This document is also available from the Federal Aviation Administration William J. Hughes Technical Center at actlibrary.tc.faa.gov.

19. Security Classif. (of this report)	20. Security Classif. (of this page)	21. No. of Pages	22. Price
Unclassified	Unclassified		

Form DOT F 1700.7 (8-72) Reproduction of completed page authorized

TABLE OF CONTENTS

LIST OF FIGURES

LIST OF TABLES

1. SCOPE

1.1 RESEARCH TASKS

To aid A17 program research efforts, the National Institute for Aviation Research (NIAR) at Wichita State University (WSU) performed numerical analysis to validate components and the full quadcopter sUAS models. The details of NIAR's task and collaboration with other universities are described as follows:

Task B (WSU, UAH, OSU): Validate the Finite Element Models (FEM) of individual sUAS components and the full sUAS for engine ingestion scenario through impact tests against titanium blade

The University of Alabama in Huntsville (UAH) conducted collision testing of individual sUAS components (camera, motors, and battery) and a full quadcopter sUAS against fan blade representative titanium plates. The impact tests were performed in the range of 154.33-360.11 m/s (300-700 knots) on an angled titanium plate to obtain contact conditions similar to those expected during an engine ingestion event. This study used fully charged batteries to provide insight into potential fire hazards during ingestion. Ohio State University (OSU) suggested a mesh size for the fan blades based on the computational modeling experiments they conducted and the advice received from our industry partners. Subsequently, NIAR performed numerical analysis to evaluate and validate the different sUAS components and the complete sUAS quadcopter model against the test results provided by UAH. To leverage all the previous work done, the sUAS quadcopter model developed during the FAA ASSURE A3 Airborne Collision Studies [1] was used to evaluate and validate these test results. Load cell, kinematics video, strain gage, and Digital Image Correlation (DIC) data were used to quantify the correlation between the numerical model results and the actual physical tests. The sUAS numerical model was updated as required to better match the UAH test results. Finally, full-scale simulation of the validated sUAS from this task and the fan model developed in Task A by OSU were also conducted to confirm the proper integration and behavior of the sUAS model when interacting with the moving fan blade.

1.2 RESEARCH QUESTIONS

The completion of Task B described in section 1.1 answered the following research questions with initial assumptions and limitations. During the research process, additional assumptions and limitations were realized, specifically regarding the test setup and test conditions, and were accepted to ensure the timely completion of Task B. These are discussed in Annex C to Task A17: UAH High Speed Impacts of Full sUAS and Components with Angled Plates.

Research Questions:

a. What modifications are needed for the quadcopter component (the motor, camera, or battery) and full quadcopter models for higher speed slicing impacts into titanium blades?
b. What range of rotational velocities would be experienced by the fan modeled in this project?

c. What velocities should be used in the experiments to capture the relative velocities in an ingestion event (considering the rotational velocity of the fan, airspeed of the airplane, and velocity of the quadcopter)?
d. How can the full quadcopter be accelerated to the desired speed, and should the quadcopter components be tested at a higher speed?

Assumptions and Limitations:

a. Materials Procurement and manufacturing of titanium wedges will depend on the initial fan design.
b. The fan model from Task A will be completed for integration with the sUAS model.

1.3 OBJECTIVES

The two main objectives of Task B are the FE model validation of the individual sUAS components (motor, camera, and battery), as well as the validation of the full quadcopter model for the engine ingestion impact conditions defined in this research project. The FE models developed in the previous A3 Airborne Collision Studies [1] were leveraged and updated for the current research study to save time and effort.

The successful FE model validation of sUAS components and full sUAS is by comparison with the UAH experimental impact tests. All the test data was compared and corroborated with the numerical analysis results regarding kinematics, load cells, strain gages, DIC, and blade damage state from still images before and after the tests. The kinematics videos, load cells, and still images were the primary sources of validation due to their data's ease of collection and reliability. On the other hand, due to the nature of the slicing impact tests, strain gages and DIC data were more challenging to be collected and only validated where possible. Thus, considered secondary sources for the validation efforts.

Once the complete sUAS quadcopter FE model was validated under current research conditions, NIAR shared it with OSU for integration with the complete engine model. OSU conducted a sensitivity study of various ingestion scenarios to understand better the interaction between sUAS and the fans during engine ingestion. Details regarding this study are discussed in Annex A to Task A17: OSU Representative Fan Model and sUAS Ingestion Studies.

2. QUADCOPTER sUAS VALIDATION

Using the physics-based Building Block Approach, the work done in A3 Airborne Collision Studies [1] validated the full quadcopter sUAS for the blunt impacts with speed up to 128.61 m/s (250 knots). Leveraging A3 validation work, the current research updated the quadcopter FE model starting from the component level and finishing at the full-scale level tests for impact conditions more representative of those observed during engine ingestion scenarios.

2.1 COMPONENT LEVEL

Similar to the A3 Airborne Collision Studies [1], three critical sUAS components were subjected to impact tests for the current research component level validation. These components were: the motor, the camera, and the battery. After discussing the worst sUAS engine impact scenarios with industry partners and NIAR, OSU developed the component level test matrix shown in Table 1. Each sUAS component had two different test configurations at 80% and 50% radial span impact location of the titanium test article. Each test configuration had three repetitions to help quantify variability between tests due to differences in projectile, target, and desired impact conditions for each test. Unfortunately, the machining process damaged one of the blades for the 50% span motor tests, which reduced the total number of tests from 18 to 17.

Table 1. Component level test matrix

Test Case	Test Number	Projectile	Target	Span (%)	Relative Angle (°)	Impact Location	Designed Speed	Performed Speed
M80L7-001	20-188	Motor	It Blade OPT A-2 Rev 2	80	25	LE	710.98 kts (365.76 m/s)	716 kts (368.34 m/s)
M80L7-002	20-189	Motor	Ti Blade OPT A-2 Rev 2	80	25	LE	710.98 kts (365.76 m/s)	713 kts (366.8 m/s)
M80L7-003	20-190	Motor	Ti Blade OPT A-2 Rev 2	80	25	LE	710.98 kts (365.76 m/s)	715 kts (367.83 m/s)
M50L5-004	20-183	Motor	Ti Blade OPT B-5 Rev 2	50	30	LE	562.86 kts (289.56 m/s)	569 kts (292.72 m/s)
M50L5-005	20-184	Motor	Ti Blade OPT B-5 Rev 2	50	30	LE	562.86 kts (289.56 m/s)	569 kts (292.72 m/s)
B80A5-007	20-200	Battery	Ti Blade OPT A-2 Rev 2	80	25	5’’ aft LE	562.86 kts (289.56 m/s)	547 kts (281.4 m/s)
B80A5-008	20-201	Battery	Ti Blade OPT A-2 Rev 2	80	25	5’’ aft LE	562.86 kts (289.56 m/s)	550 kts (282.94 m/s)

B80A5-009	20-202	Battery	Ti Blade OPT A-2 Rev 2	80	25	5'' aft LE	562.86 kts (289.56 m/s)	549 kts (282.43 m/s)
B50L7-010	20-210	Battery	Ti Blade OPT B-5 Rev 2	50	30	LE	710.98 kts (365.76 m/s)	533 kts (274.2 m/s)
B50L7-011	20-211	Battery	Ti Blade OPT B-5 Rev 2	50	30	LE	710.98 kts (365.76 m/s)	539 kts (277.29 m/s)
B50L7-012	20-214	Battery	Ti Blade OPT B-5 Rev 2	50	30	LE	710.98 kts (365.76 m/s)	532 kts (273.68 m/s)
C80L7-013	20-191	Camera	Ti Blade OPT A-2 Rev 2	80	25	LE	710.98 kts (365.76 m/s)	722 kts (371.43 m/s)
C80L7-014	20-192	Camera	Ti Blade OPT A-2 Rev 2	80	25	LE	710.98 kts (365.76 m/s)	711 kts (365.77 m/s)
C80L7-015	20-196	Camera	Ti Blade OPT A-2 Rev 2	80	25	LE	710.98 kts (365.76 m/s)	719 kts (369.89 m/s)
C50L5-016	20-185	Camera	Ti Blade OPT B-5 Rev 2	50	30	LE	562.86 kts (289.56 m/s)	571 kts (293.75 m/s)
C50L5-017	20-186	Camera	Ti Blade OPT B-5 Rev 2	50	30	LE	562.86 kts (289.56 m/s)	569 kts (292.72 m/s)
C50L5-018	20-187	Camera	Ti Blade OPT B-5 Rev 2	50	30	LE	562.86 kts (289.56 m/s)	568 kts (292.72 m/s)

The name of each test case in Table 1 was proposed to provide a brief label that accurately describes each combination of sUAS component, span and relative angle of the blade, location of the impact, and the impact speed. Every impact condition is coded using eight characters (AijBk-mnl):

- A – Distinguishes between sUAS components:
  - Motor (M)
  - Battery (B)
  - Camera (C)
- ij – Distinguishes between span and relative angle of Titanium blade:
  - 80% and 25 deg (80)
  - 50% and 30 deg (50)
- B – Distinguishes between impact location:
  - Leading Edge (L)
  - 5 inches aft of leading edge (A)

- k – Distinguishes between impact speed:
  - 710.98 kts (7)
  - 562.86 kts (5)
- mnl – Distinguishes between the number of the test:
  - 001 (Test 1)
  - 002 (Test 2)
  - …
  - 018 (Test 18)

Example of M80L7-001:

- Motor
- 80% and 25 deg
- Leading edge
- 710.98 kts
- Test 1

Table 2 and Table 3 describe the details of the projectiles and targets, respectively. The shown dimensions and mass of the projectiles are the standard values. Depending on the manufacturing process and quality control, the detail of an sUAS component could vary slightly from one quadcopter to another.

Table 2. Component level projectiles details

Projectile	Dimensions [mm]	Mass [g]	Quantity Needed
Battery	123.19 x 57.15 x 35.05	362.87	6
Motor	32.51 x 28.19 x 28.19	51.03	5
Camera	36.58 x 41.91 x 34.04	51.88	6

Table 3. Component level targets details

Target Description	Material	Target size [mm]	Instrumentation	Quantity Needed
Titanium Blade Opt A-2 (for 80% radial impact)	Ti-6Al-4V	254 x 457.2 (including 76.2 mm extension for bolts connection)	Linear Strain Gauge and DIC	9
Titanium Blade Opt B-5 (for 50% radial impact)	Ti-6Al-4V	254 x 457.2 (including 76.2 mm extension for bolts connection)	Linear Strain Gauge and DIC	8

Figure 2.1 shows the titanium blades with 76.2 mm (3 inches) extension for the bolt connections. Based on OSU initial mesh sensitivity study (discussed in Annex A?), the mesh of the blades originally was suggested to have six (6) element through thickness. In the effort to reduce computational time and improve validation results, NIAR conducted an additional mesh sensitivity study comparing the blade damage and load cell correlations for the component level tests. The study concluded that a coarser blade with three (3) elements through thickness is more efficient and provides similar or better results than the original six (6) element through thickness blades. NIAR mesh study is documented in Appendix A. The subsequent sections for the components and full-scale level validation were done using the final three (3) element through thickness blades.

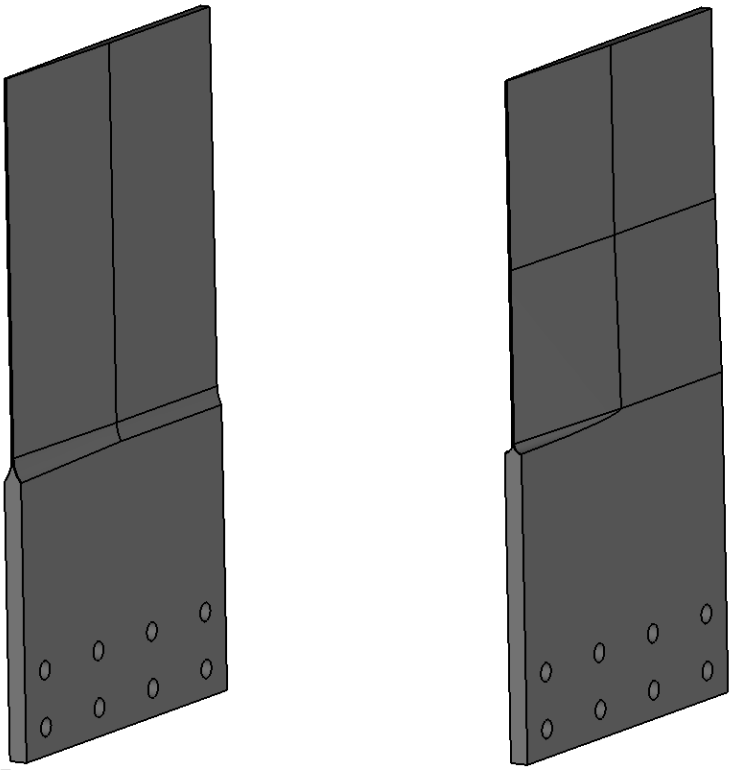

Figure 2.1. Titanium blade opt A-2 (left) and titanium blade opt B-5 (right)

2.1.1 Motor

2.1.1.1 M80L7 Test Configuration

For this test configuration, the motor impacts the leading edge of the titanium blade Opt A-2 at the desired velocity of 365.26 m/s (710 knots). The impact location is at 80% radial span of the blade, and the blade is angled at 25 degrees relative to the impact direction. Three repetitions – M80L7-001, M80L7-002, and M80L7-003 – were conducted. Out of these three repetitions, M80L7-002 was selected to corroborate with the simulation. Figure 2.2 shows the schematic setup of the M80L7 test configuration.

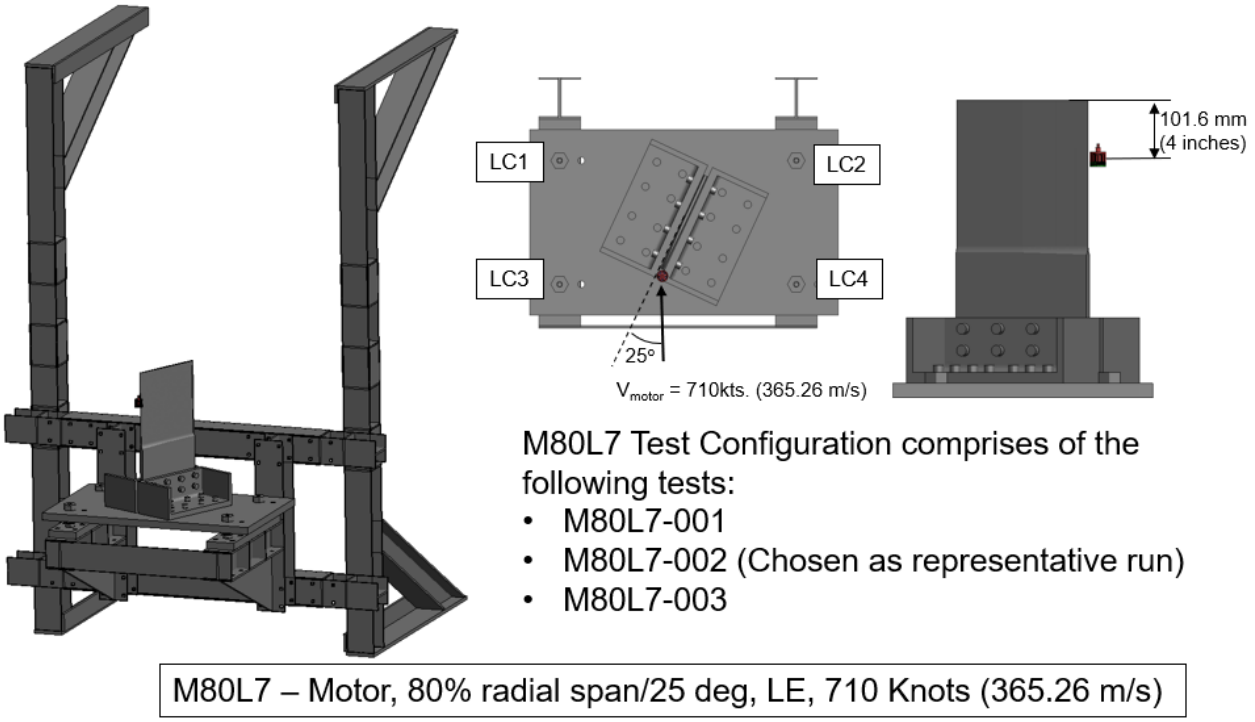

Figure 2.2. M80L7 test configuration setup

To match the conditions of the M80L7-002 test, the FE simulation was set up with the initial projectile velocity of 366.8 m/s (713 knots). The motor's orientation was adjusted to a pitch of -6.1 degrees, a roll of 0 degrees, and yaw of 0 degrees. The impact location to the motor's center of gravity was 106.68 mm (4.2 inches) measured from the top of the blade, which deviated from the desired impact location by 5.08 mm (0.2 inches) shown in Figure 2.2.

Figure 2.3 and Figure 2.4 show the top and side view kinematics comparison between the test and simulation from the start to the end of the impact. Three instances were compared. The first instance at t=0s is the start of the simulation before the impact. The second instance at t=0.00035s is during the impact. The last instance at t=0.0007s is after the impact.

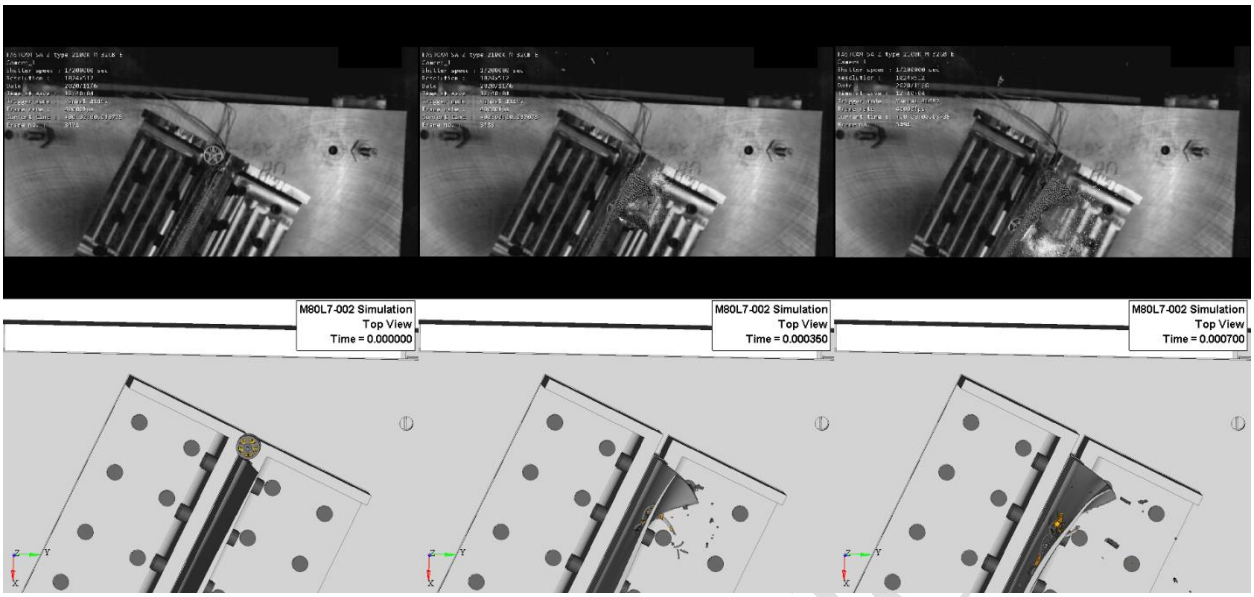

Figure 2.3. M80L7-002 top view kinematics comparison

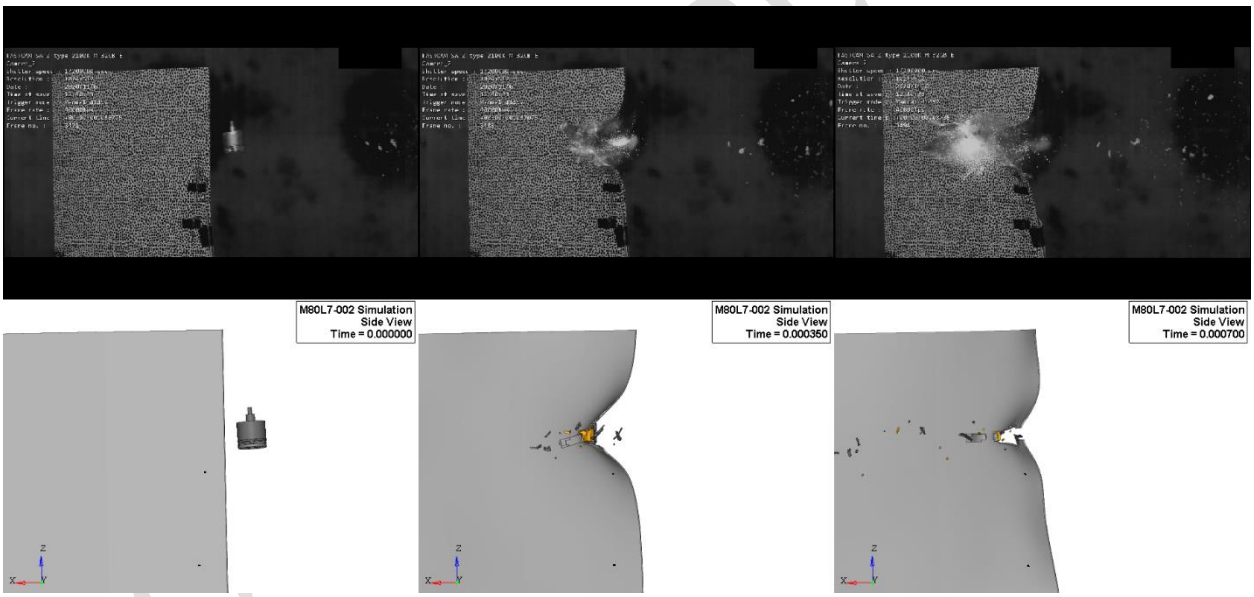

Figure 2.4. M80L7-002 side view kinematics comparison

After 0.7ms of the shown simulation, the blade continued vibrating due to the impact's residual energy. Thus, an additional spring back analysis was performed on the blade to obtain its final deformed shape at its equilibrium state. Figure 2.5 compares the final blade damage after the spring back FE analysis and the physical test damage. The FE result for the blade's LE shows a good correlation with the final deformed shape of the physical blade's LE.

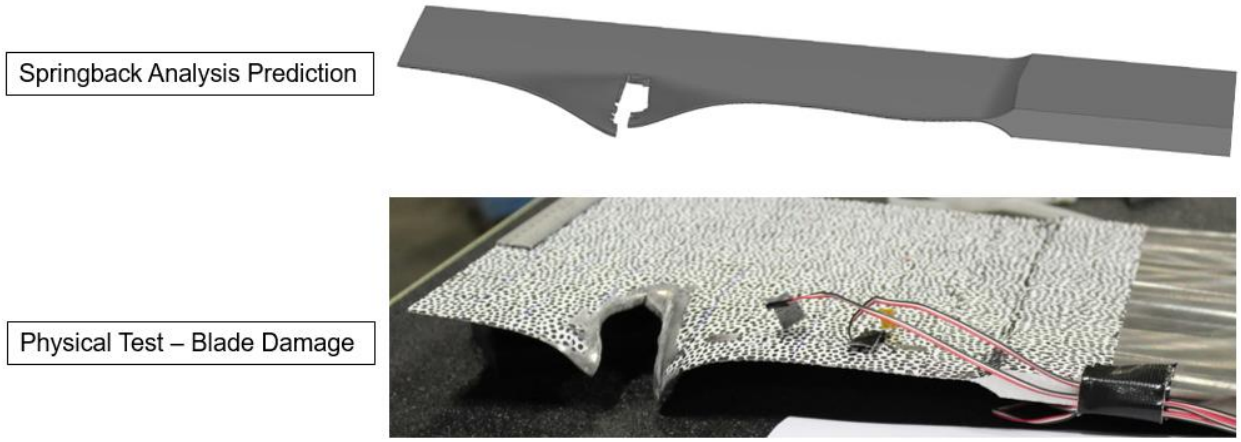

Figure 2.5. Spring back analysis prediction of blade damage vs. physical test damage

Due to the slicing nature of the test, parts of sUAS debris obstructed the blade surfaces during the impact, making it challenging to process the DIC data. Therefore, only partial blade surfaces were selected where DIC data collection was deemed possible. Figure 2.6 shows the selective areas of the blade for the DIC processing in this test M80L7-002.

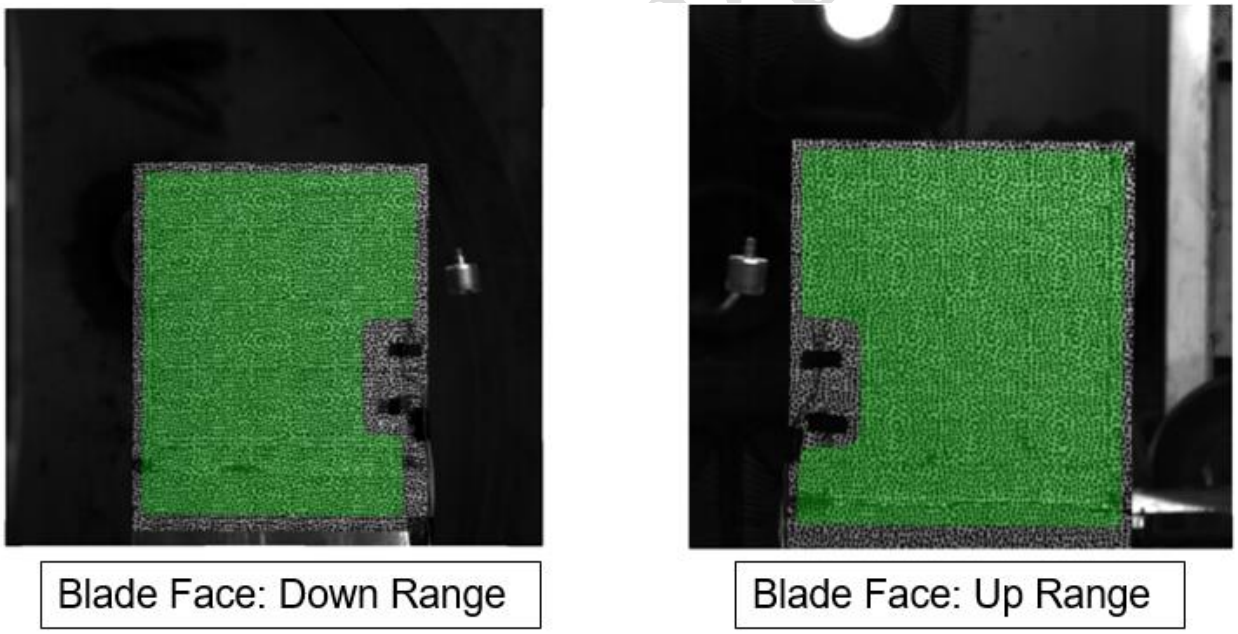

Figure 2.6. Test M80L7-002 selective areas of the blade for DIC processing

Figure 2.7 and Figure 2.8 show the X (blade chord direction) strains, Z (blade span direction) strains, and Y out-of-plane displacement comparison between the DIC test data and simulation during the impact at t=0.00025s. Although the sUAS debris blockage compromised the quality of the DIC data, the contour comparison around the impact region shows a good correlation.

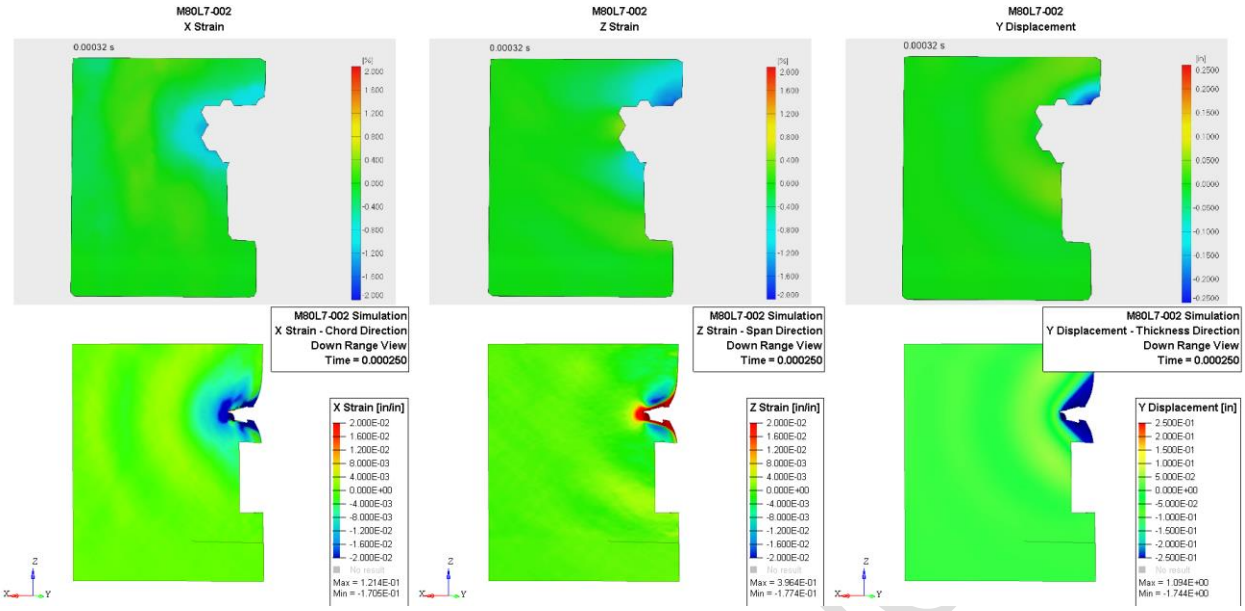

Figure 2.7. Test M80L7-002 DIC comparison on down range face of the blade – Experimental data (top) and simulation (bottom)

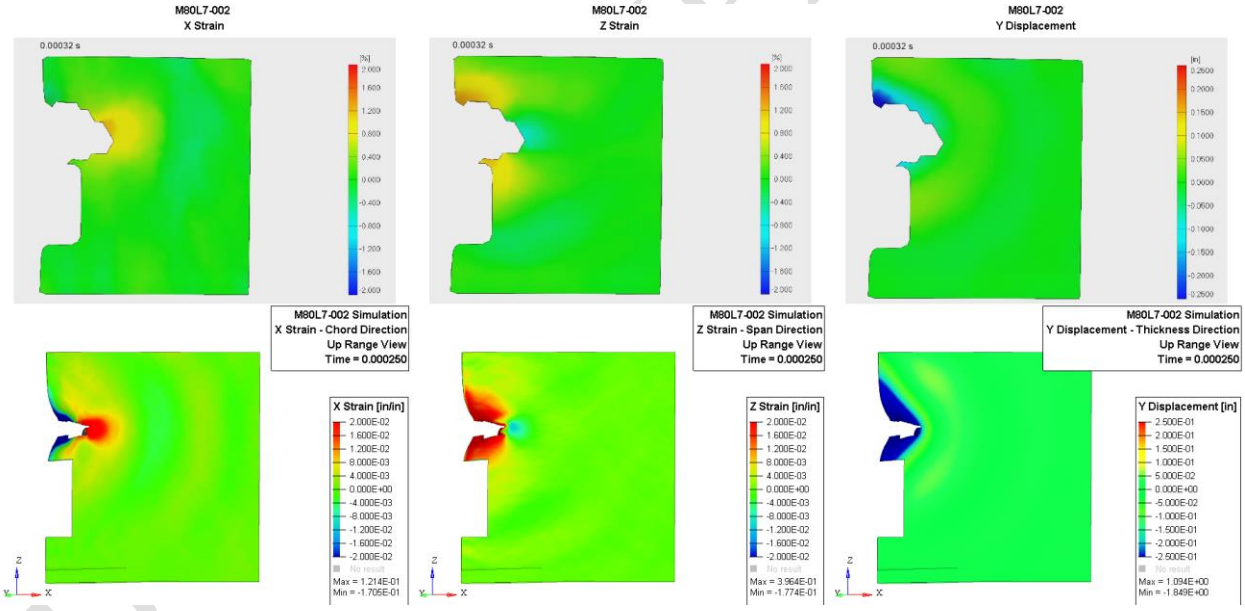

Figure 2.8. Test M80L7-002 DIC comparison on up range face of the blade – Experimental data (top) and simulation (bottom)

In addition to DIC contour data, the time history, showing the resultant displacement for two points (B and G), was obtained and compared with the simulation for all the tests. Figure 2.9. Location of points B and G for extraction of DIC out of plane displacement time historyand Figure 2.10. Resultant displacement time history comparison between simulation and M80L7 testsshow these points' locations and the displacement comparison results. The simulation displacement results correlate well with the M80L7 tests.

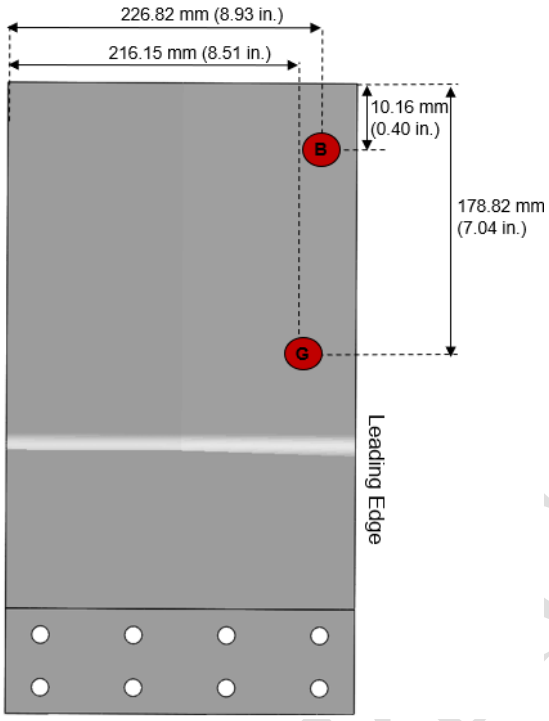

Figure 2.9. Location of points B and G for extraction of DIC out of plane displacement time history

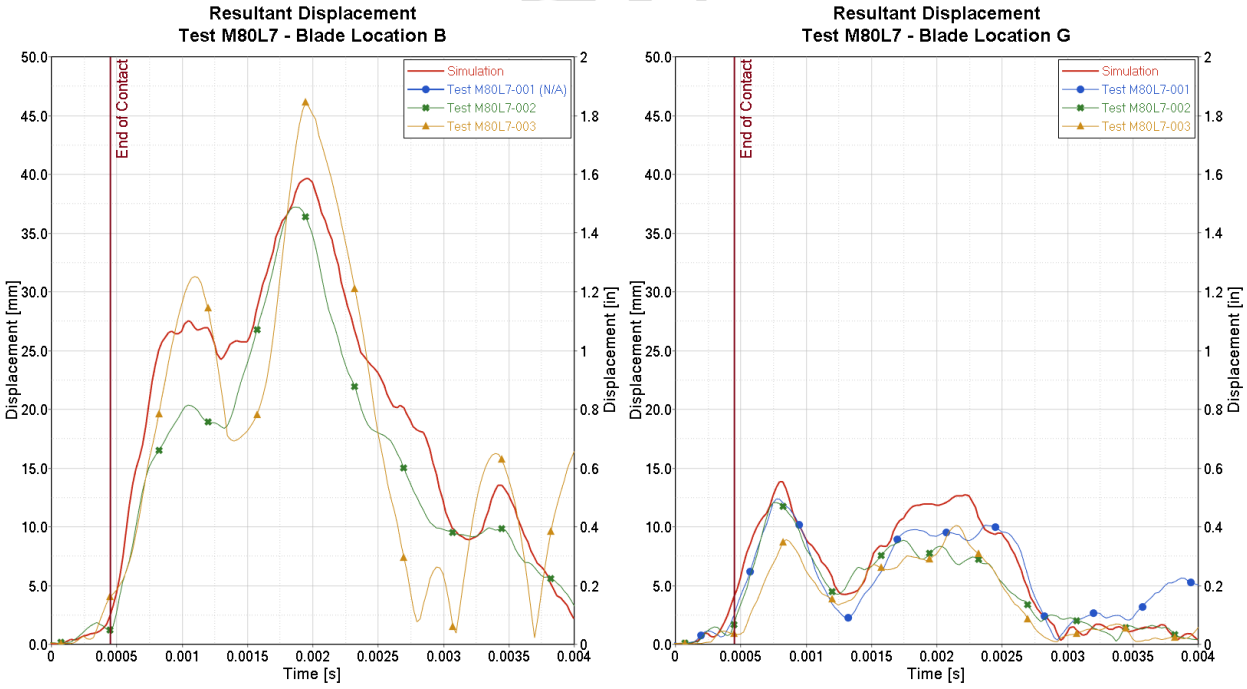

Figure 2.10. Resultant displacement time history comparison between simulation and M80L7 tests

Figure 2.11. Test M80L7 configuration load cells data comparison shows the load cells' data comparison between the simulation and the three test repetitions. The data has no filter, and its sampling rate was 1MHz for both the simulation and tests. The simulation results agree with the test data. The strain gages' data comparison was not possible due to corrupted test data.

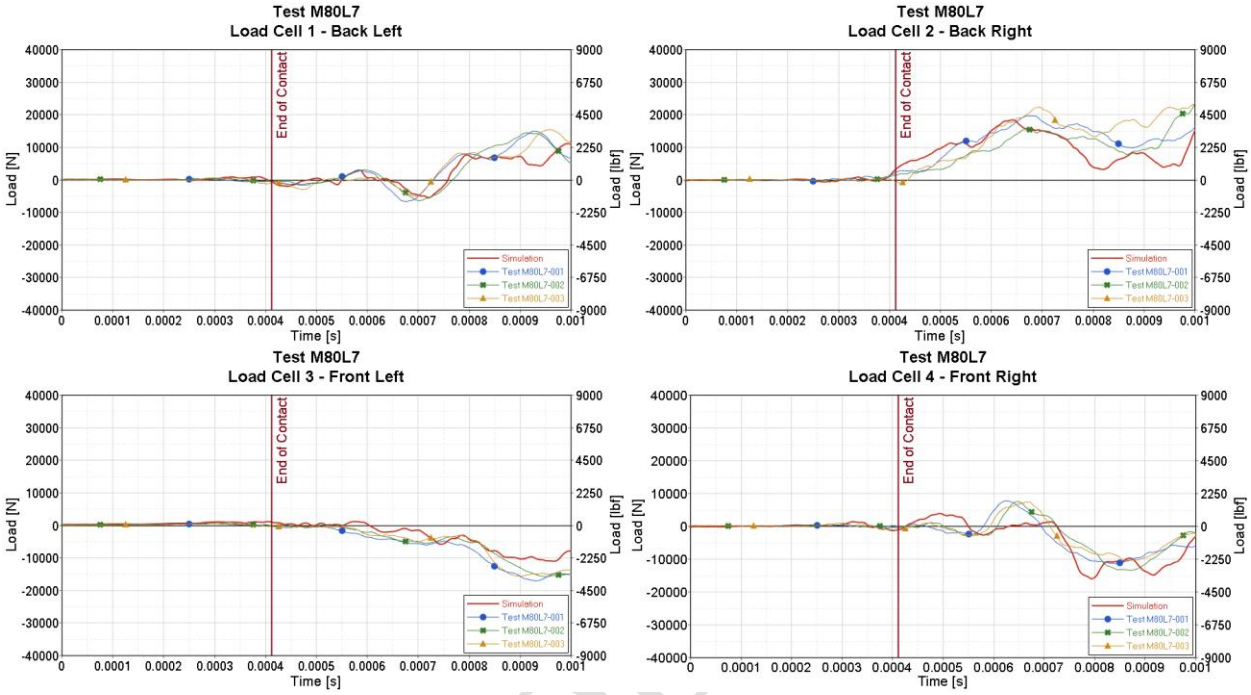

Figure 2.11. Test M80L7 configuration load cells data comparison

The results in this section show a good qualitative correlation between simulation and physical test data in terms of blade damage, loads, and DIC. Thus, for this M80L7 configuration, the motor component of the sUAS is considered validated.

2.1.1.2 M50L5 Test Configuration

For this test configuration, the motor impacts the leading edge of the titanium blade Opt B-5 at the desired velocity of 289.56 m/s (562.86 kts). The impact location is at 50% radial span of the blade, and the blade is angled at 30 degrees relative to the impact direction. Two repetitions – M50L5-004 and M50L5-005 – were conducted. Out of these two repetitions, M50L5-004 was selected to corroborate with the simulation. Figure 2.12 shows the schematic setup of the M50L5 test configuration.

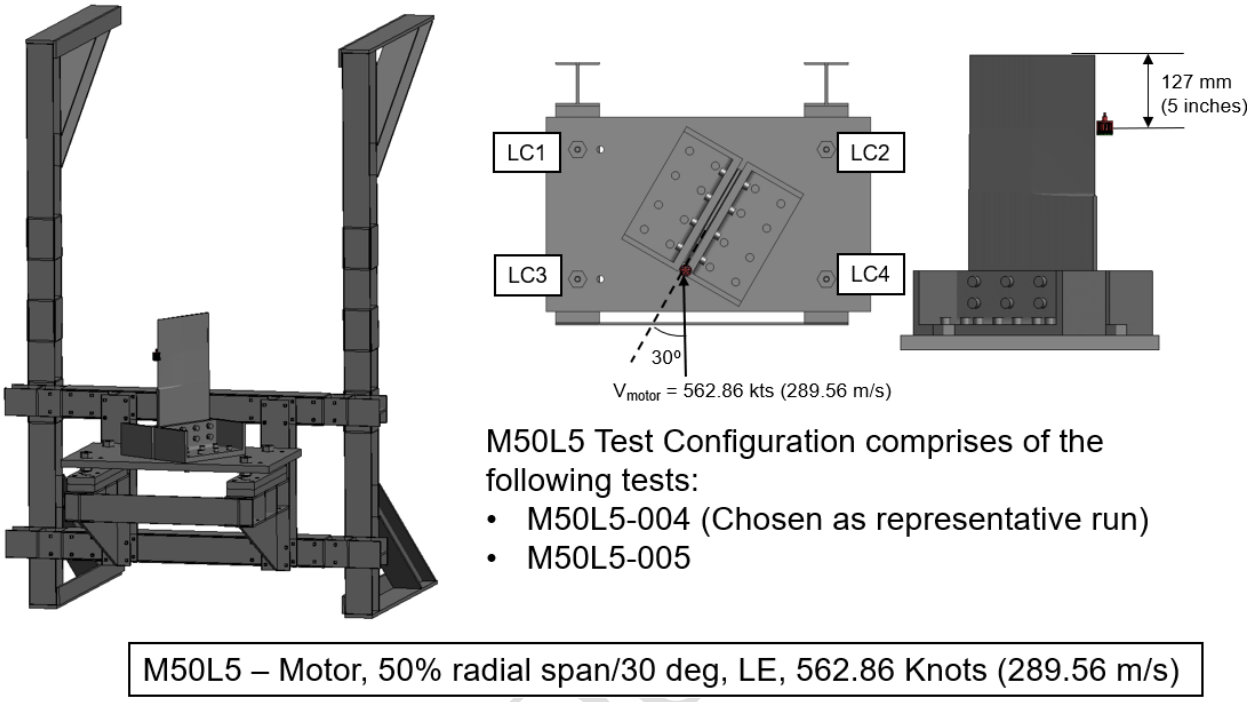

Figure 2.12. M50L5 test configuration setup

To match the conditions of the M50L5-004 test, the FE simulation was set up with the initial projectile velocity of 292.72 m/s (569 kts). The motor's orientation was adjusted to a pitch of -6.5 degrees, a roll of 0 degrees, and yaw of 0 degrees. The impact location to the motor's center of gravity was 128.89 mm (5.07 inches) measured from the top of the blade, which deviated from the desired impact location by 1.78 mm (0.07 inches) shown in Figure 2.12.

Figure 2.13 and Figure 2.14 show the top and side view kinematics comparison between the test and simulation from the start to the end of the impact. Three instances were compared. The first instance at t=0s is the start of the simulation before the impact. The second instance at t=0.00035s is during the impact. The last instance at t=0.0007s is after the impact.

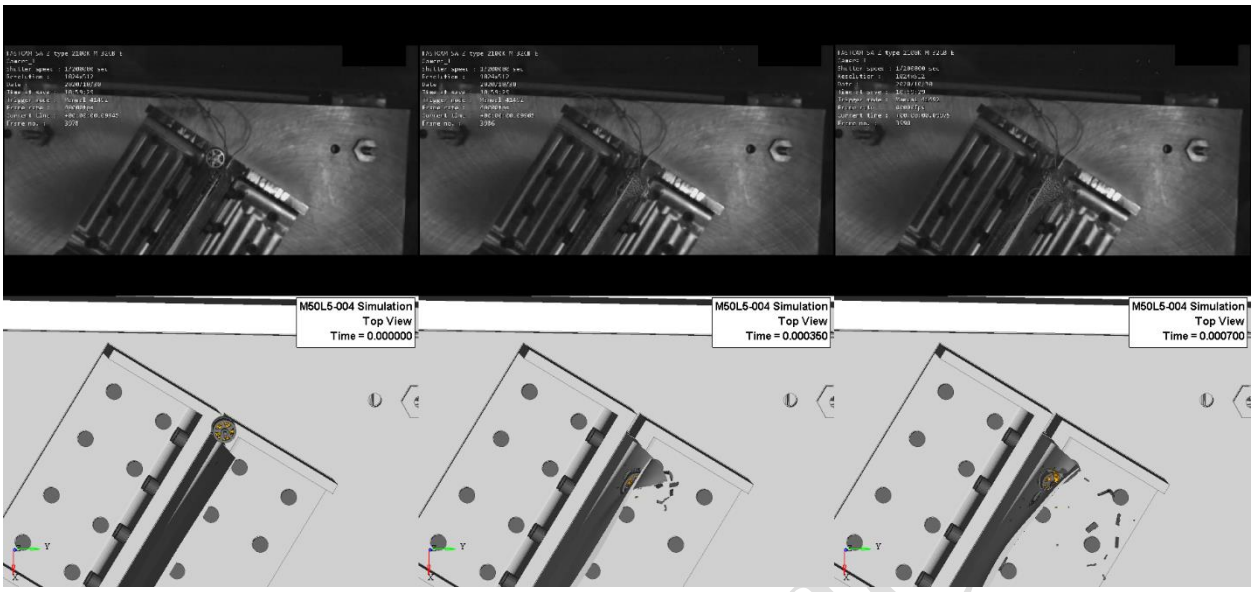

Figure 2.13. M50L5-004 kinematics top view comparison

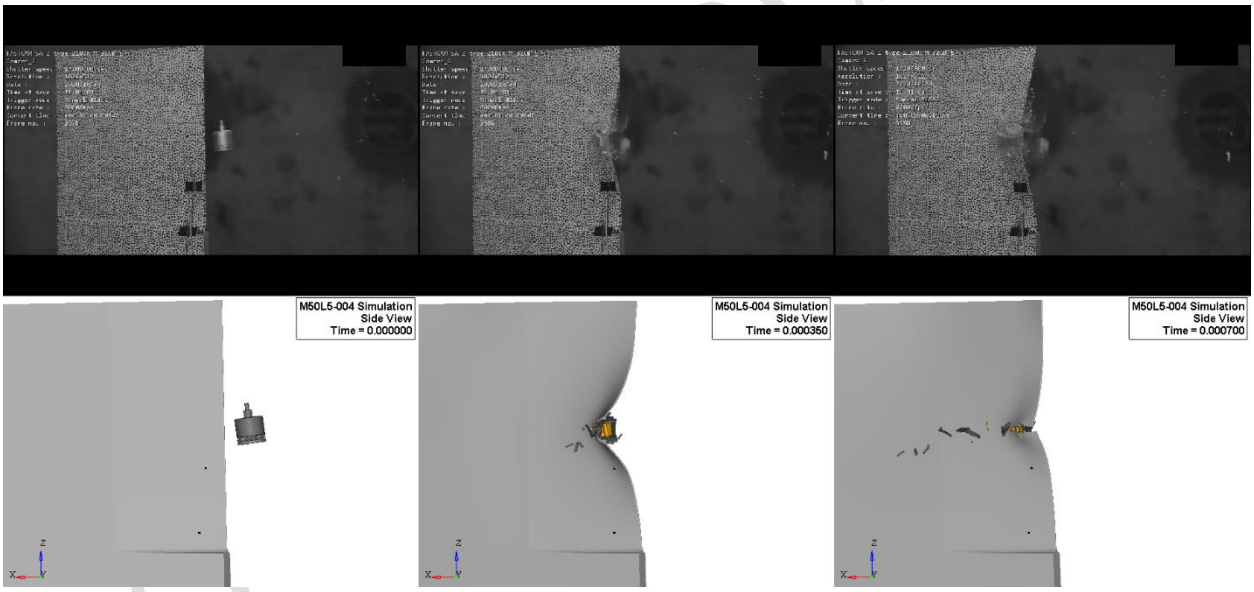

Figure 2.14. M50L5-004 kinematics side view comparison

After 0.7ms of the shown simulation, the blade continued vibrating due to the impact's residual energy. Thus, an additional spring back analysis was performed on the blade to obtain its final deformed shape at its equilibrium state. Figure 2.15 compares the final blade damage after the spring back FE analysis and the physical test damage. Although there is a slight rupture in the simulated blade's LE, the FE result shows a fair correlation with the final deformed shape of the physical blade's LE.

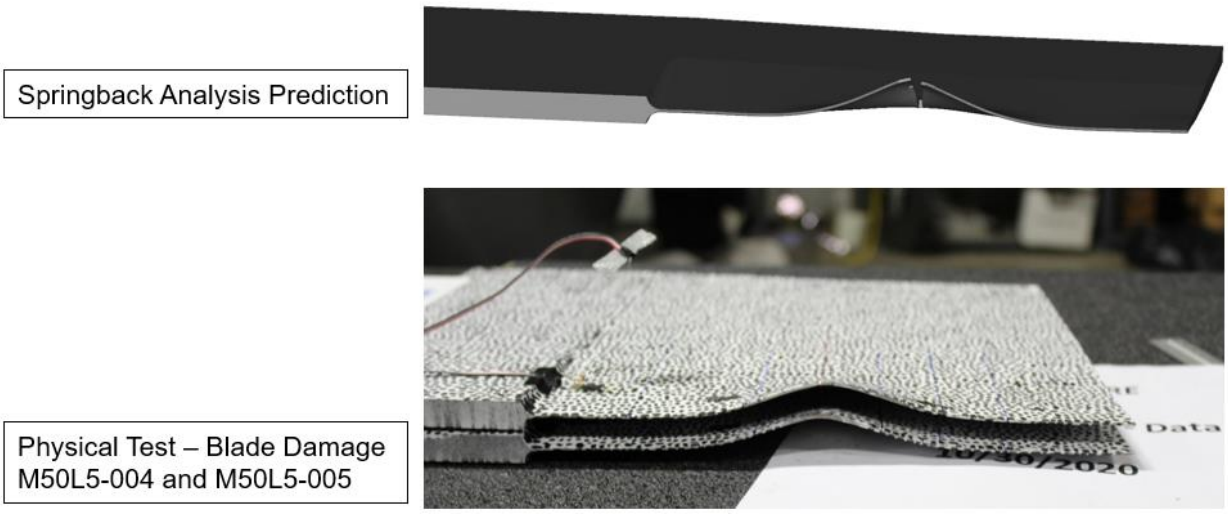

Figure 2.15. Spring back analysis prediction of blade damage vs. physical test damage

Due to the slicing nature of the test, parts of sUAS debris obstructed the blade surfaces during the impact, making it challenging to process the DIC data. Therefore, only partial blade surfaces were selected where DIC data collection was deemed possible. Figure 2.16 shows the selective areas of the blade for the DIC processing in this test M50L5-004.

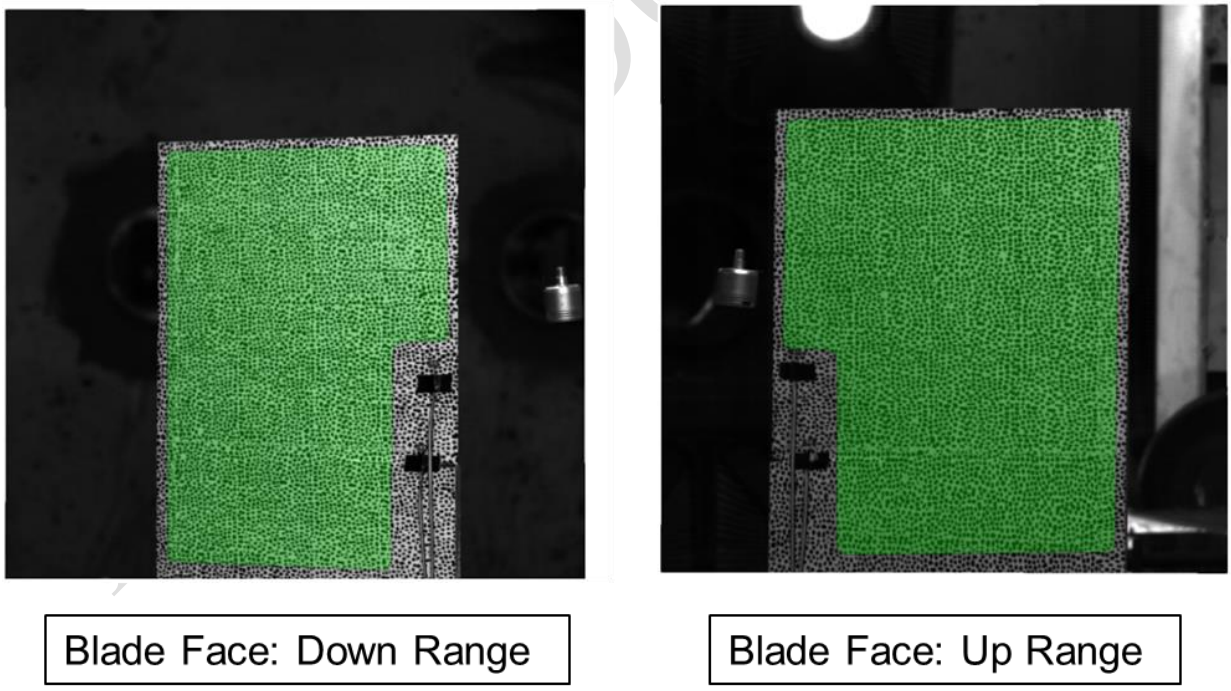

Figure 2.16. Test M50L5-004 selective areas of the blade for DIC processing

Figure 2.17 and Figure 2.18 show the X (blade chord direction) strains, Z (blade span direction) strains, and Y out-of-plane displacement comparison between the DIC test data and simulation during the impact at t=0.0003s. Although the sUAS debris blockage compromised the quality of the DIC data, the contour comparison around the impact region shows a good correlation.

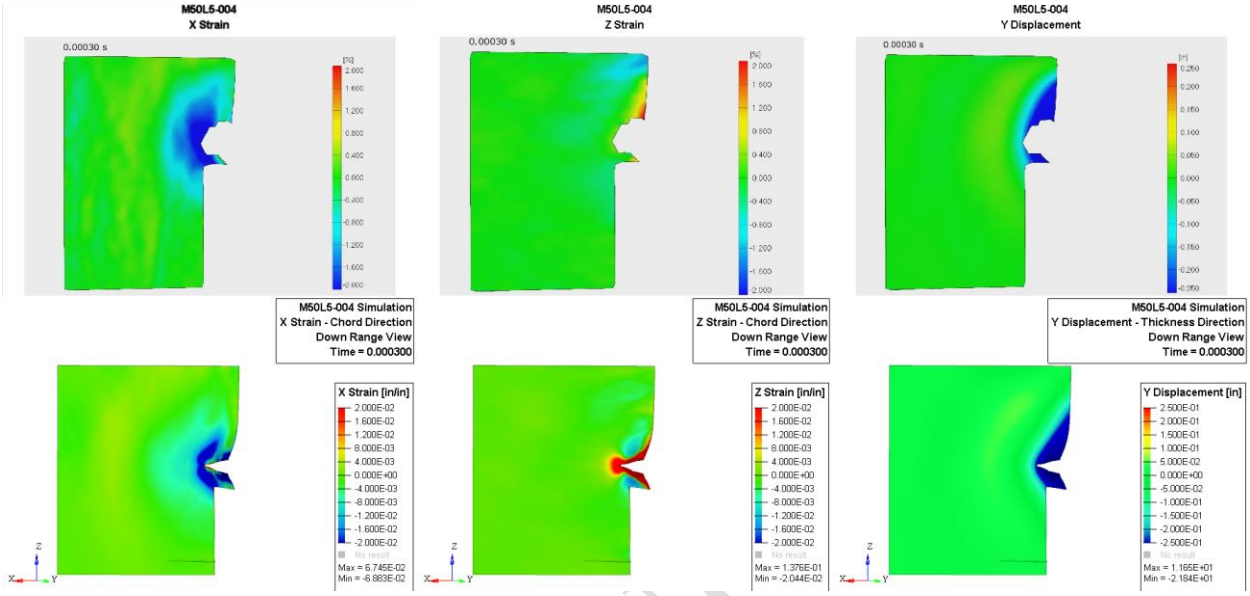

Figure 2.17. Test M50L5-004 DIC comparison on down range face of the blade – Experimental data (top) and simulation (bottom)

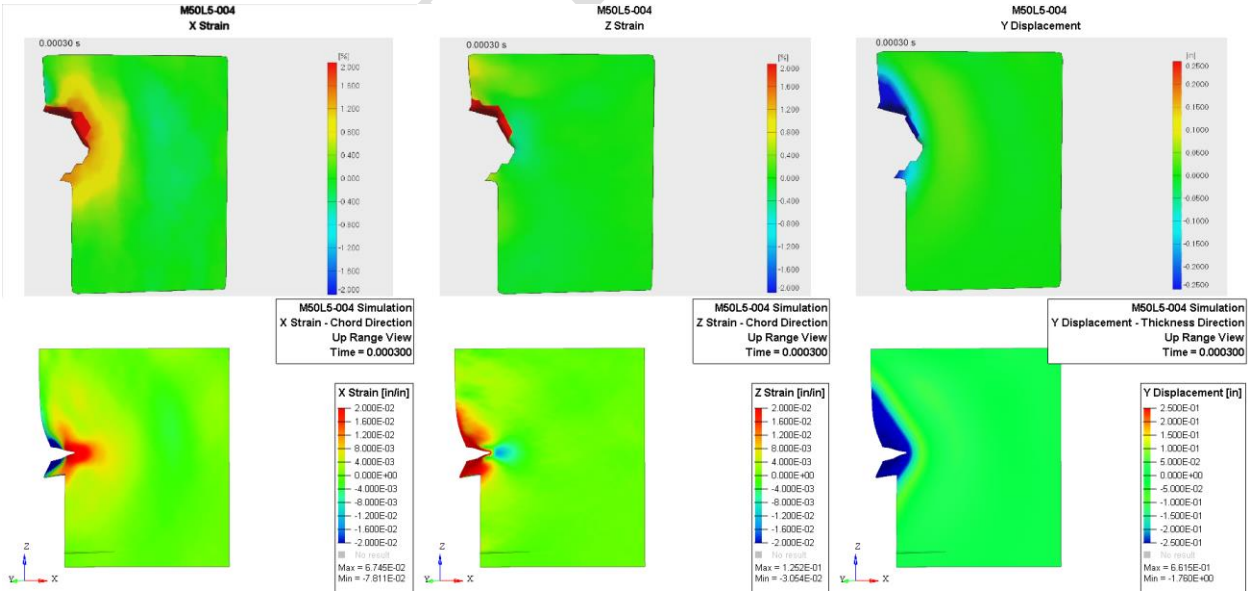

Figure 2.18. Test M50L5-004 DIC comparison on up range face of the blade – Experimental data (top) and simulation (bottom)

In addition to DIC contour data, the time history, showing the resultant displacement for two points (D and G), was obtained and compared with the simulation for all the tests. Figure 2.19 and Figure 2.20 show the location of these points and the results of the displacements comparison. The simulation displacement correlates well with the M50L5 tests.

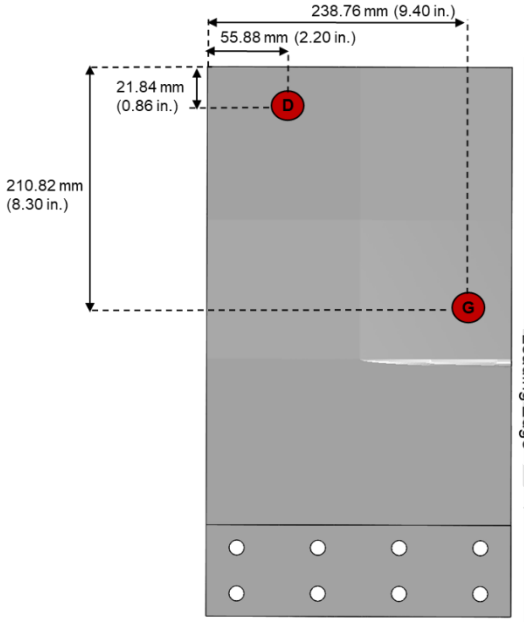

Figure 2.19. Location of points D and G for extraction of DIC resultant displacement time history

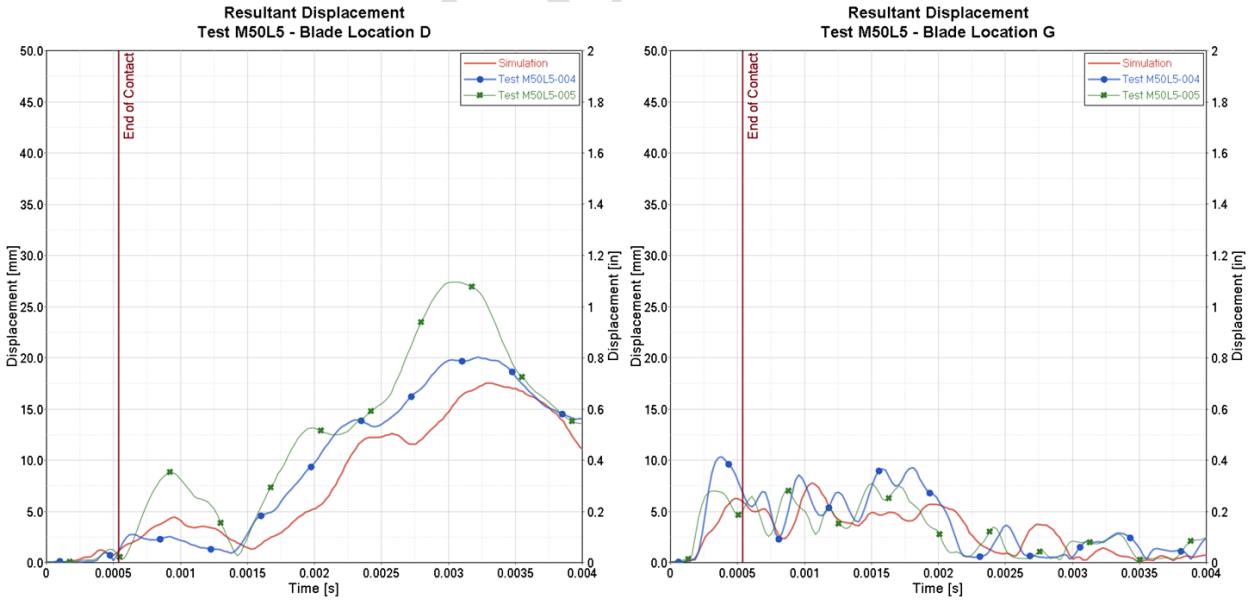

Figure 2.20. Resultant displacement time history comparison between simulation and M50L5 tests

Figure 2.21 shows the load cell data comparison between the simulation and the two test repetitions. The data has no filter, and its sampling rate was 1MHz for both the simulation and tests. The simulation results show good agreement with the test data. The strain gages' data comparison was not possible due to corrupted test data.

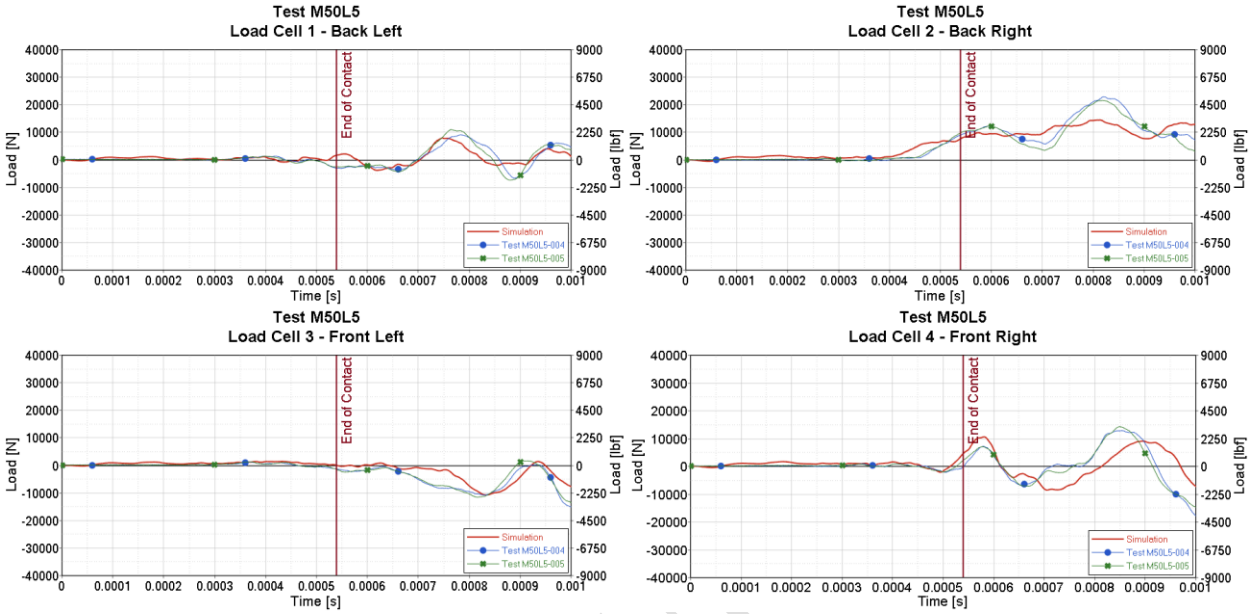

Figure 2.21. Test M50L5 configuration load cells data comparison

The results in this section show a good qualitative correlation between simulation and physical test data in terms of blade damage, loads, and DIC. Thus, for this M50L5 configuration, the motor component of the sUAS is considered validated.

2.1.1.3 FE Information of the Validated UAS Motor

Through the validation efforts described in Section 2.1.1.1 and Section 2.1.1.2 the FE model of the UAS motor is considered validated for the M80L7 and M50L5 test conditions. Figure 2.22 shows the mesh and components of the validated motor, which remain the same as those in A3 program [1]. The main update of the motor in A17 program was on the refinement of material failure definitions for the magnets and stator components. They were re-calibrated for better correlation with the current study test conditions. Once updated, the three most important A3 motor component level tests were rerun to guarantee that these small changes did not significantly affect the previous validation effort.

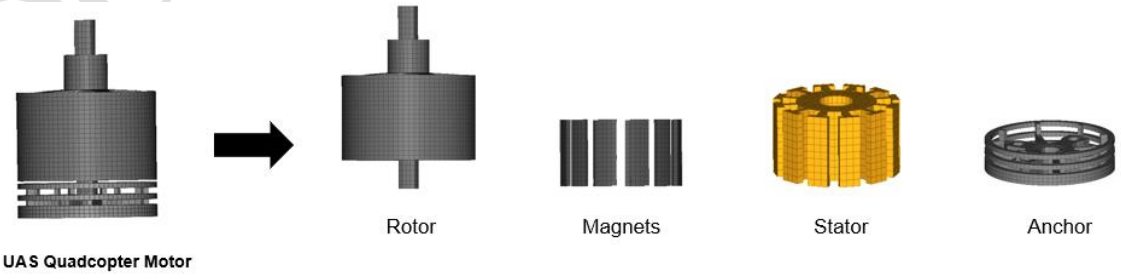

Figure 2.22. Validated FE model of UAS motor

2.1.2 Camera

2.1.2.1 C80L7 Test Configuration

For this test configuration, the camera impacts the leading edge of the titanium blade Opt A-2 at the desired velocity of 365.26 m/s (710 knots). The impact location is at 80% radial span of the blade, and the blade is angled at 25 degrees relative to the impact direction. Three repetitions – C80L7-013, C80L7-014, and C80L7-015– were conducted. Of these three repetitions, C80L7-014 was selected to corroborate with the simulation. Figure 2.23 shows the schematic setup of the C80L7 test configuration.

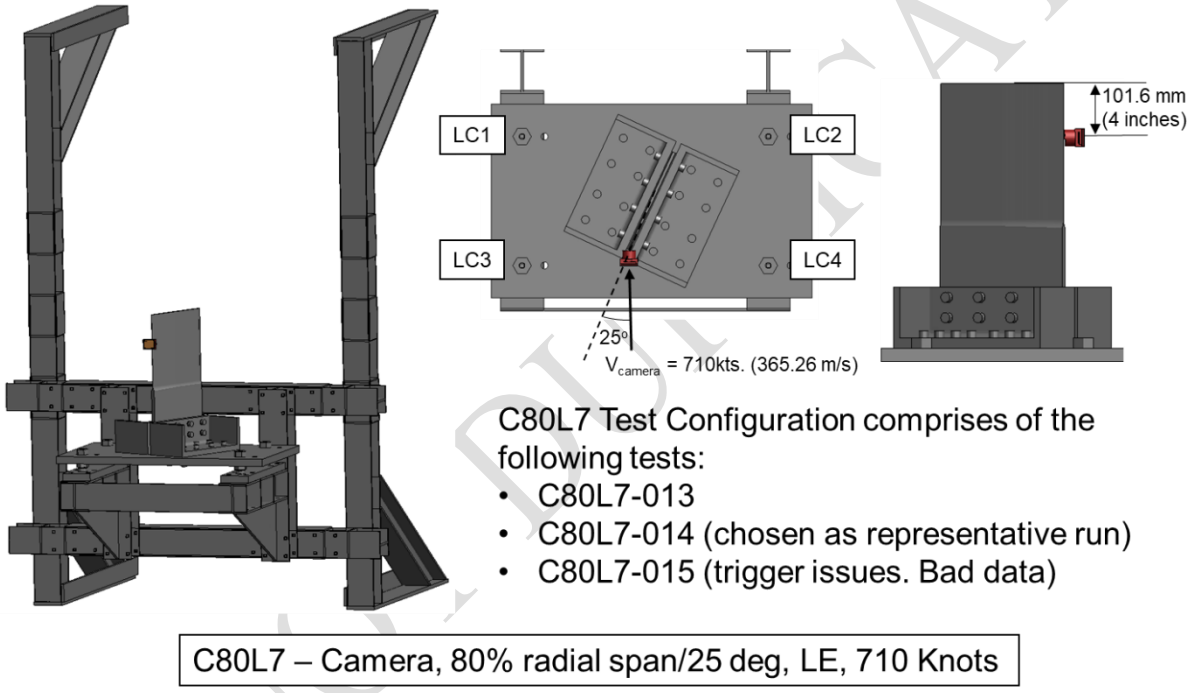

Figure 2.23. C80L7 test configuration setup

To match the conditions of the C80L7-014 test, the FE simulation was set up with the initial projectile velocity of 362.77 m/s (711 knots). The camera's orientation was adjusted to a pitch of 3 degrees, a roll of 0, and yaw of 0.3 degrees. The impact location to the camera's c.g. was 101.31 mm (3.988 inches) measured from the top of the blade, which deviated from the desired impact location by 0.279 mm (0.011 inches) shown in Figure 2.23.

Figure 2.24 and Figure 2.25 show the top and side view kinematics comparison between the test and simulation from the start to the end of the impact. Three instances were compared. The first instance at t=0s is the start of the simulation before the impact. The second instance at t=0.0003s is during the impact. The last instance at t=0.0006s is after the impact.

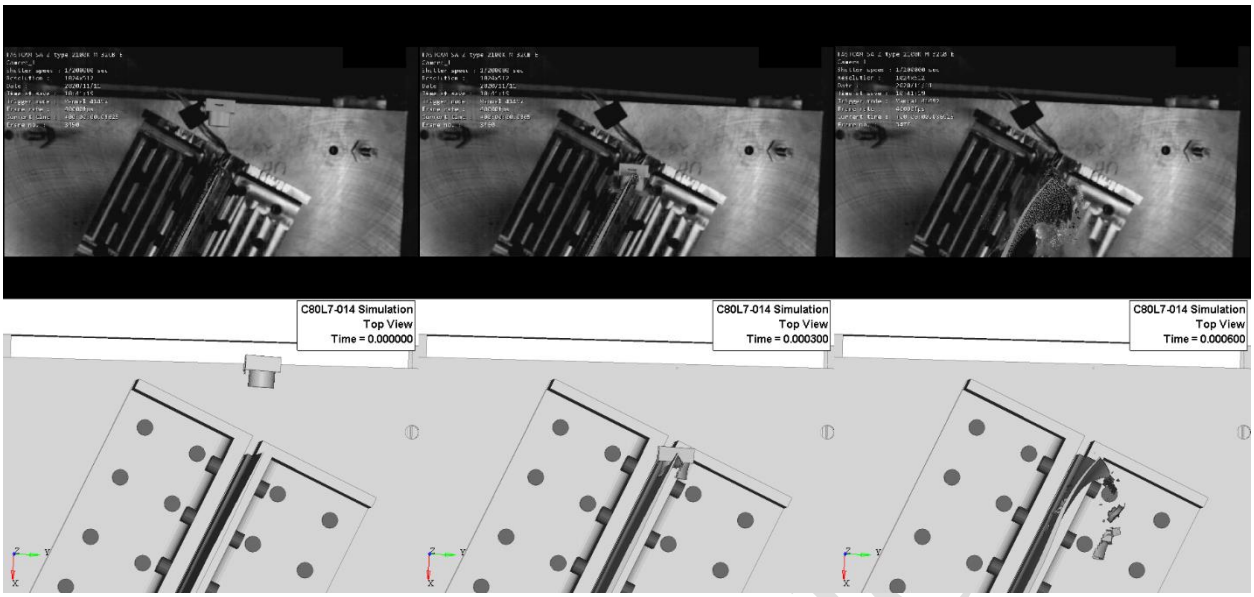

Figure 2.24. C80L7-014 top view kinematics comparison

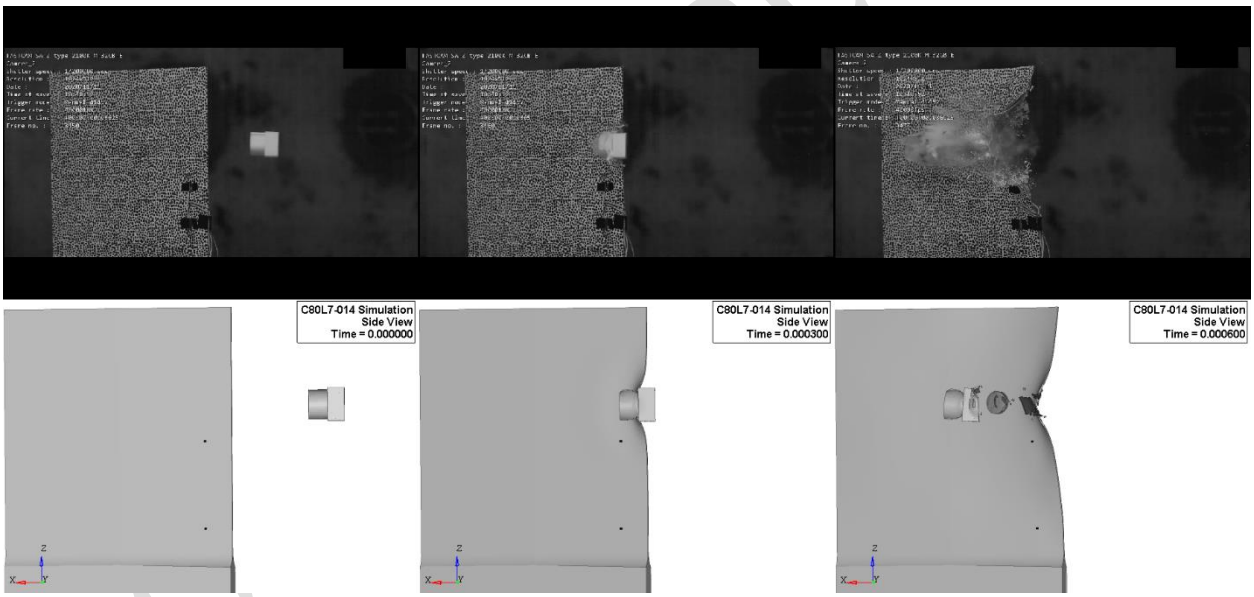

Figure 2.25. C80L7-014 side view kinematics comparison

After 0.6ms of the shown simulation, the blade continued vibrating due to the impact's residual energy. Thus, an additional spring back analysis was performed on the blade to obtain its final deformed shape at its equilibrium state. Figure 2.26 compares the final blade damage after the spring back FE analysis and the physical test damage. The FE result for the blade's LE shows a good correlation with the final deformed shape of the physical blade's LE.

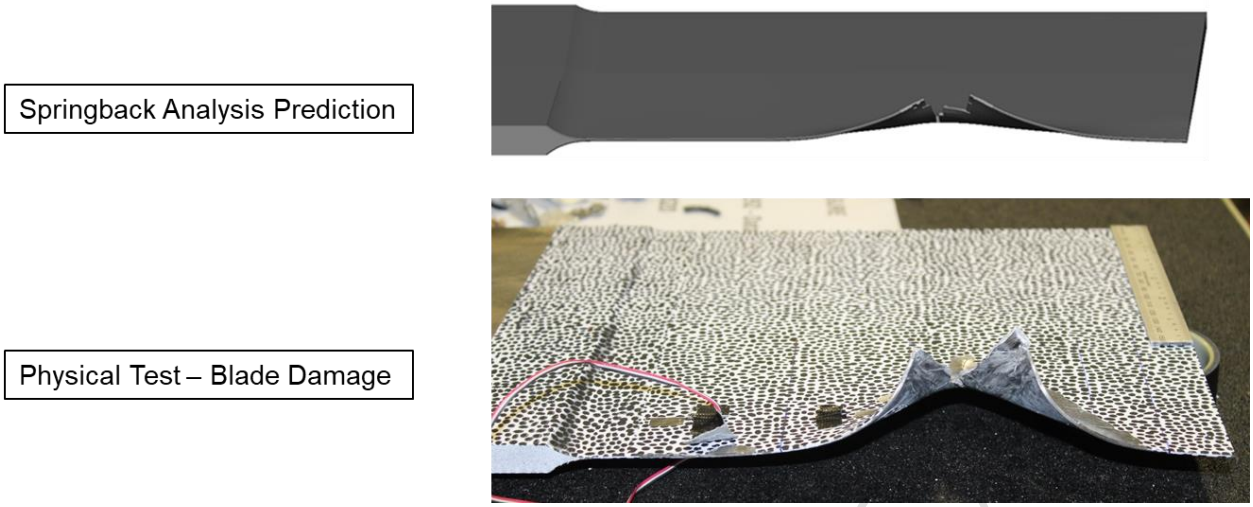

Figure 2.26. Spring back analysis prediction of blade damage vs. physical test damage

Due to the slicing nature of the test, parts of sUAS debris obstructed the blade surfaces during the impact, making it challenging to process the DIC data. Therefore, only partial blade surfaces were selected where DIC data collection was deemed possible.Figure 2.6 Figure 2.27 shows the selective areas of the blade for the DIC processing in this test C80L7-014.

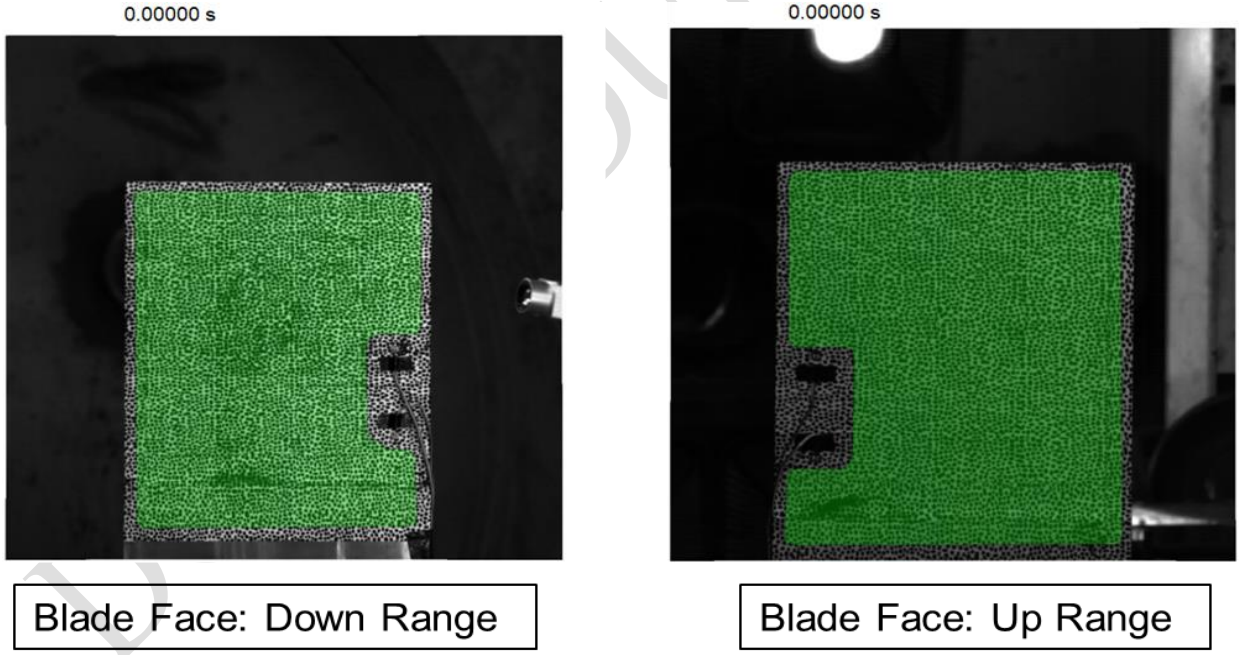

Figure 2.27. Test C80L7-014 selective areas of the blade for DIC processing

Figure 2.28 and Figure 2.29 show the X (blade chord direction) strains, Z (blade span direction) strains, and Y out-of-plane displacement comparison between the DIC test data and simulation during the impact at t=0.000425s. Although the sUAS debris blockage compromised the quality of the DIC data, the contour comparison around the impact region shows a good correlation.

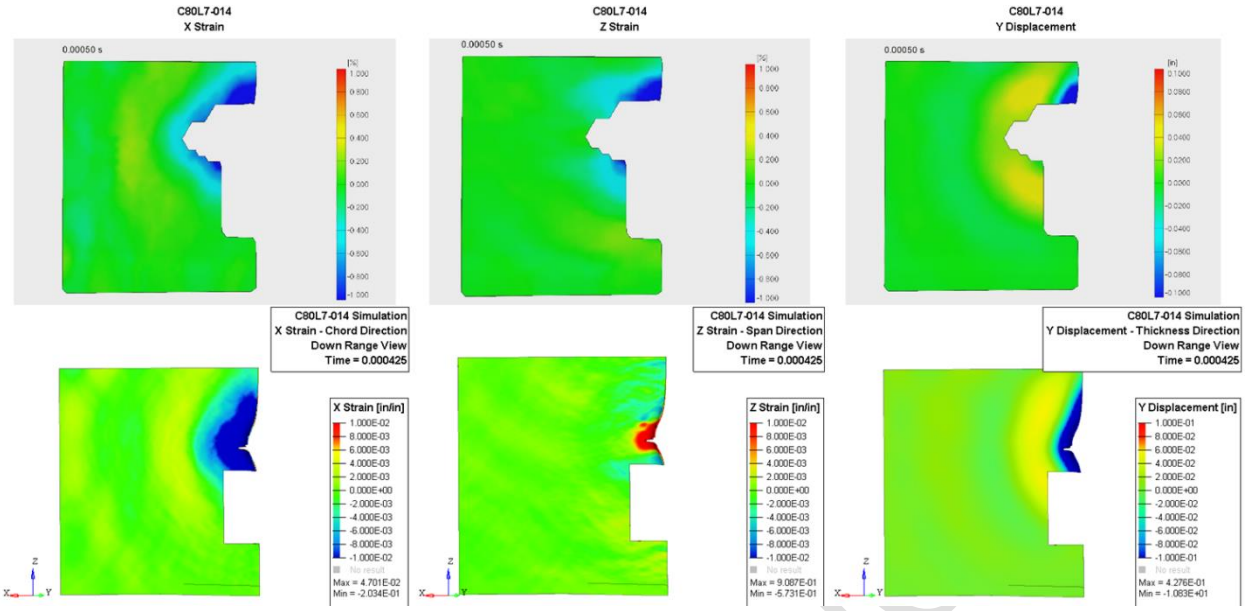

Figure 2.28. Test C80L7-014 DIC comparison on down range face of the blade – Experimental data (top) and simulation (bottom)

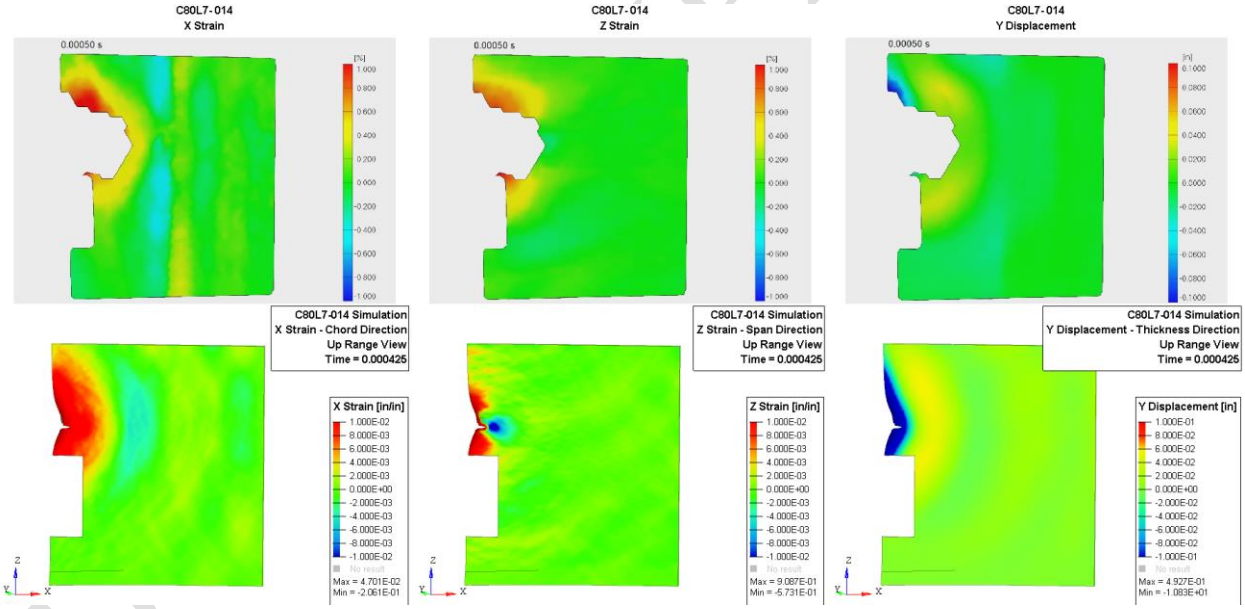

Figure 2.29. Test C80L7-014 DIC comparison on up range face of the blade – Experimental data (top) and simulation (bottom)

In addition to DIC contour data, the time history, showing the resultant displacement for two points (D and G), was obtained and compared with the simulation for all the tests. Figure 2.30 and Figure 2.31 show the location of these points and the results of the displacement comparison. The simulation displacement results correlate well with the C80L7 tests.

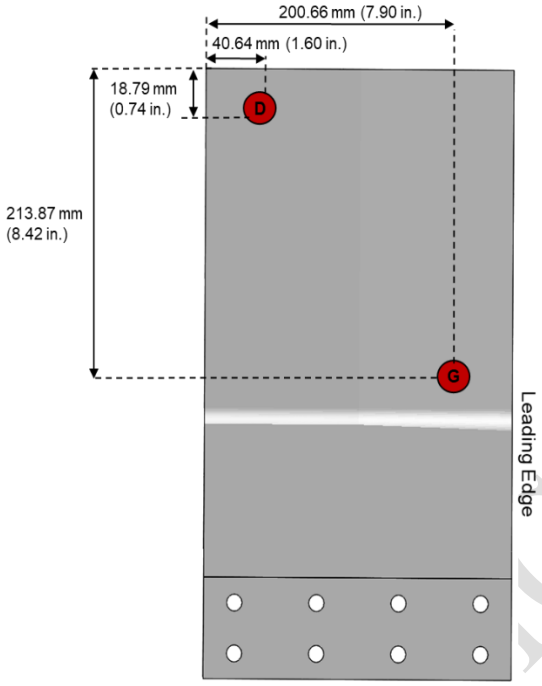

Figure 2.30. Location of points D and G for extraction of DIC resultant displacement time history

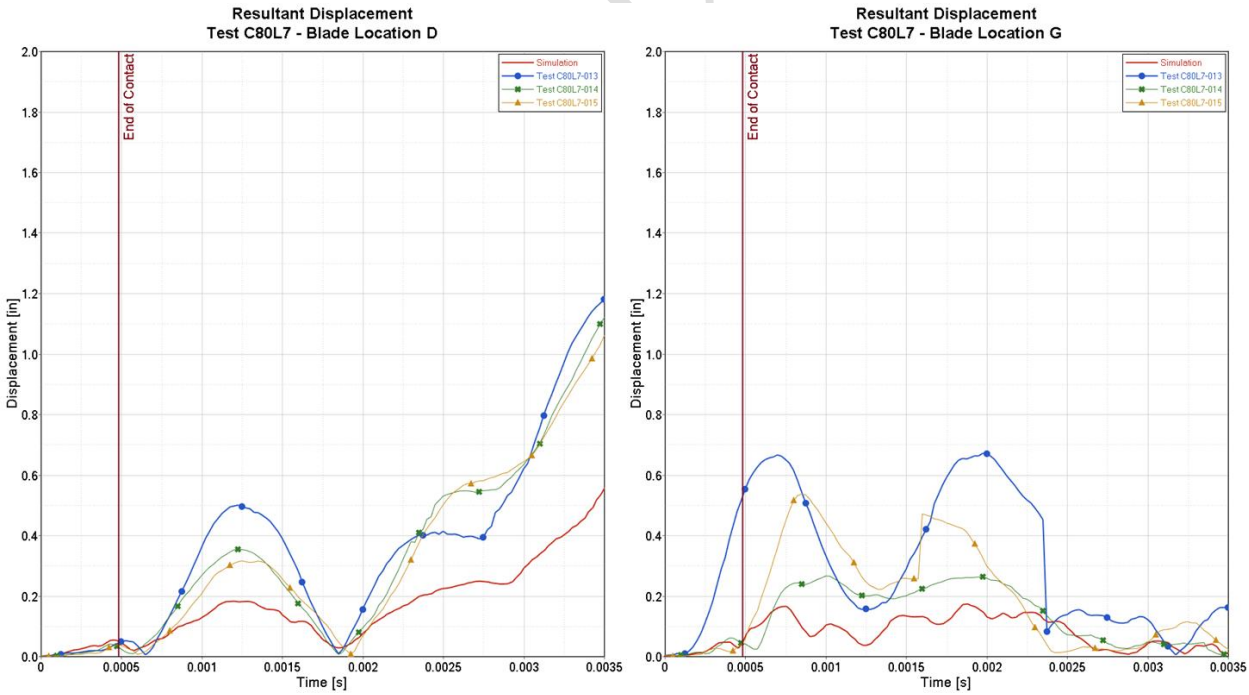

Figure 2.31. Resultant displacement time history comparison between simulation and C80L7 tests

Figure 2.32 shows the load cells' data comparison between the simulation and the three test repetitions. The data has no filter, and the sampling rate of the data was 1MHz for both the simulation and tests. The simulation results agree with the test data. The strain gages' data comparison was not possible due to corrupted test data.

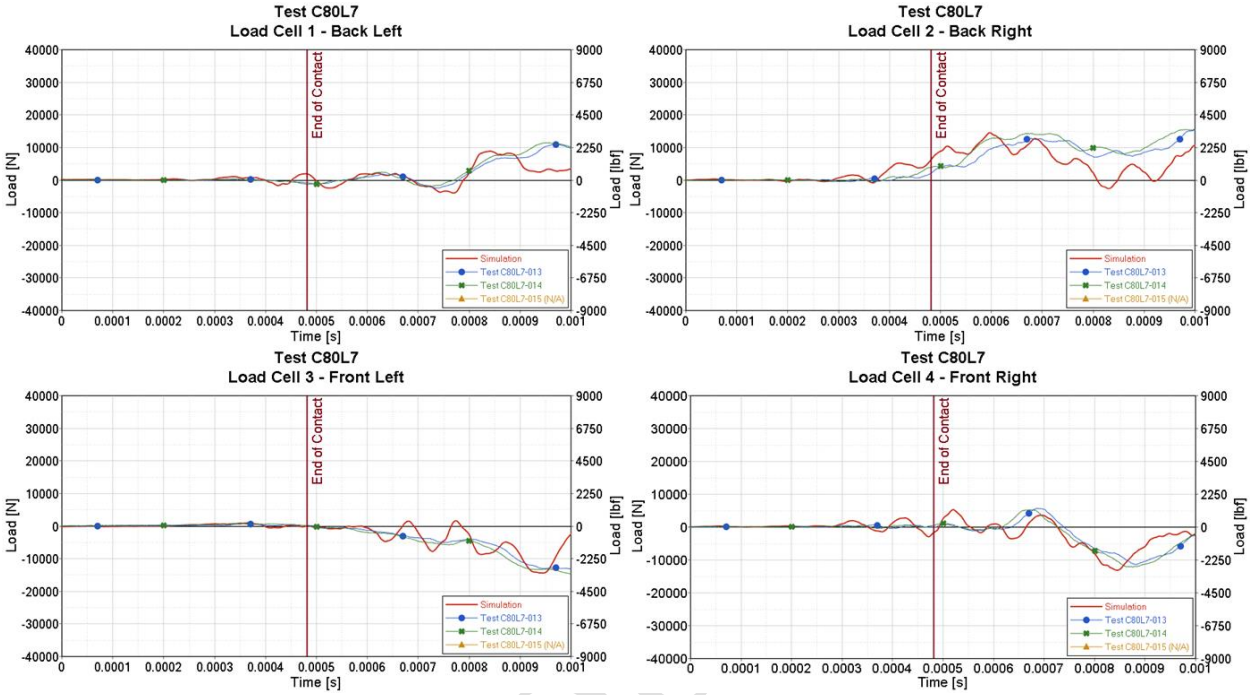

Figure 2.32. Test C80L7 configuration load cells data comparison

The results in this section show a good qualitative correlation between simulation and physical test data in terms of blade damage, loads, and DIC. Thus, for this C80L7 configuration, the camera component of the sUAS is considered validated.

2.1.2.2 C50L5 Test Configuration

For this test configuration, the camera impacts the leading edge of the titanium blade Opt B-5 at the desired velocity of 289.56 m/s (562.86 kts). The impact location is at 50% radial span of the blade, and the blade is angled at 30 degrees relative to the impact direction. Three repetitions – C50L5-016, C50L5-017, and C50L5-018– were conducted. Of these three repetitions, C50L5-016 was selected to corroborate with the simulation. Figure 2.33 shows the schematic setup of the C50L5 test configuration.

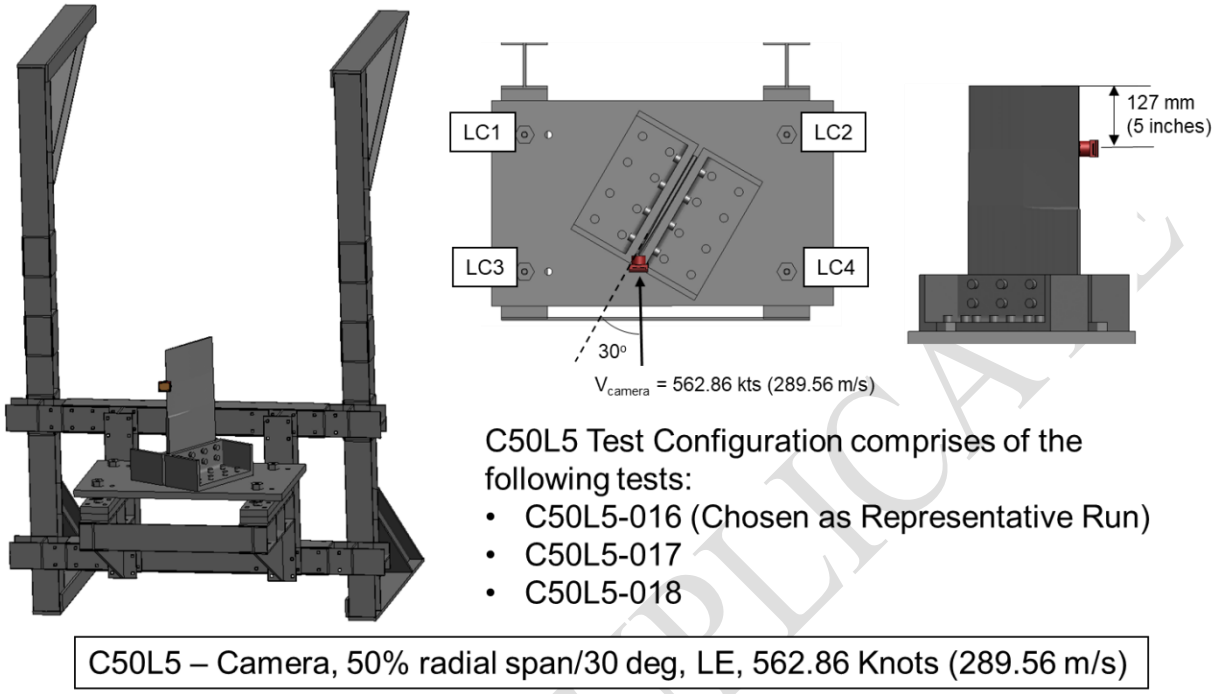

Figure 2.33. C50L5 test configuration setup

To match the conditions of the C50L5-016 test, the FE simulation was set up with the initial projectile velocity of 293.75 m/s (571 knots). The camera's orientation was adjusted to a pitch of -2 degrees, a roll of -6 degrees, and yaw of -0.55 degrees. The impact location to the camera's c.g. was 126.697 mm (4.988 inches) measured from the top of the blade, which deviated from the desired impact location by 0.305mm (0.012inches) shown in Figure 2.33.

Figure 2.34 and Figure 2.35 show the top and side view kinematics comparison between the test and simulation from the start to the end of the impact. Three instances were compared. The first instance at t=0s is the start of the simulation before the impact. The second instance at t=0.00035s is during the impact. The last instance at t=0.0007s is after the impact.

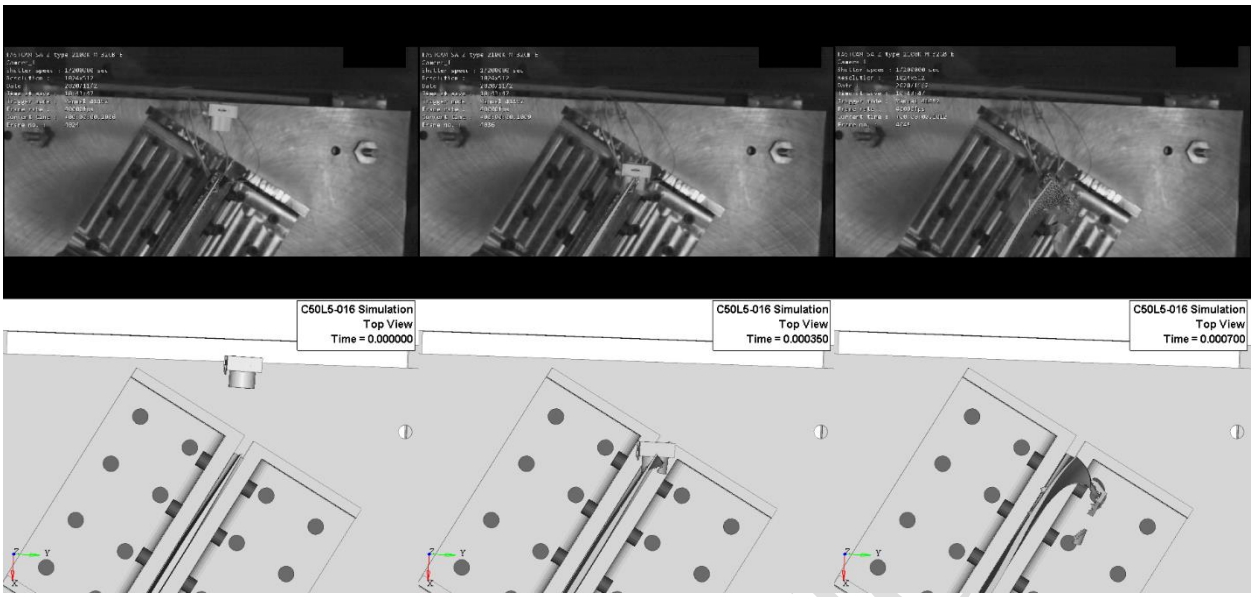

Figure 2.34. C50L5-016 top view kinematics comparison

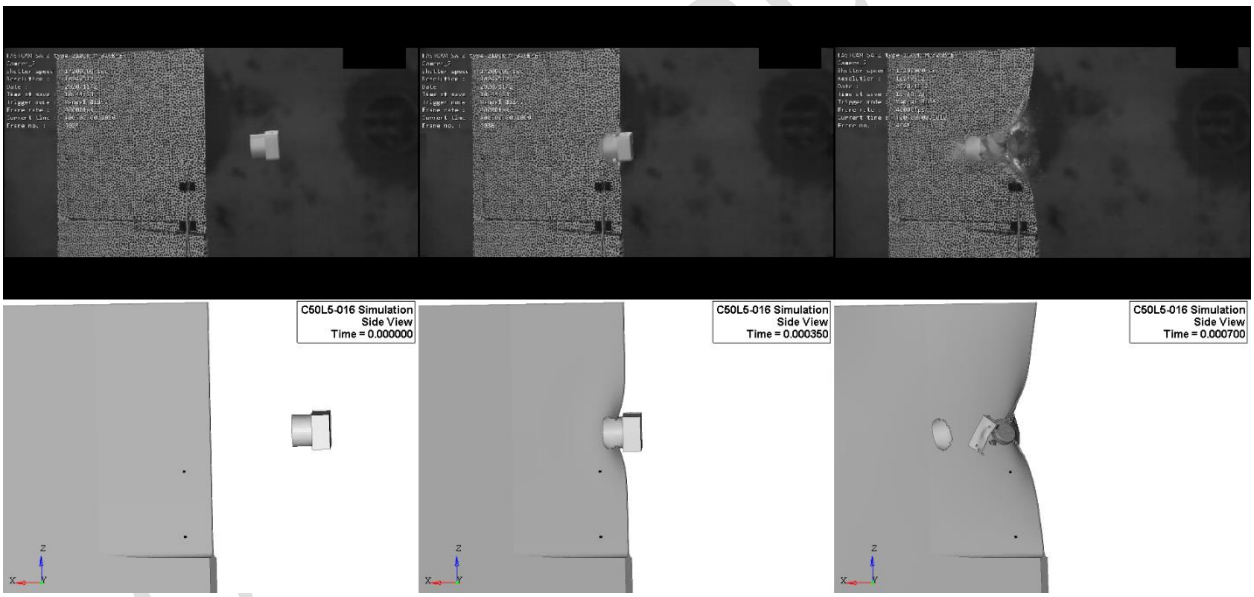

Figure 2.35. C50L5-016 side view kinematics comparison

After 0.7ms of the shown simulation, the blade continued vibrating due to the impact's residual energy. Thus, an additional spring back analysis was performed on the blade to obtain its final deformed shape at its equilibrium state. Figure 2.36 compares the final blade damage after the spring back FE analysis and the physical test damage. The FE result for the blade's LE shows a good correlation with the final deformed shape of the physical blade's LE.

Figure 2.36. Spring back analysis prediction of blade damage vs. physical test damage

Due to the slicing nature of the test, parts of sUAS debris obstructed and scraped the blade surfaces during the impact, making it challenging to process the DIC data. Therefore, only partial blade surfaces were selected where DIC data collection was deemed possible. Figure 2.37 shows the selective areas of the blade for the DIC processing in this test C50L5-016.

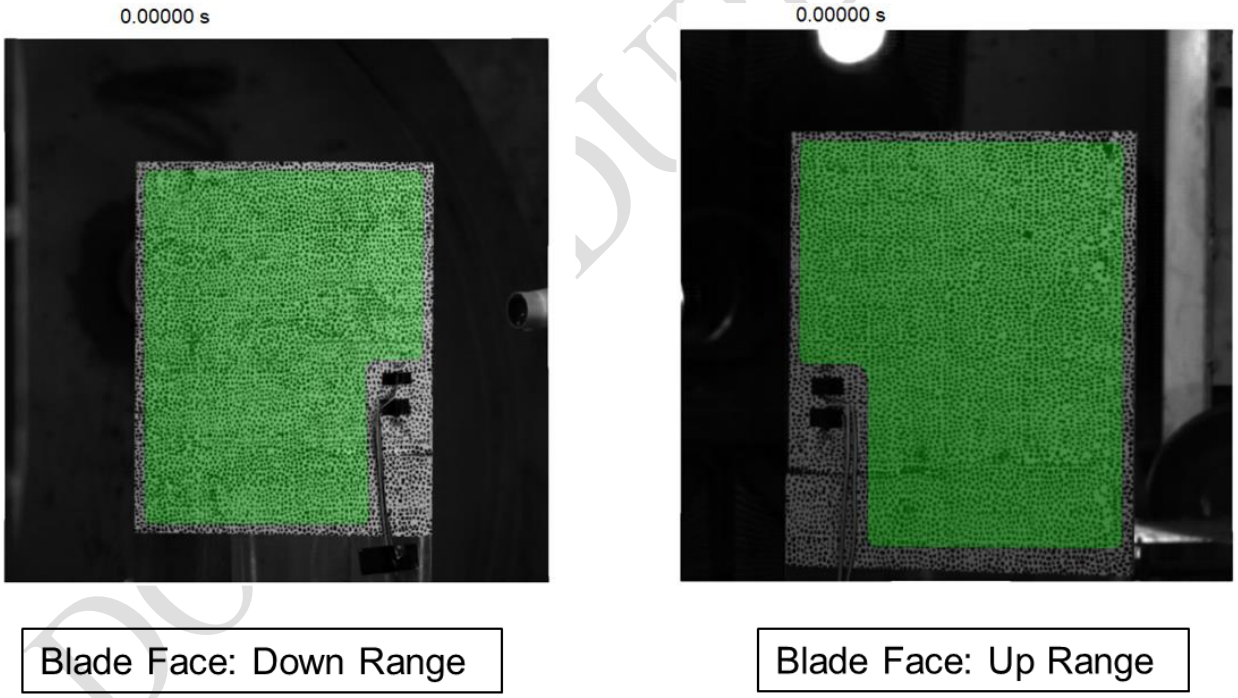

Figure 2.37. Test C50L5-016 selective areas of the blade for DIC processing

Figure 2.38 and Figure 2.39 show the X (blade chord direction) strains, Z (blade span direction) strains, and Y out-of-plane displacement comparison between the DIC test data and the simulation after the impact at t=0.0009s. The data comparison during the impact was not possible due to debris obstruction around the impact area. Although the sUAS debris blockage compromised the

quality of the DIC data, the contour comparison around the impact region shows a good correlation.

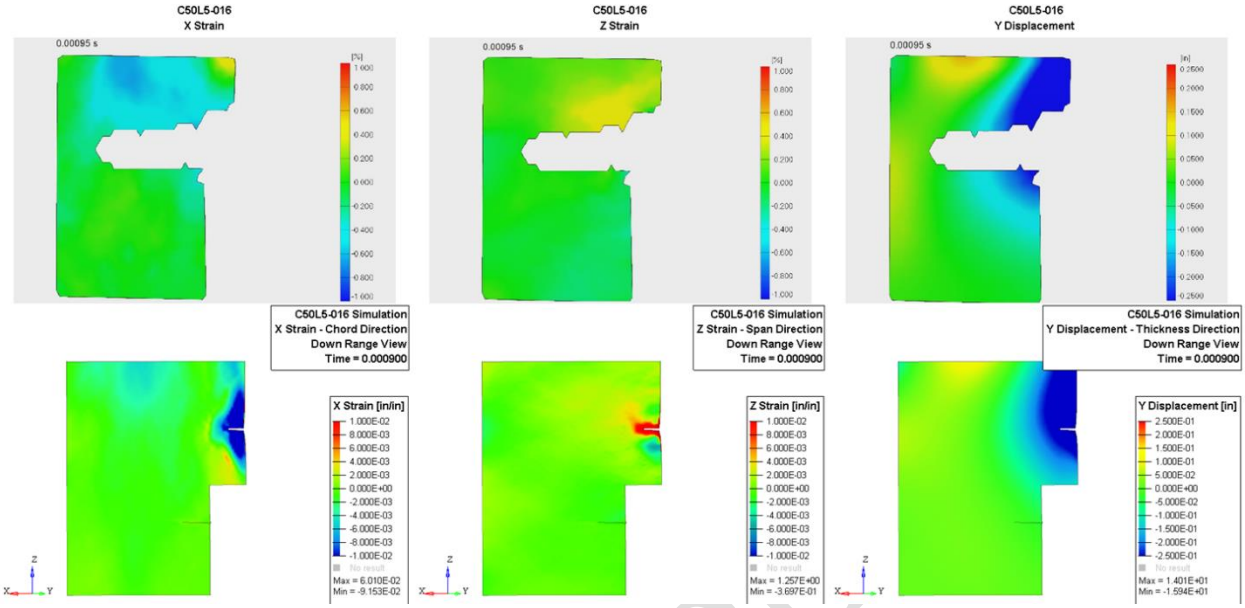

Figure 2.38. Test C50L5-016 DIC comparison on down range face of the blade – Experimental data (top) and simulation (bottom)

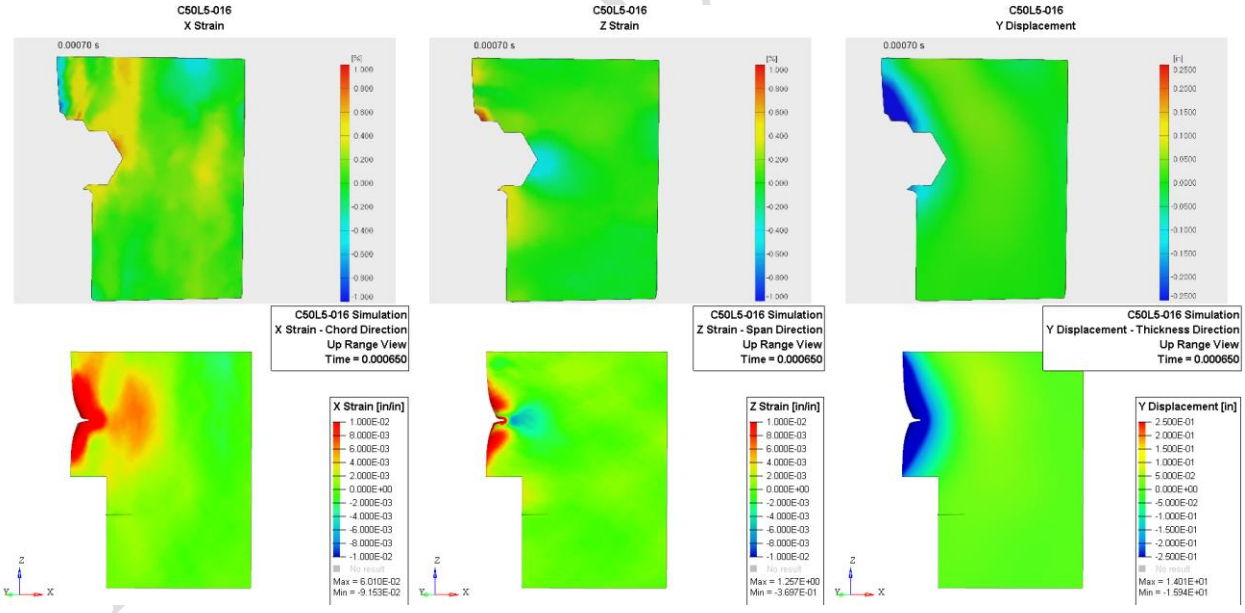

Figure 2.39. Test C50L5-016 DIC comparison on up range face of the blade – Experimental data (top) and simulation (bottom)

In addition to DIC contour data, the time history, showing the resultant displacement for two points (D and G), was obtained and compared with the simulation for all the tests. Figure 2.40 and Figure

2.41 show these points' location and displacement comparison results. The simulation displacement results correlate well with the C50L5 tests.

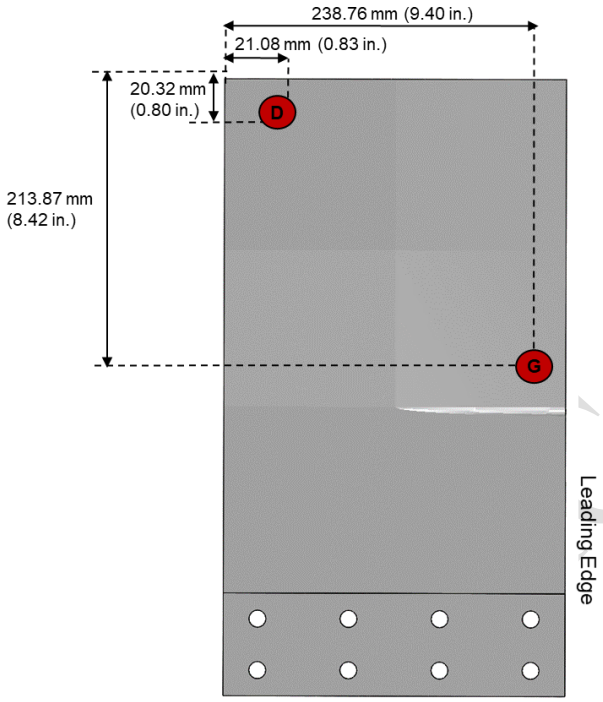

Figure 2.40. Location of points D and G for extraction of DIC resultant displacement time history

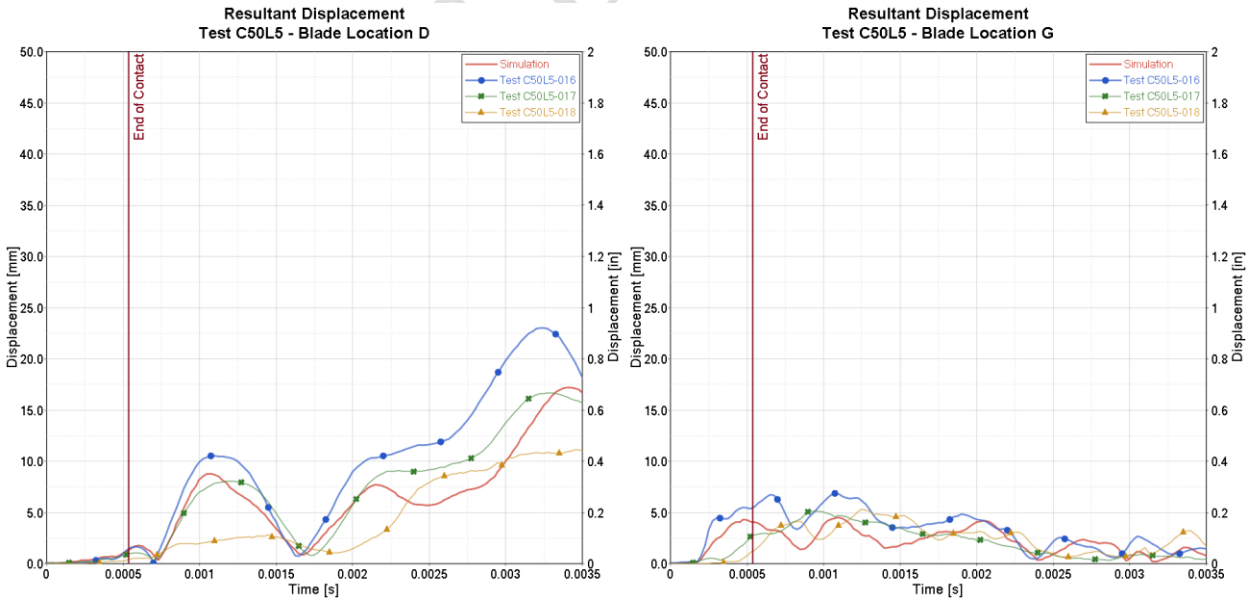

Figure 2.41. Resultant displacement time history comparison between simulation and C50L5 tests

Figure 2.42Figure 2.11 shows the load cells' data comparison between the simulation and the three test repetitions. The data has no filter, and its sampling rate was 1MHz for both the simulation and tests. The simulation results agree with the test data. The strain gages' data comparison was not possible due to corrupted test data.

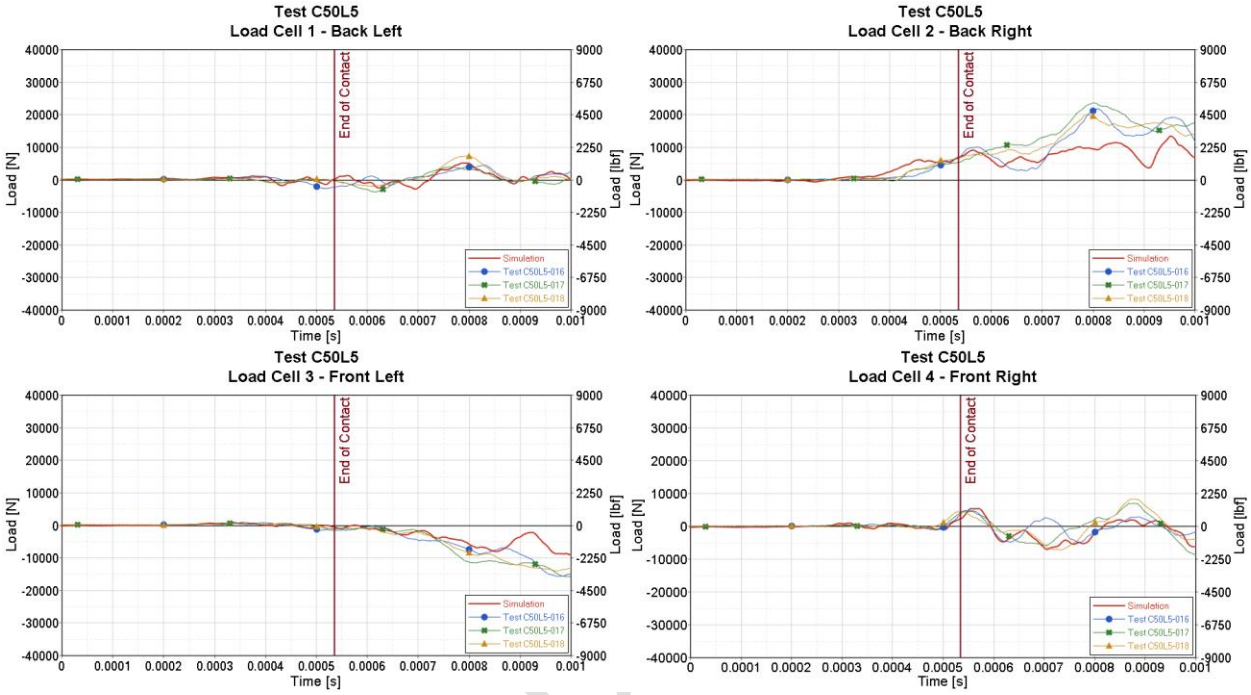

Figure 2.42. Test C50L5 configuration load cells data comparison

The results in this section show a good qualitative correlation between simulation and physical test data in terms of blade damage, loads, and DIC. Thus, for this C50L5 configuration, the camera component of the sUAS is considered validated.

2.1.2.3 FE Information of the Validated UAS Camera

Through the validation efforts described in Section 2.1.2.1 and Section 2.1.2.2 the FE model of the UAS camera is considered validated for the C80L7 and C50L5 test conditions. Figure 2.43 shows the mesh and components of the validated camera, most of which remain the same as those in A3 program [1]. The main update of the camera for A17 program was the addition of the lens and its body to improve the fidelity of camera model for the blade slicing impacts under the current study. Once updated, the three most important A3 camera component level tests were rerun to guarantee that these small changes did not significantly affect the previous validation effort.

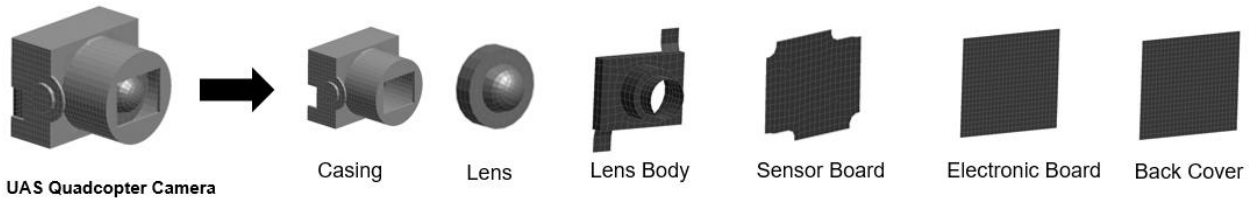

Figure 2.43. Validated FE model of UAS camera

2.1.3 Battery

2.1.3.1 B80A5 Test Configuration

For this test configuration, the battery impacts the leading edge of the titanium blade Opt A-2 at the desired velocity of 289.86 m/s (563.86 knots). The impact location is at 80% radial span of the blade, and the blade is angled at 25 degrees relative to the impact direction. Three repetitions – B80A5-007, B80A5-008, and B80A5-009 – were conducted. Out of these three repetitions, B80A5-007 was selected to corroborate with the simulation. Figure 2.44 shows the schematic setup of the B80A5 test configuration.

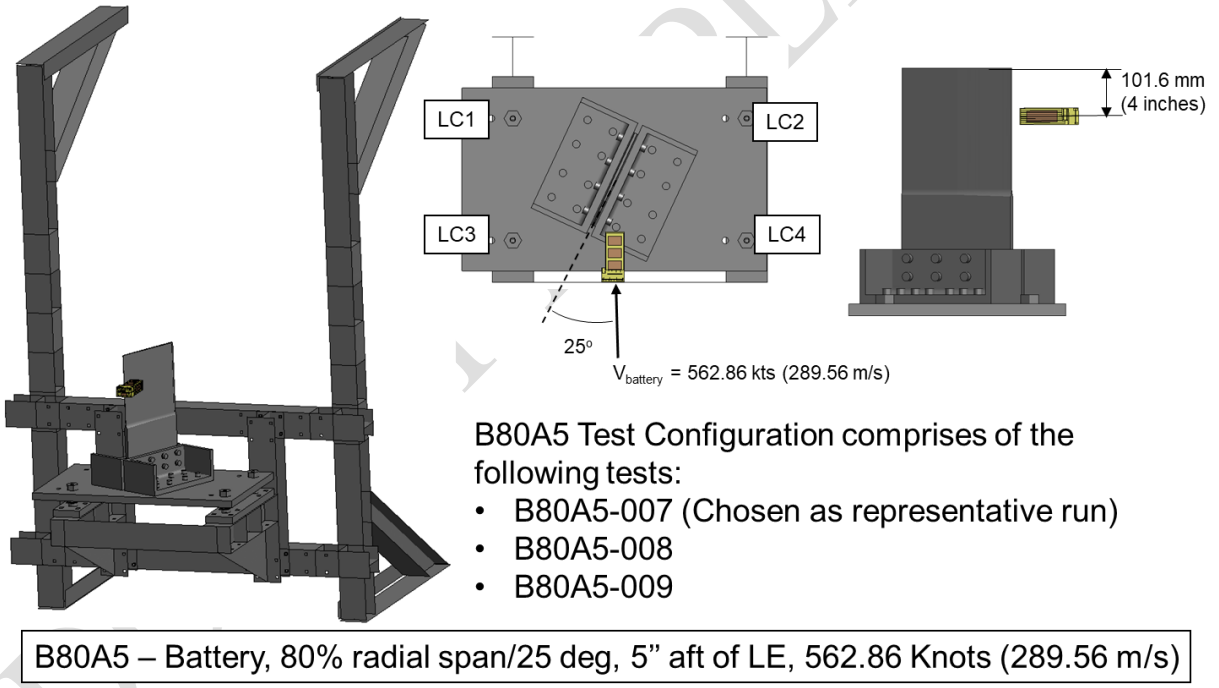

Figure 2.44. B80A5 test configuration setup

To match the conditions of the B80A5-007 test, the FE simulation was set up with the initial projectile velocity of 281.4 m/s (547 knots). The battery's orientation was adjusted to a pitch of 0 degrees, a roll of -3 degrees, and yaw of 6 degrees. The impact location to the battery's c.g. was 105.607 mm (4.158 inches) measured from the top of the blade, which deviated from the desired impact location by 4.01 mm (0.158 inches) shown in Figure 2.44.

Figure 2.45 and Figure 2.46 show the top and side view kinematics comparison between the test and simulation from the start to the end of the impact. Three instances were compared. The first instance at t=0s is the start of the simulation before the impact. The second instance at t=0.0007s is during the impact. The last instance at t=0.0014s is after the impact.

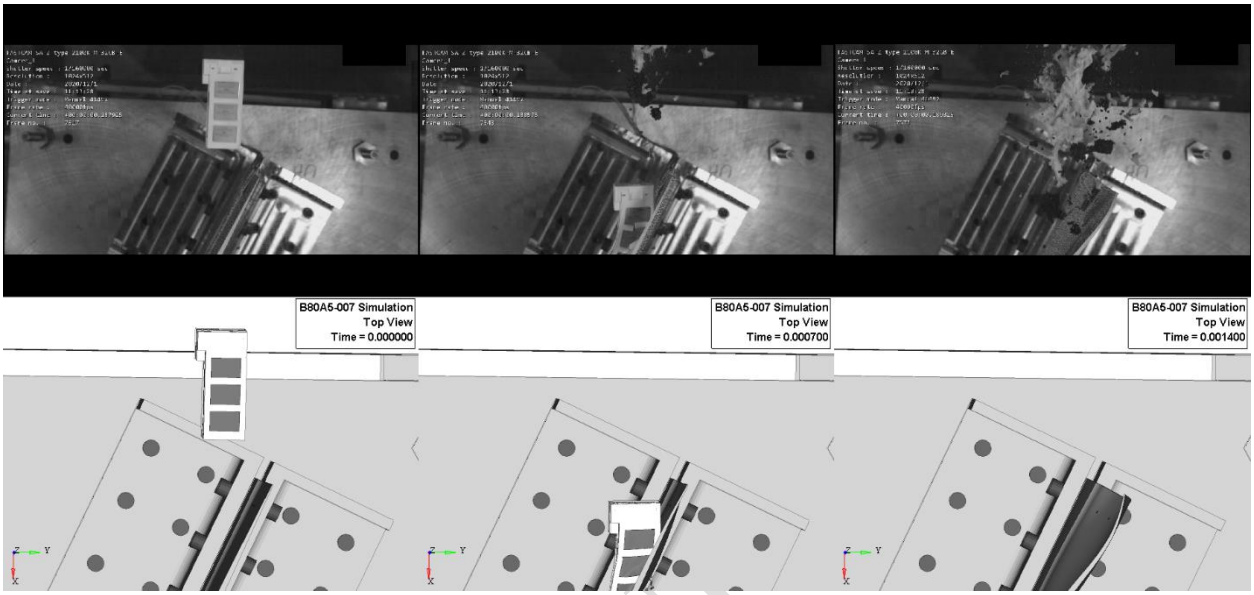

Figure 2.45. B80A5-007 top view kinematics comparison

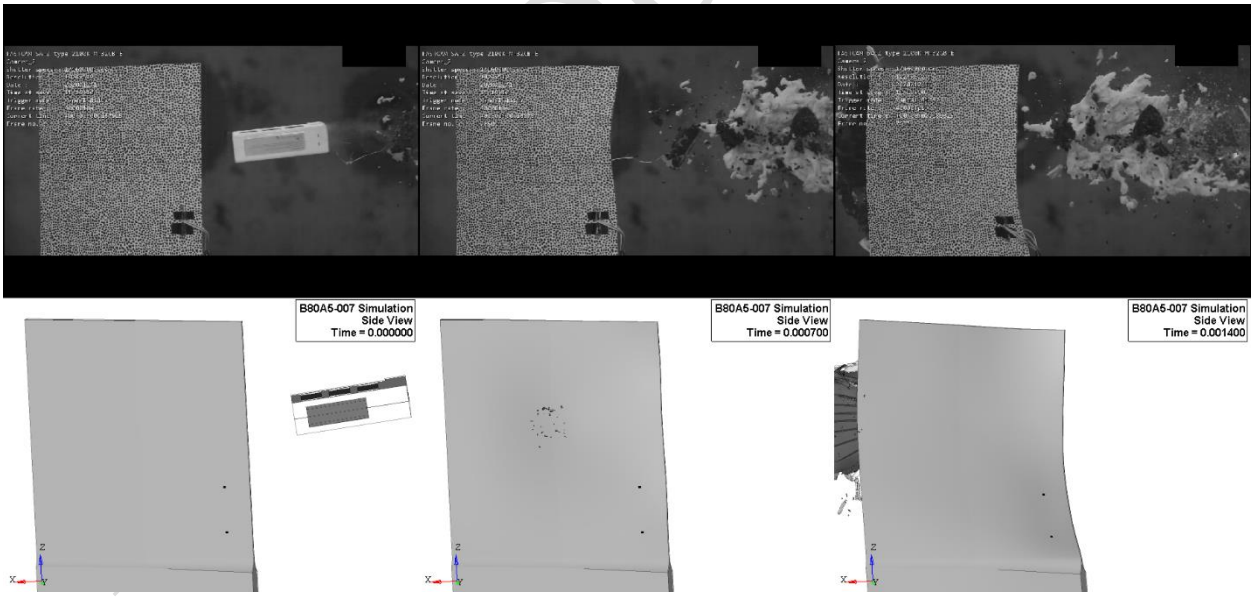

Figure 2.46. B80A5-007 side view kinematics comparison

After 1.4ms of the shown simulation, the blade continued vibrating due to the impact's residual energy. Thus, an additional spring back analysis was performed on the blade to obtain its final deformed shape at its equilibrium state. Figure 2.47 compares the final blade damage after the

spring back FE analysis and the physical test damage. The FE result for the blade's LE shows a good correlation with the final deformed shape of the physical blade's LE.

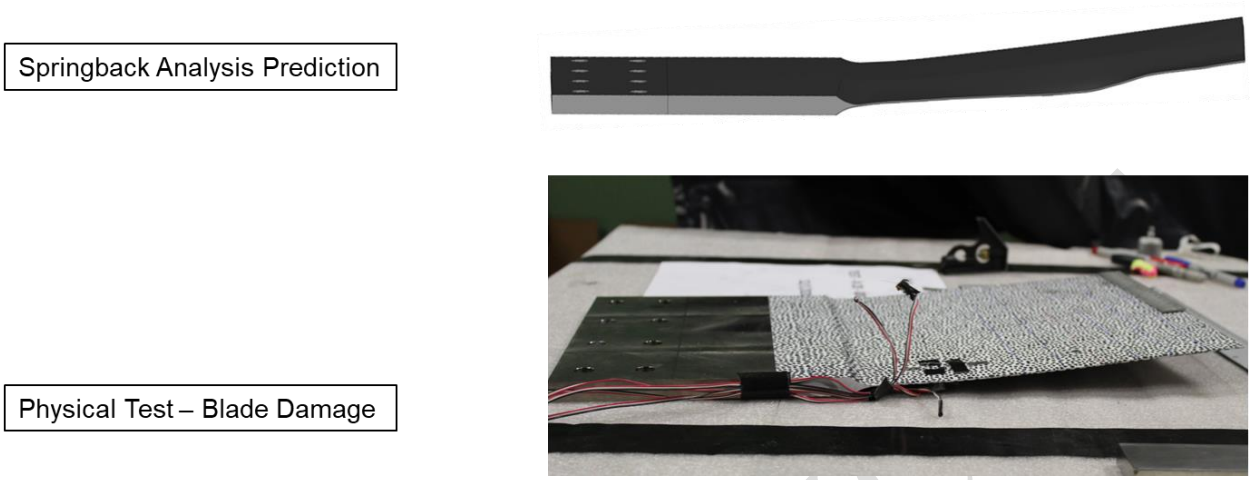

Figure 2.47. Spring back analysis prediction of blade damage vs. physical test damage

Due to the slicing nature of the test, parts of sUAS debris obstructed the blade surfaces during the impact, making it challenging to process the DIC data. Therefore, only partial blade surfaces were selected where DIC data collection was deemed possible. Figure 2.48 shows the selective areas of the blade for the DIC processing in this test B80A5-007.

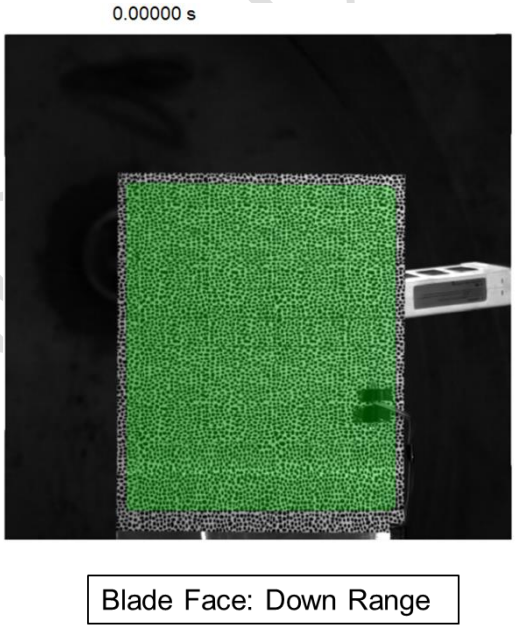

Figure 2.48. Test B80A5-007 selective area of the blade for DIC processing

Figure 2.49 shows the X (blade chord direction) strains, Z (blade span direction) strains, and Y out-of-plane displacement comparison between the DIC test data and simulation during the impact

at t=0.0011s. Although the sUAS debris blockage compromised the quality of the DIC data, the contour comparison around the impact region shows a good correlation.

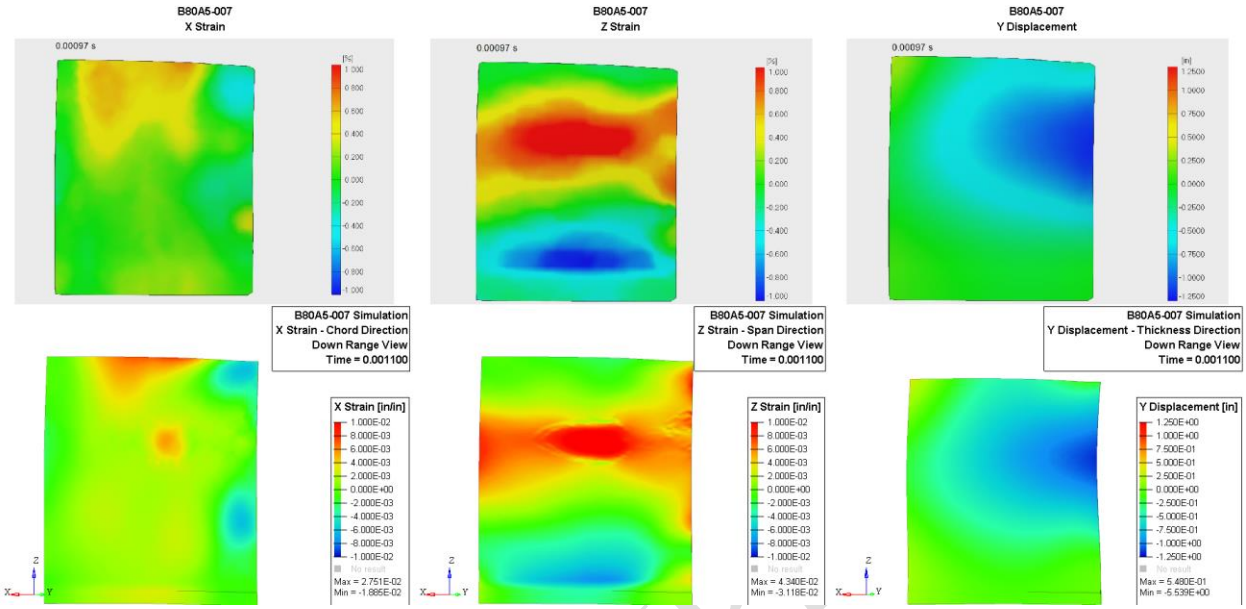

Figure 2.49. Test B80A5-007 DIC comparison on down range face of the blade – Experimental data (top) and simulation (bottom)

In addition to DIC contour data, the time history, showing the resultant displacement for two points (D and G), was obtained and compared with the simulation for all the tests. Figure and Figure 2.51 show the location of these points and the results of the displacement comparison. The simulation displacement correlates well with the B80A5 tests.

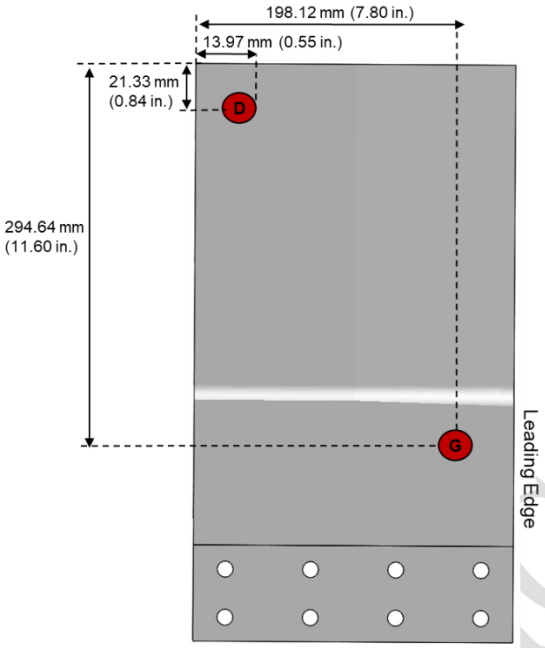

Figure 2.50. Location of points D and G for extraction of DIC resultant displacement time history

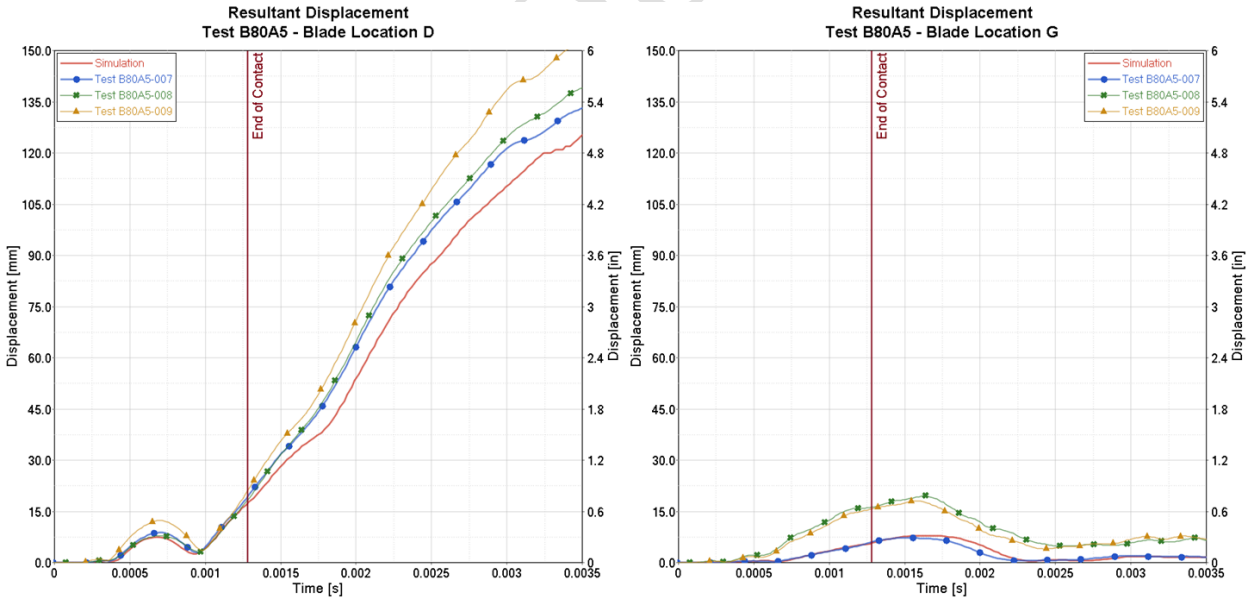

Figure 2.51. Resultant displacement time history comparison between simulation and B80A5 tests

Figure 2.52 shows the load cells' data comparison between the simulation and the three test repetitions. The data has no filter, and its sampling rate was 1MHz for both the simulation and

tests. The simulation results agree with the test data. The strain gages' data comparison was not possible due to corrupted test data.

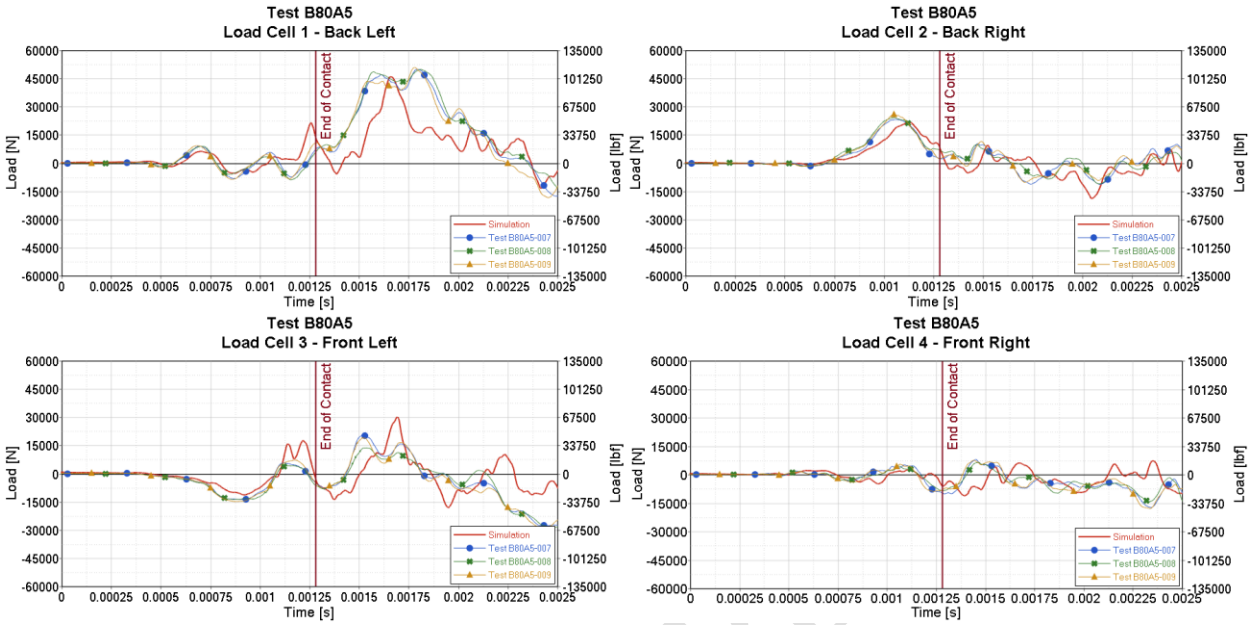

Figure 2.52. Test B80A5 configuration load cells data comparison

The results in this section show a good qualitative correlation between simulation and physical test data in terms of blade damage, loads, and DIC. Thus, for this B80A5 configuration, the battery component of the sUAS is considered validated.

2.1.3.2 B50L7 Test Configuration

For this test configuration, the battery impacts the leading edge of titanium blade Opt B-5 at the modified desired velocity of 289.56 m/s (562.86 kts) instead of the originally desired velocity of 365.76m/s (710.98 kts) because the battery cannot sustain the original velocity without being deformed before the impact. The impact location is at 50% radial span of the blade, and the blade is angled at 30 degrees relative to the impact direction. Three repetitions – B50L7-010, B50L7-011, and B50L7-12 – were conducted. Out of these three repetitions, B50L7-011 was selected to corroborate with the simulation. Figure 2.53 shows the schematic setup of the B50L7 test configuration.

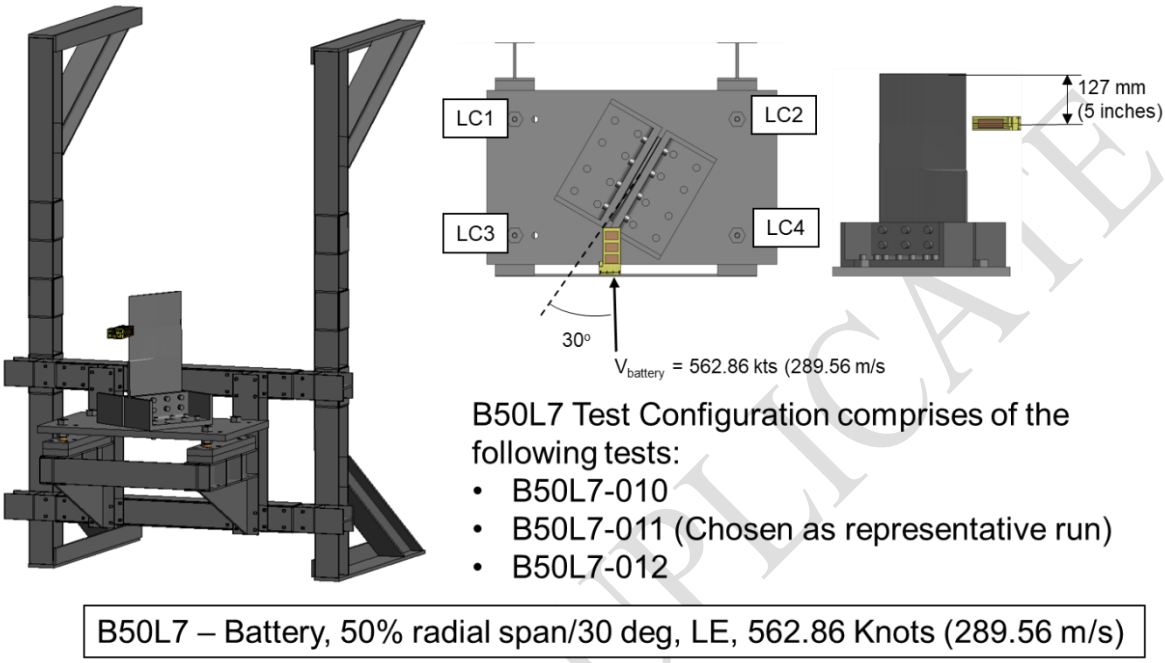

Figure 2.53. B50L7 test configuration setup

To match the conditions of the B50L7-011 test, the FE simulation was set up with the initial projectile velocity of 277.29 m/s (539 knots). The battery's orientation was adjusted to a pitch of -1.1 degrees, a roll of -11.5 degrees, and yaw of 1.4 degrees. The impact location to the battery's c.g. was 127 mm (5 inches) measured from the top of the blade, which matched with the desired impact location shown in Figure 2.53.

Figure 2.54 and Figure 2.55 show the top and side view kinematics comparison between the test and simulation from the start to the end of the impact. Three instances were compared. The first instance at t=0s is the start of the simulation before the impact. The second instance at t=0.00045s is during the impact. The last instance at t=0.0009s is after the impact.

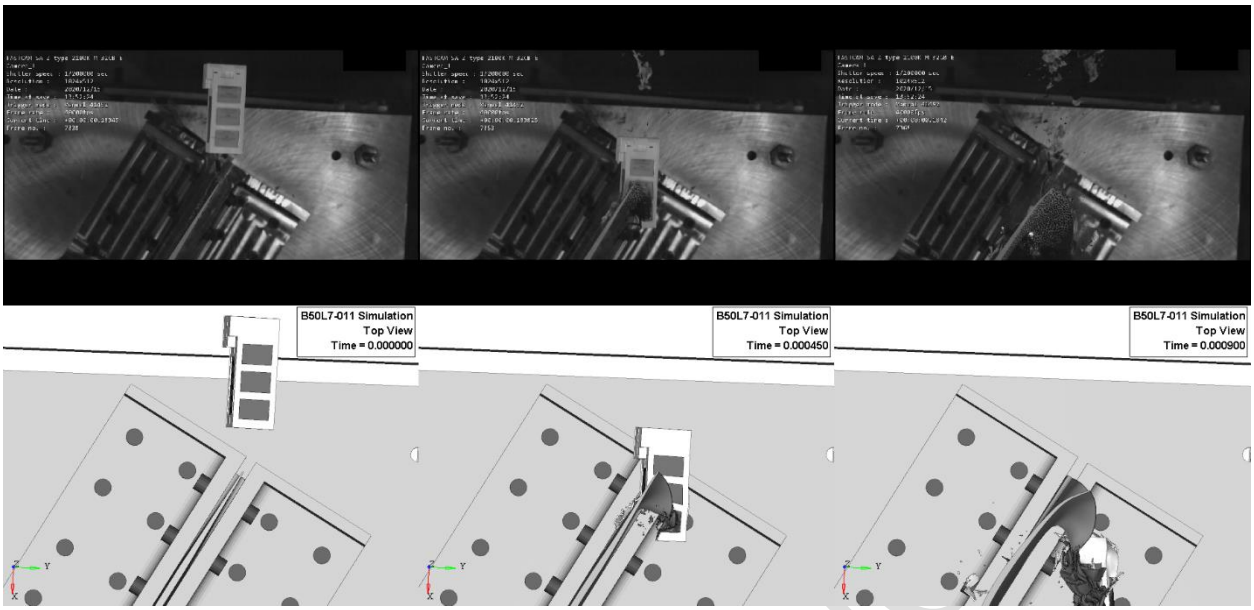

Figure 2.54. B50L7-011 top view kinematics comparison

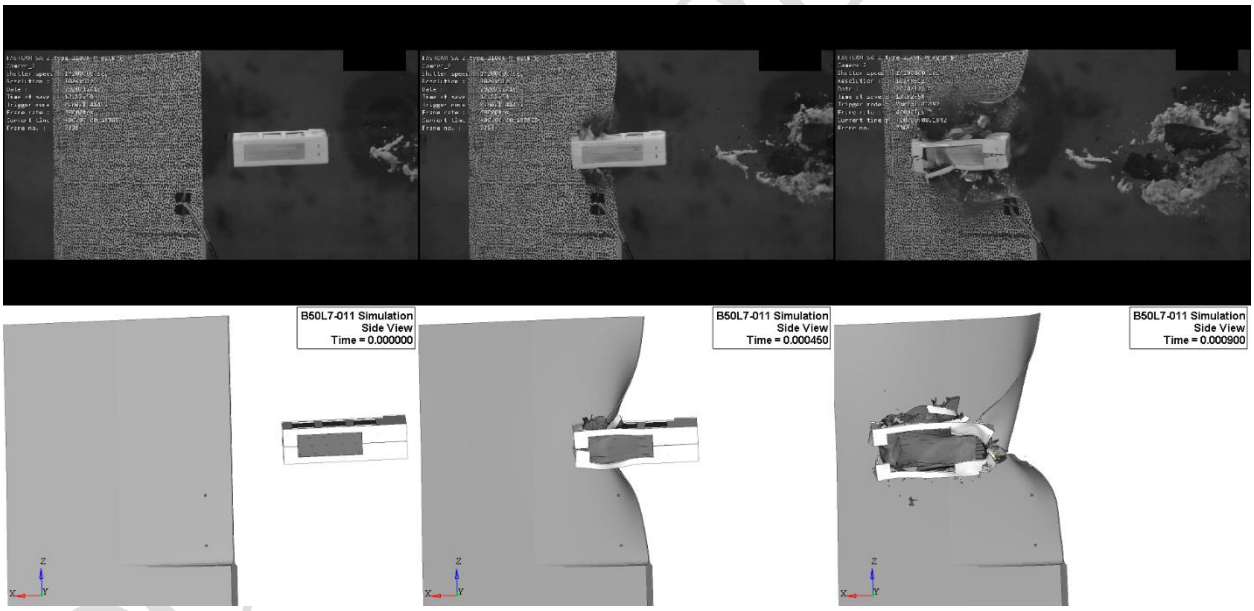

Figure 2.55. B50L7-011 side view kinematics comparison

After 0.9ms of the shown simulation, the blade continued vibrating due to the impact's residual energy. Thus, an additional spring back analysis was performed on the blade to obtain its final deformed shape at its equilibrium state. Figure 2.56 compares the final blade damage after the spring back FE analysis and the physical test damage. The FE result for the blade’s LE shows a good correlation with the final deformed shape of the physical blade's LE.

Figure 2.56. Spring back analysis prediction of blade damage vs. physical test damage

Due to the slicing nature of the test, parts of sUAS debris obstructed the blade surfaces during the impact, making it challenging to process the DIC data. Therefore, only partial blade surfaces were selected where DIC data collection was deemed possible. Figure 2.57 shows the selective areas of the blade for the DIC processing in this test B50L7-011.

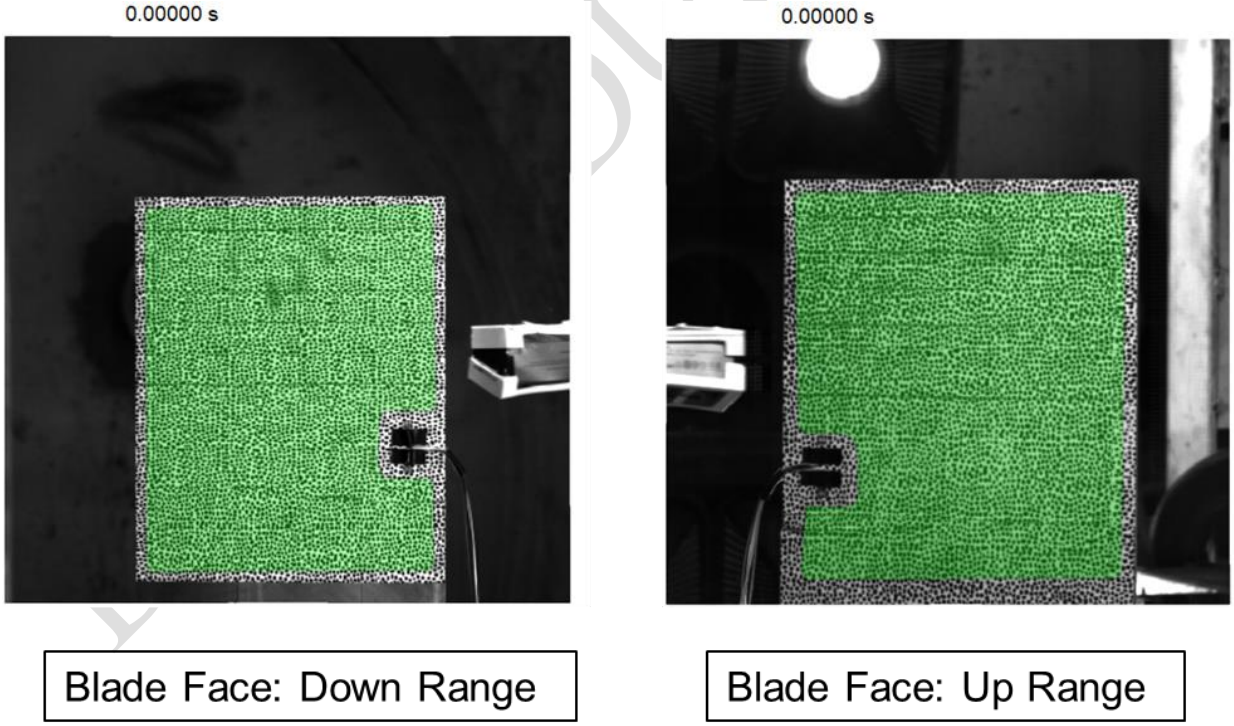

Figure 2.57. Test B50L7-011 selective areas of the blade for DIC processing

Figure 2.58 and Figure 2.59 show the X (blade chord direction) strains, Z (blade span direction) strains, and Y out-of-plane displacement comparison between the DIC test data and simulation during the impact at t=0.00055s. Although the sUAS debris blockage compromised the quality of the DIC data, the contour comparison around the impact region shows a good correlation.

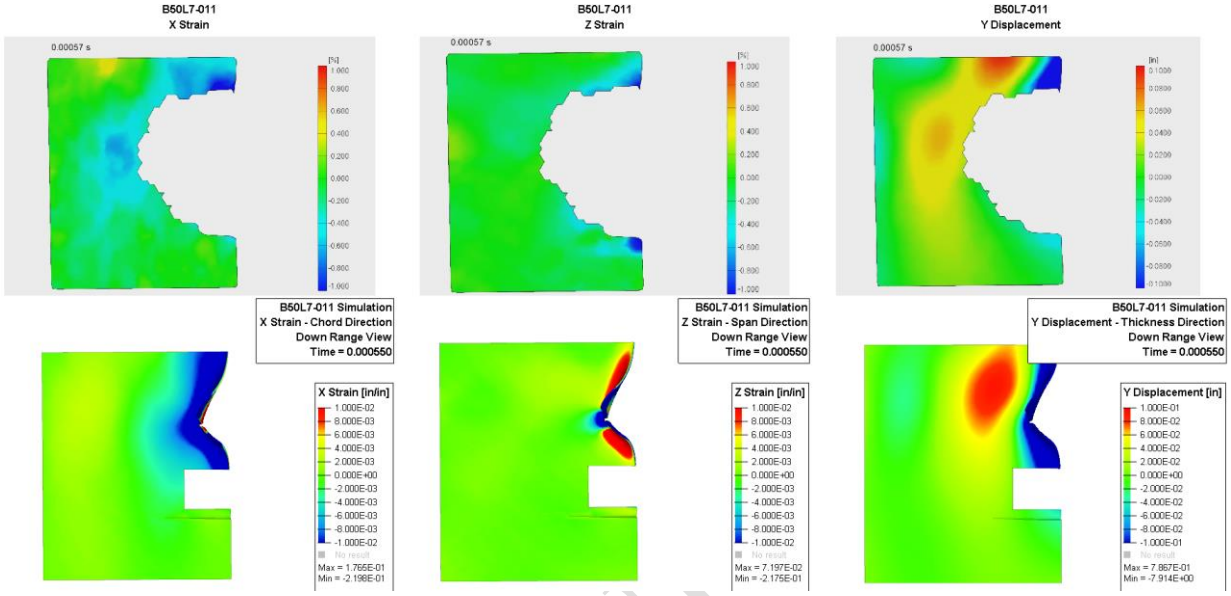

Figure 2.58. Test B50L7-011 DIC comparison on down range face of the blade – Experimental data (top) and simulation (bottom)

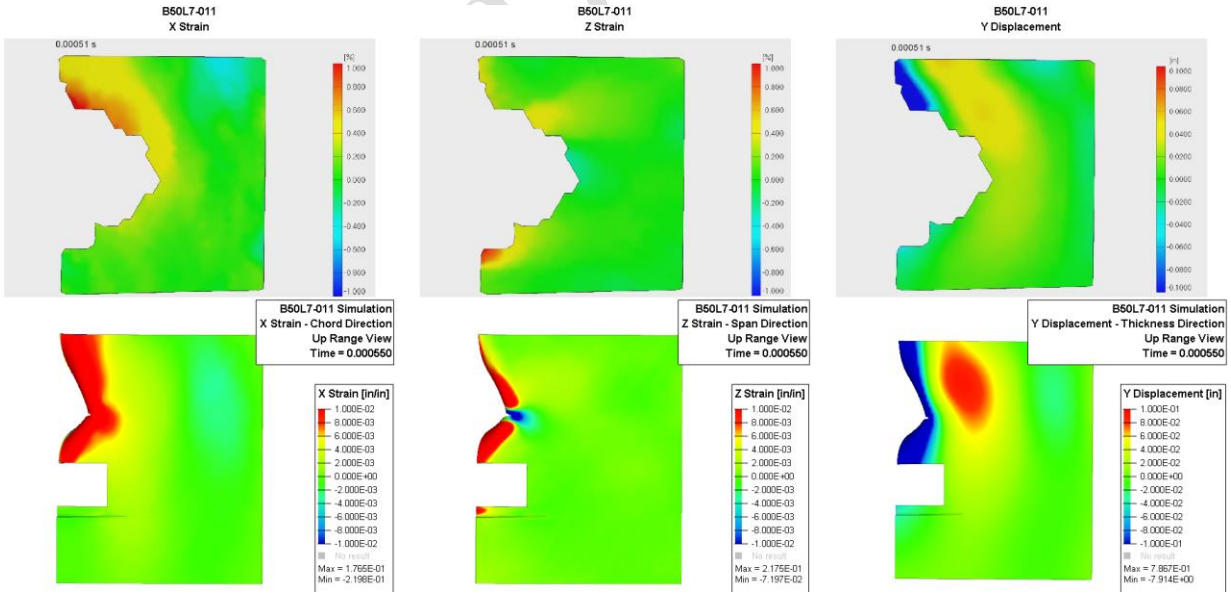

Figure 2.59. Test B50L7-011 DIC comparison on up range face of the blade – Experimental data (top) and simulation (bottom)

In addition to DIC contour data, the time history, showing the resultant displacement for two points (D and G), was obtained and compared with the simulation for all the tests. Figure 2.60 and Figure

2.61 show the location of these points and the results of the displacement comparison. The simulation displacement results agree with the B50L7 tests.

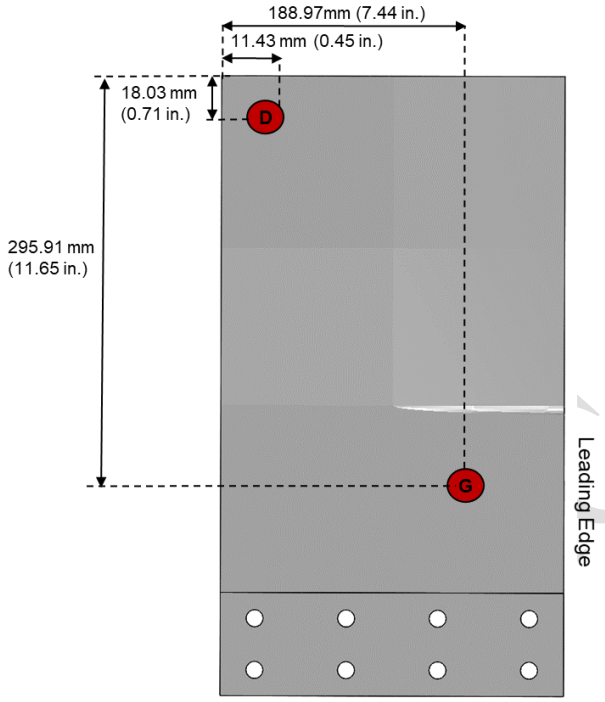

Figure 2.60. Location of points D and G for extraction of DIC resultant displacement time history

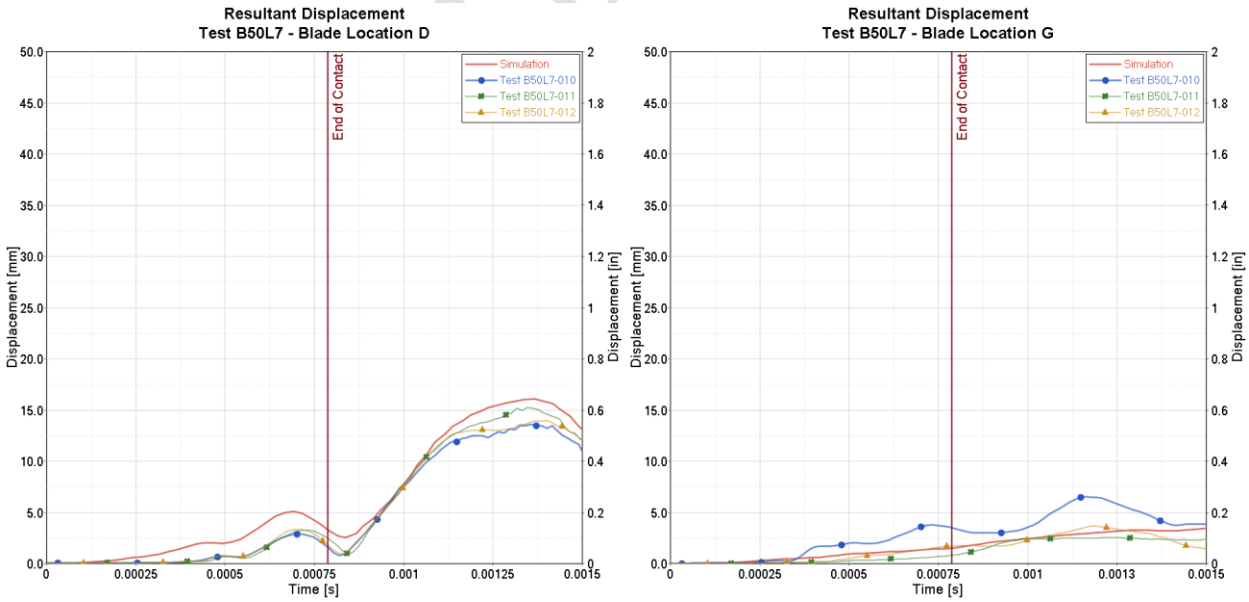

Figure 2.61. Resultant displacement time history comparison between simulation and B50L7 tests

Figure 2.62 shows the load cells' data comparison between the simulation and the three test repetitions. The data has no filter, and its sampling rate was 1MHz for both the simulation and tests. The simulation results agree with the test data. The strain gages' data comparison was not possible due to corrupted test data.

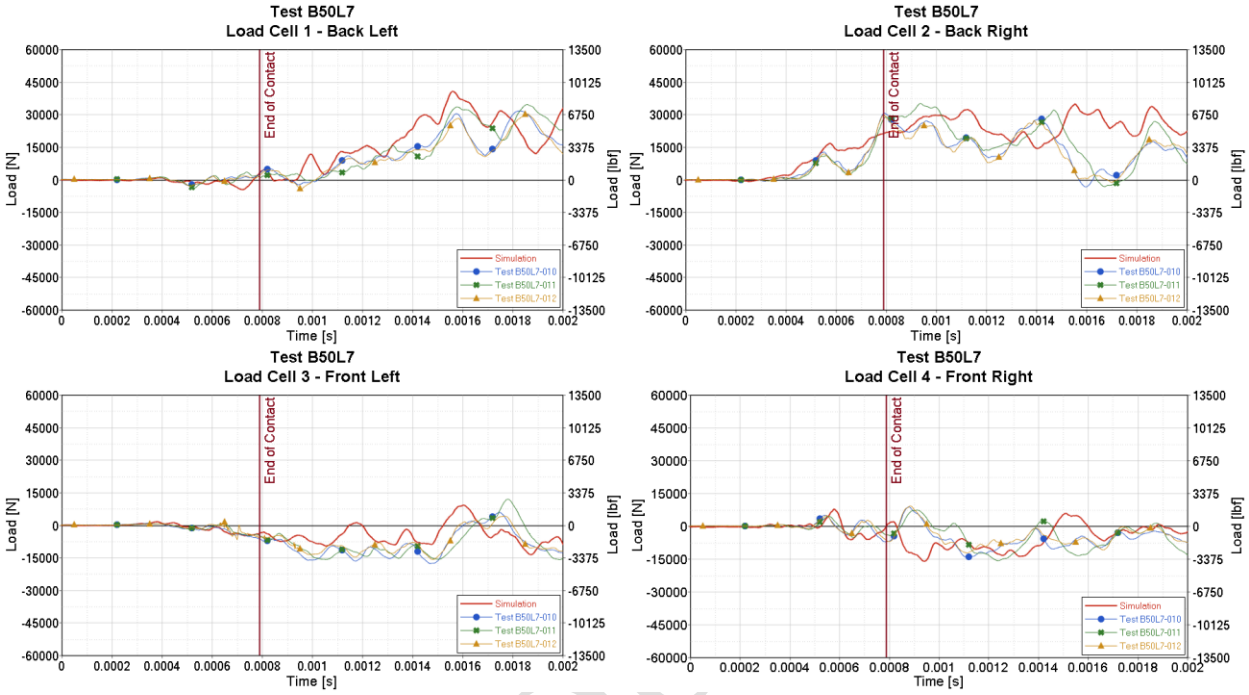

Figure 2.62. Test B50L7 configuration load cells data comparison

The results in this section show a good qualitative correlation between simulation and physical test data in terms of blade damage, loads, and DIC. Thus, for this B50L7 configuration, the battery component of the sUAS is considered validated.

2.1.3.3 FE Information of the Validated UAS Battery

Through the validation efforts described in Section 2.1.3.1 and Section 2.1.3.2 the FE model of the UAS battery is considered validated for the B80A5 and B50L7 test conditions. Figure 2.63 shows the mesh and components of the validated battery, some of which remain the same as those in A3 program [1]. The main updates of the battery for A17 program were the addition of the internal electronics and divisions of battery cells to capture the buckling behavior better. Once updated, the three most important A3 battery component level tests were rerun to guarantee that these small changes did not significantly affect the previous validation effort.

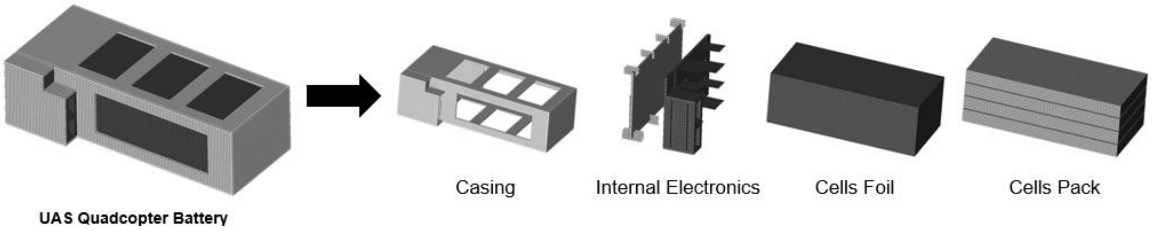

Figure 2.63. Validated FE model of UAS battery

2.2 FULL-SCALE LEVEL

Following the Building Block Approach, after the main sUAS components are validated, the next step is to validate the complete sUAS. Table 4 shows the full-scale test matrix. Similar to the component level test matrix, there are two test configurations at 80% and 50% radial span impact locations on the blades, respectively. Each configuration has three test repetitions for a total of 6 tests. The nomenclature of the test case follows the same principles as the components tests described in the previous section. The only difference in this section is the first letter of the test case name, which is the letter D (short for DJI) for all the tests.

Table 4. Full scale test matrix

Test Case	Test Number	Projectile	Target	Span (%)	Relative Angle (°)	Impact Location	Designed Speed	Performed Speed
D80L7-001	21-82	DJI Body	Ti Blade OPT A-2 Rev 4	80	25	LE	425 kts (218.64 m/s)	406 kts (208.86 m/s)
D80L7-002	21-83	DJI Body	Ti Blade OPT A-2 Rev 4	80	25	LE	425 kts (218.64 m/s)	394 kts (202.69 m/s)
D80L7-003	21-84	DJI Body	Ti Blade OPT A-2 Rev 4	80	25	LE	425 kts (218.64 m/s)	434 kts (223.27 m/s)
D50L5-004	21-52	DJI Body	Ti Blade OPT B-5 Rev 3	50	30	LE	425 kts (218.64 m/s)	433 kts (222.75 m/s)
D50L5-005	21-56	DJI Body	Ti Blade OPT B-5 Rev 3	50	30	LE	425 kts (218.64 m/s)	419 kts (215.55 m/s)
D50L5-006	21-85	DJI Body	Ti Blade OPT B-5 Rev 3	50	30	LE	425 kts (218.64 m/s)	428 kts (220.18 m/s)

Figure 2.64 and Table 5 show the projectile (DJI Phantom 3 body) geometry and its detailed specifications. The DJI body excludes the propellers, legs, gimbal, and camera assembly normally present in a full DJI Phantom 3.

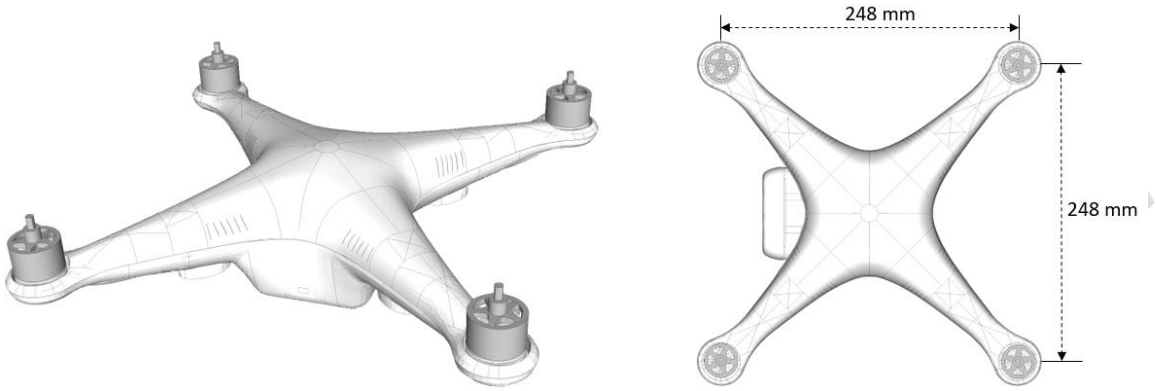

Figure 2.64 Geometry features of the DJI Phantom 3 body

Table 5. Specifications of the DJI Phantom 3 body

Mass	930 g	2.05 lb.
Diagonal (center of the motors)	350 mm	13.8 in
Height	98 mm	3.86 in
Max. Motor Speed	1,240 rad/s	11,840 rpm
Motors	4x brushless DC motors; mass: 54 g	
Battery	4x LiPo cells; capacity: 4480 mAh; mass: 363 g	

Table 6 and Figure 2.65 show the targets' details and geometry, respectively.

Table 6. Target details

Target Description	Material	Target size [in]	Instrumentation	Quantity Needed
Titanium Blade Opt A-2 Rev 4(for 80% radial impact)	Ti-6Al-4V	10x18 (including 3'' extension for bolts connection)	Linear Strain Gauge and DIC	3
Titanium Blade Opt B-5 Rev 3(for 50% radial impact)	Ti-6Al-4V	10x18 (including 3'' extension for bolts connection)	Linear Strain Gauge and DIC	3

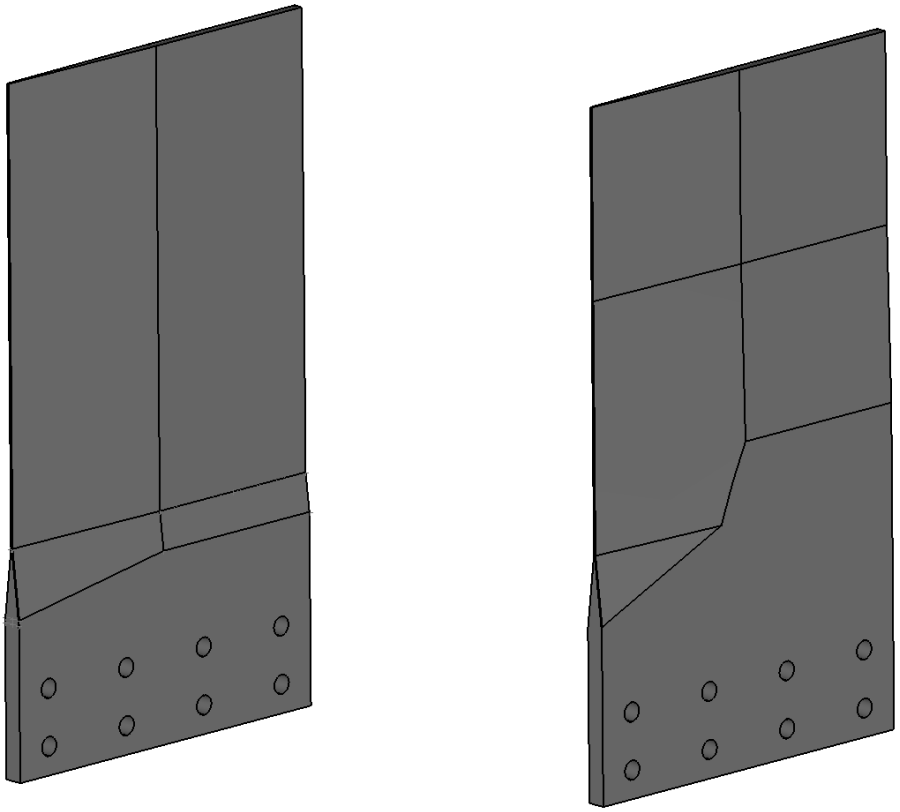

Figure 2.65 Titanium blade opt A-2 rev 4(left) and titanium blade opt B-5 rev 3(right)

2.2.1.1 D80L7 Test Configuration

For this test configuration, the sUAS body impacts the leading edge of the titanium blade Opt A-2 rev 4 at the desired velocity of 218.64 m/s (425 knots). The impact location is at 80% radial span of the blade, and the blade is angled at 25 degrees relative to the impact direction. Three repetitions – D80L7-001, D80L7-002, and D80L7-003 – were conducted. Due to the high variability of the sUAS trajectory from launch for all the tests, they were all selected to corroborate with simulations. Figure 2.66 shows the schematic setup of the D80L7 test configuration.

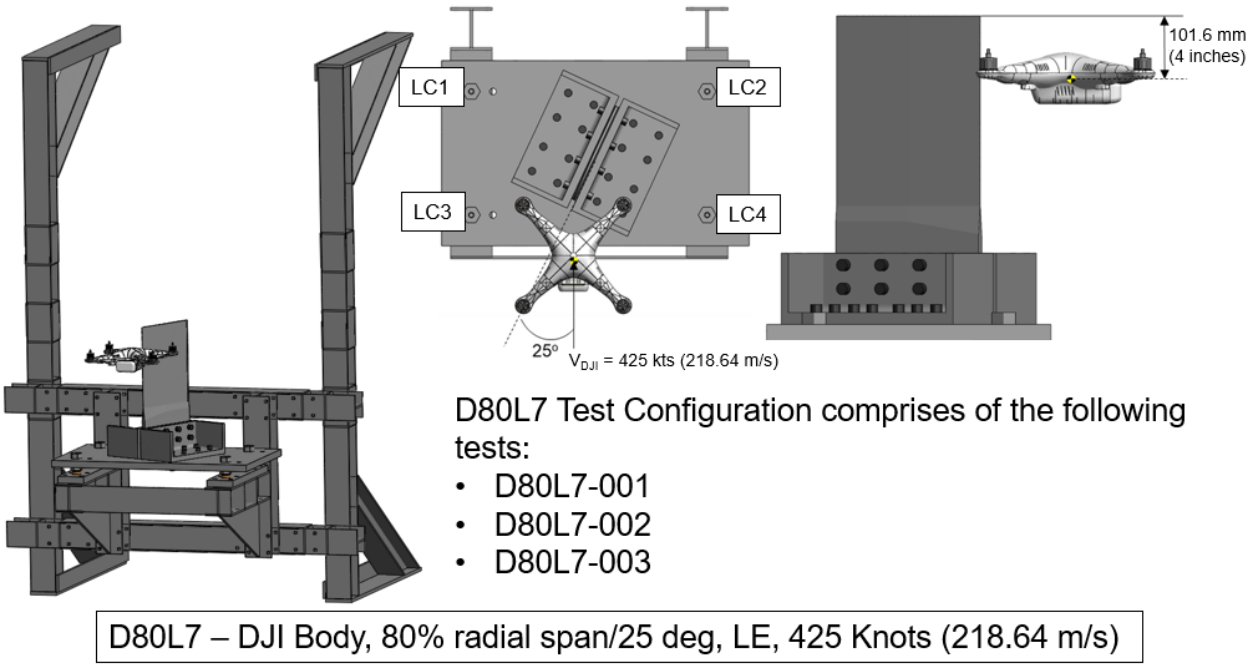

Figure 2.66. D80L7 test configuration setup

The simulations were set up to match the testing conditions for all the tests shown in Table 7.

Table 7. D80L7 test conditions

Test Case	Actual Impact Velocity	sUAS Pitch	sUAS Roll	sUAS Yaw	Impact Location w.r.t sUAS C.G.
D80L7-001	406 kts (208.86 m/s)	-45 deg	25 deg	-8 deg	2.5 in. from the top of the blade
D80L7-002	394 kts (202.69 m/s)	46 deg	25 deg	25 deg	Only one arm of the sUAS hit the blade LE
D80L7-003	434 kts (223.27 m/s)	-37 deg	-11.6 deg	6.4 deg	2.5 in. from the top of the blade

Figure 2.67 to Figure 2.69 and Figure 2.70 to Figure 2.72 show the top and side view kinematics comparison between the D80L7 tests and simulations from the start to the end of the impact. Three instances were compared. The first instance at t=0s is the start of the simulation before the impact. The second instance at t=0.001s is during the impact. The last instance at t=0.002s is after the impact.

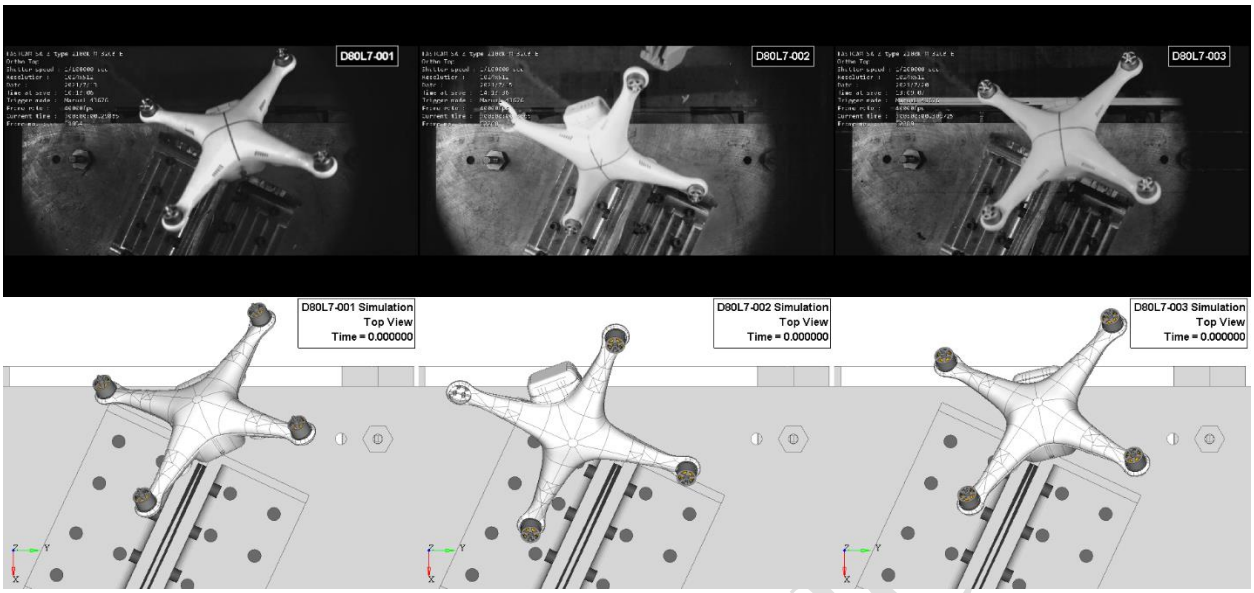

Figure 2.67. D80L7 tests top view kinematics comparison at t=0s

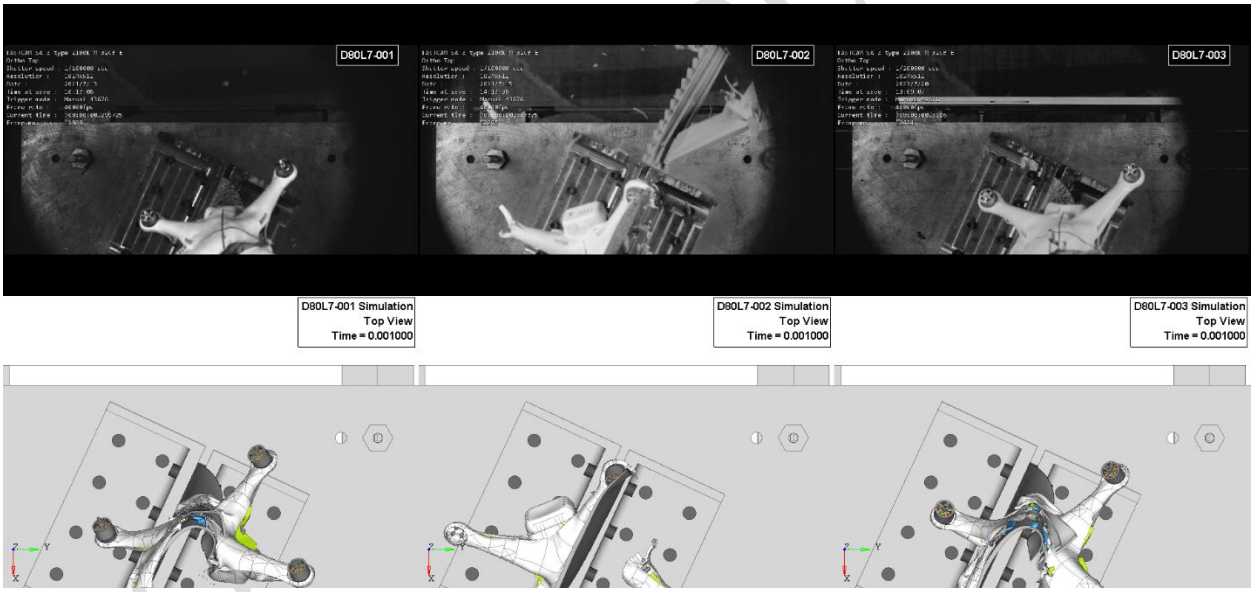

Figure 2.68. D80L7 tests top view kinematics comparison at t=0.001s

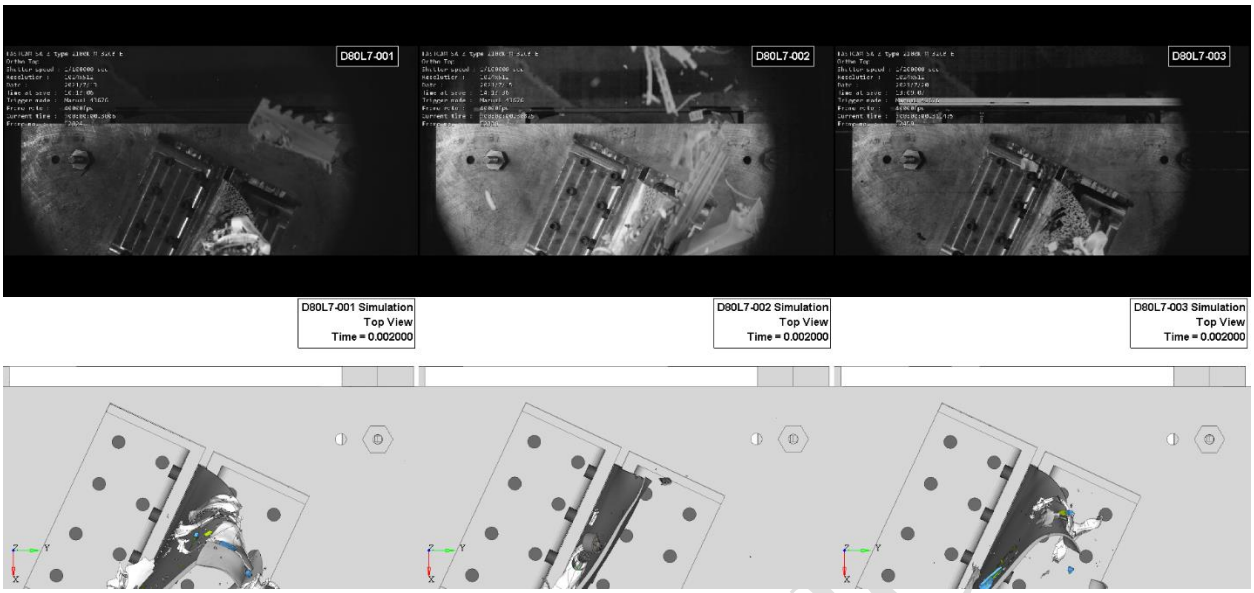

Figure 2.69. D80L7 tests top view kinematics comparison at t=0.002s

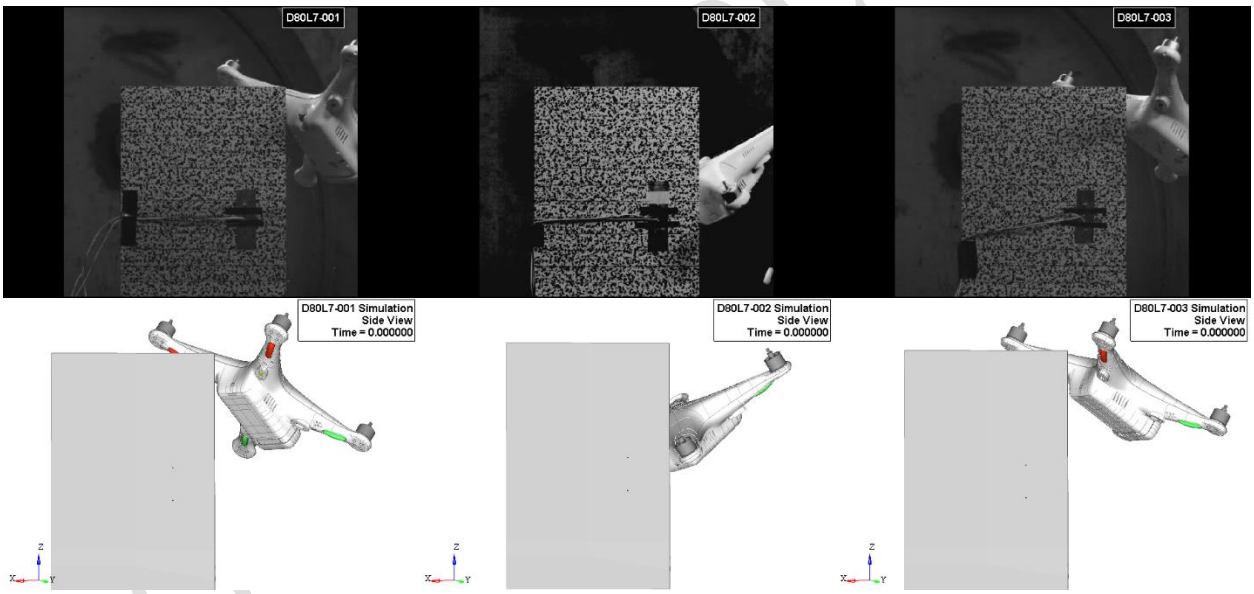

Figure 2.70. D80L7 tests side view kinematics comparison at t=0s

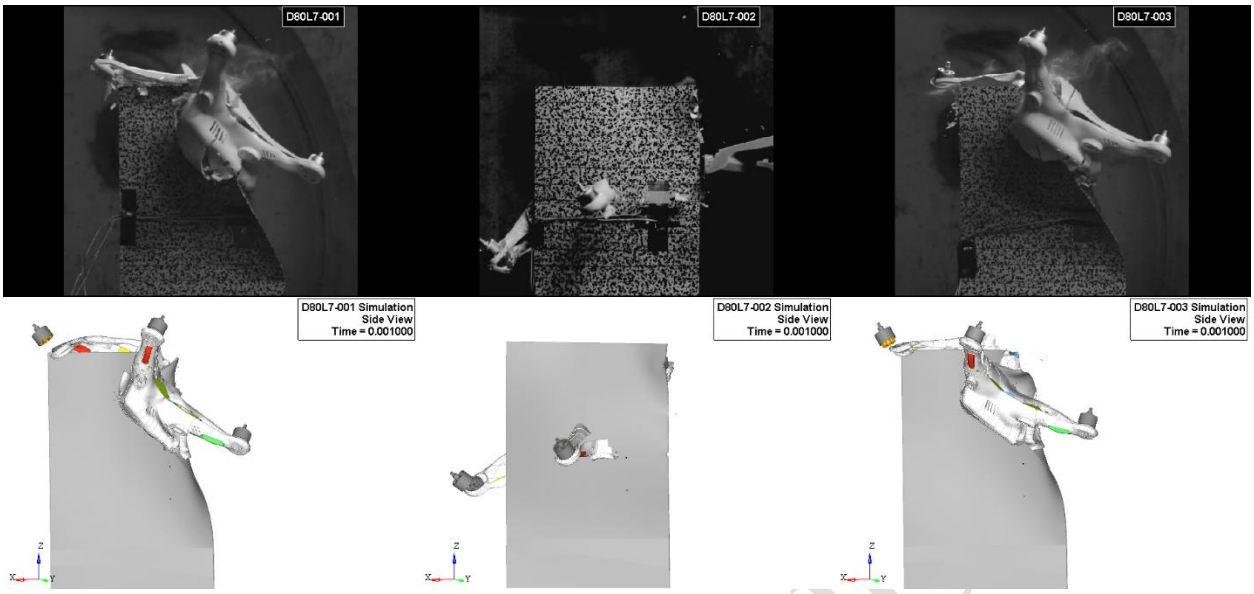

Figure 2.71. D80L7 tests side view kinematics comparison at t=0.001s

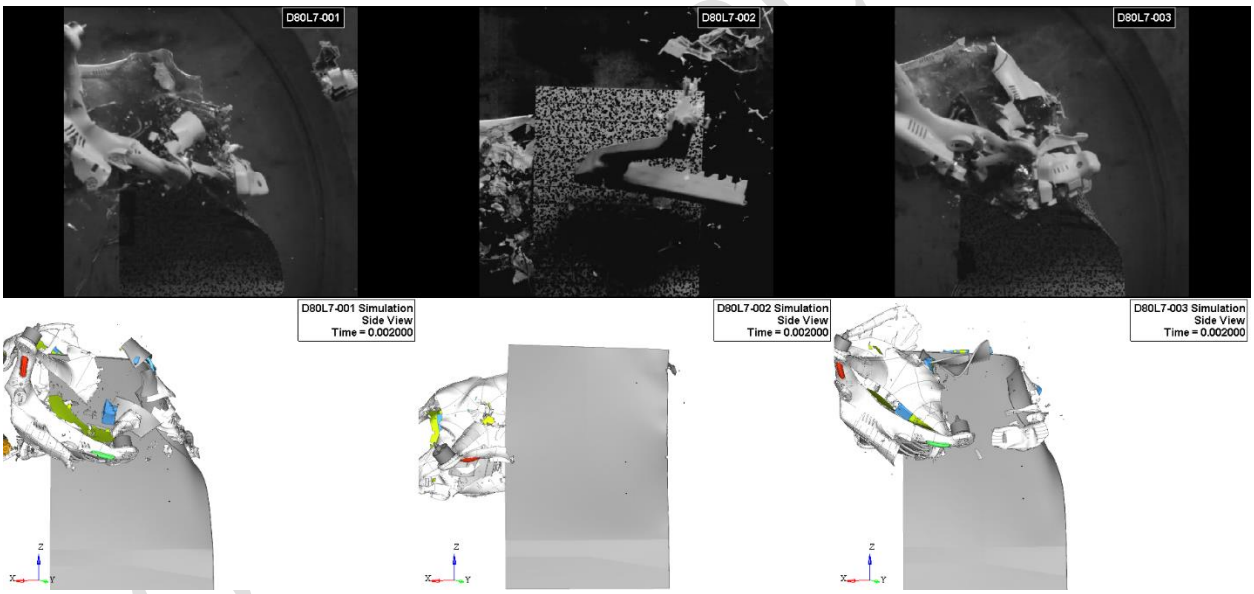

Figure 2.72. D80L7 tests side view kinematics comparison at t=0.002s

After 2ms, shown in all the simulations, the blade continued vibrating due to the impact's residual energy. Thus, an additional spring back analysis was performed on the blade to obtain its final deformed shape at its equilibrium state. Figure 2.73 compares the final blade damage between the spring back analysis prediction and the physical test damage for all the tests. The FE result for the blade's LE shows a good correlation with the final deformed shape of the physical blade's LE.

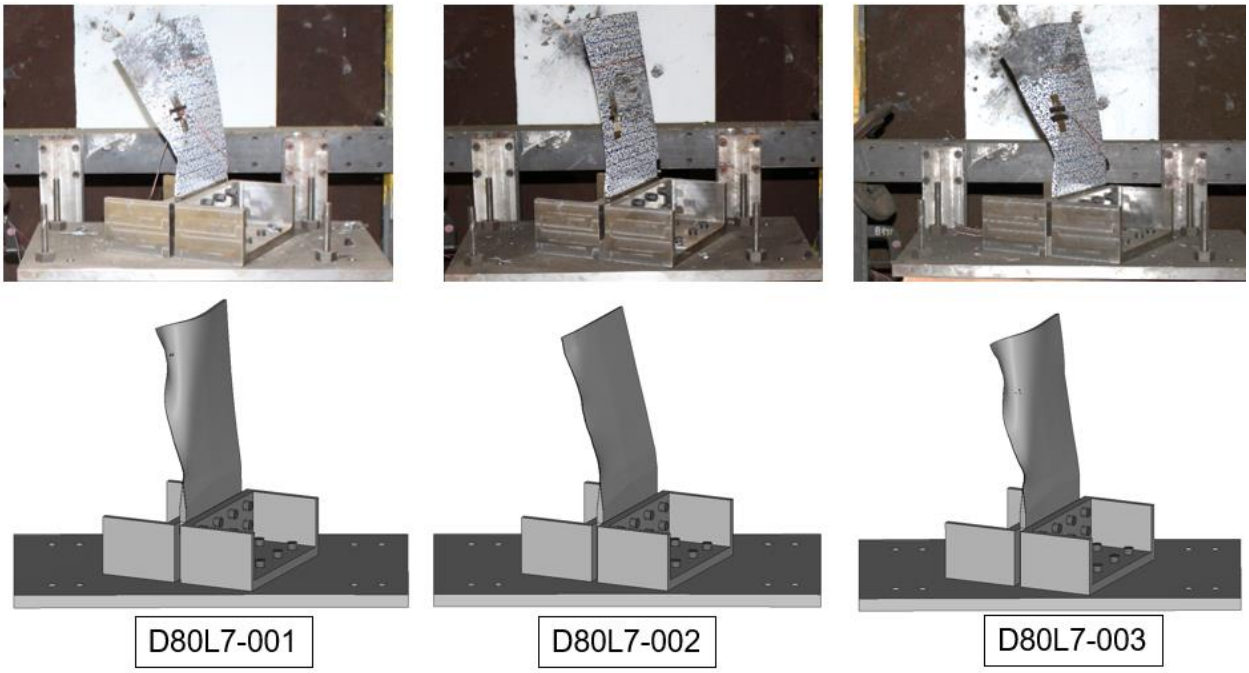

Figure 2.73. Spring back analysis prediction of blade damage vs. physical test damage for all D80L7 tests

Similar difficulty observed in components level tests in processing DIC data was present for the full-scale tests. In fact, the sUAS body being larger than its components, produced much more debris that covered most of the blade surface during the impact obstructing the DIC camera views. As a result, it was not possible to obtain good DIC contour data to compare with the simulations. Nevertheless, the time history of the resultant displacements from specific points on the blade surfaces was obtained and used to compare the simulation and the three D80L7 tests where possible. Due to the debris obstruction, the complete test time history curves were sometimes unavailable for the entire impact duration. Figure 2.74 to Figure 2.81 show these points' locations and the displacement comparison results. The comparison of point B (close to the impact area) shows some discrepancies after the impact with the sUAS because of the low fidelity DIC data in the impact area, and the LE damage, although similar, is not identical between the test and simulation. Overall, the simulation displacement agrees well with the D80L7 tests for the duration of the impact. After the end of the contact, depending on the debris obstructions, some test data points show noticeable difference to the simulation results.

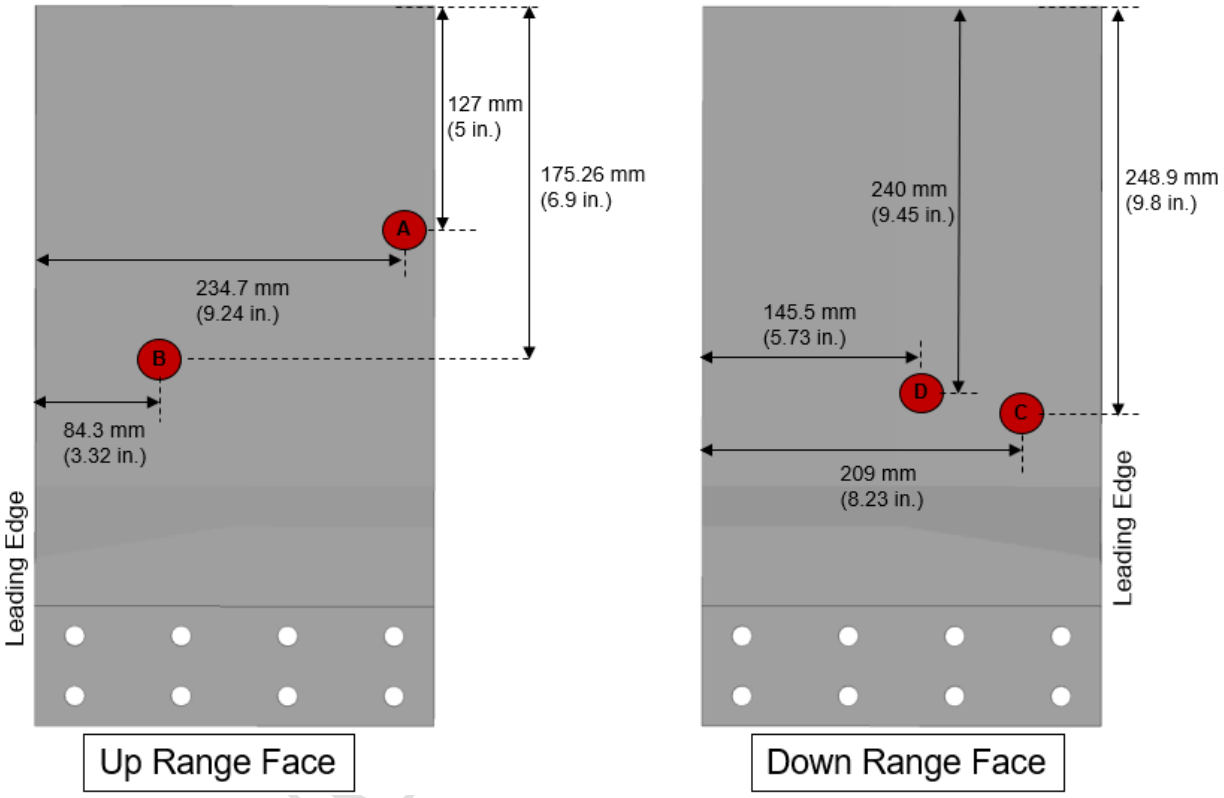

Figure 2.74. Location of points A,B,C, and D for extraction of DIC resultant displacement time history for test D80L7-001

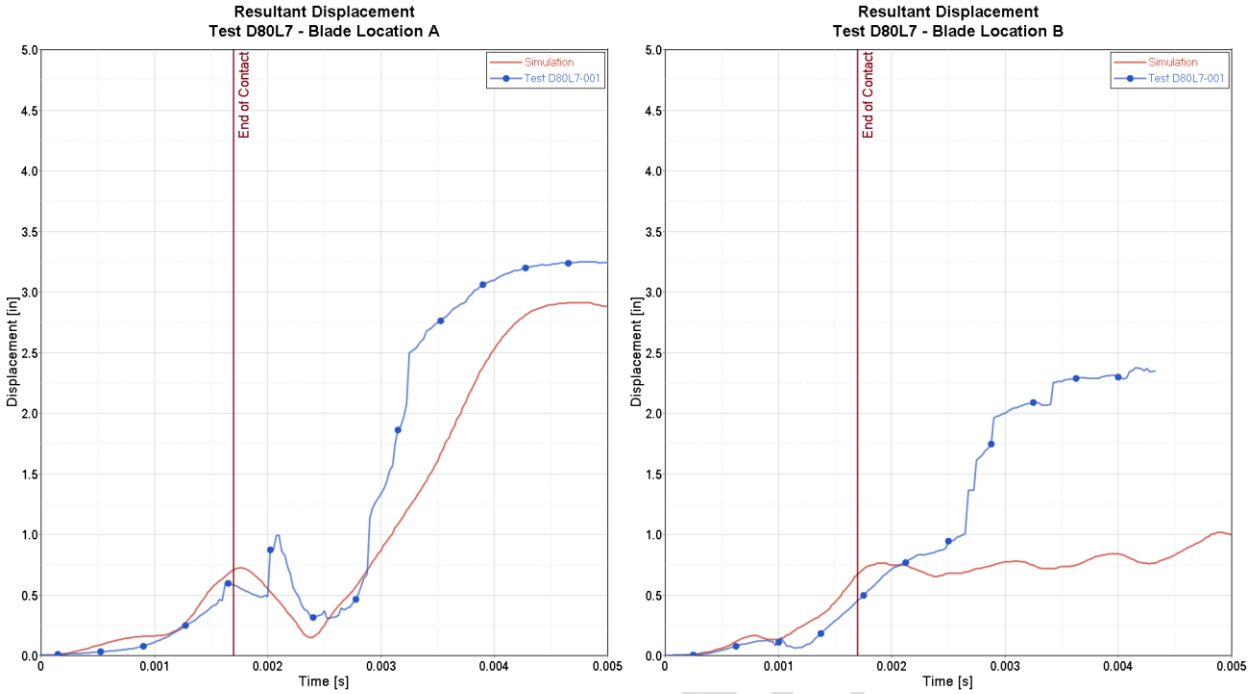

Figure 2.75. Resultant displacement of location A and B time history comparison between simulation and test D80L7-001

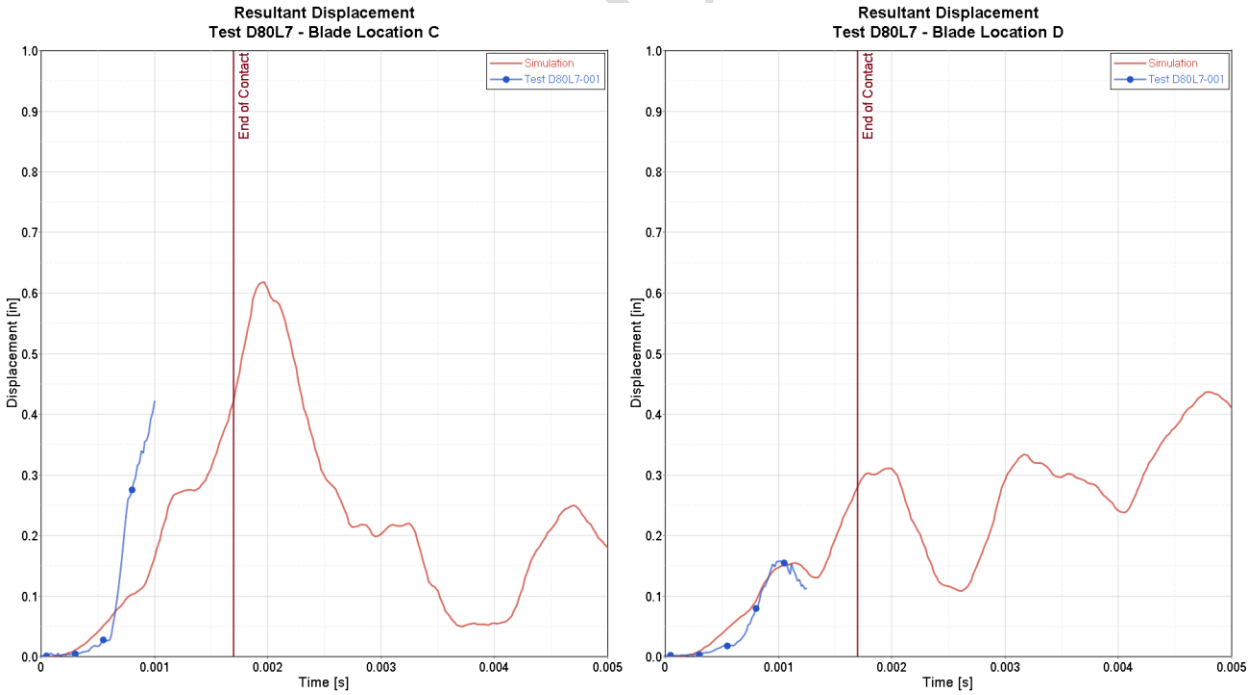

Figure 2.76. Resultant displacement of location C and D time history comparison between simulation and test D80L7-001

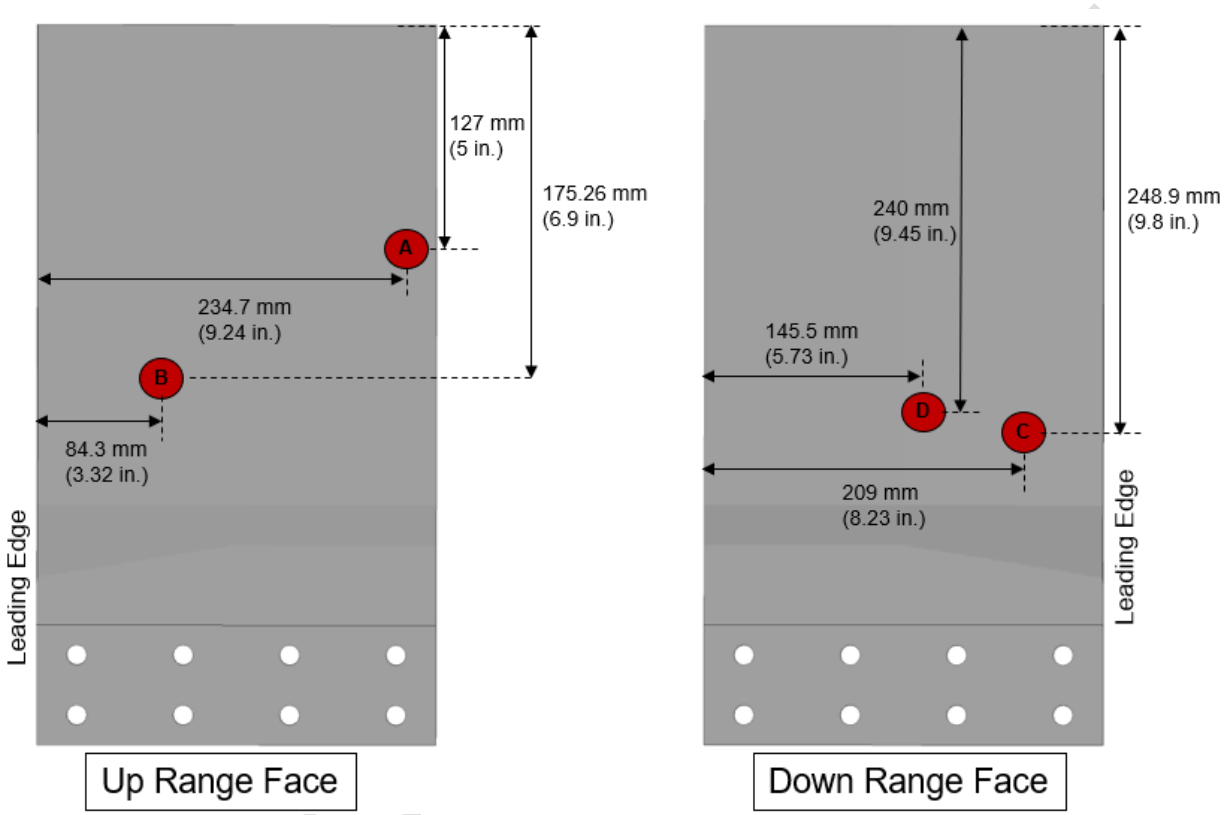

Figure 2.77. Location of points A,B,C, and D for extraction of DIC resultant displacement time history for test D80L7-002

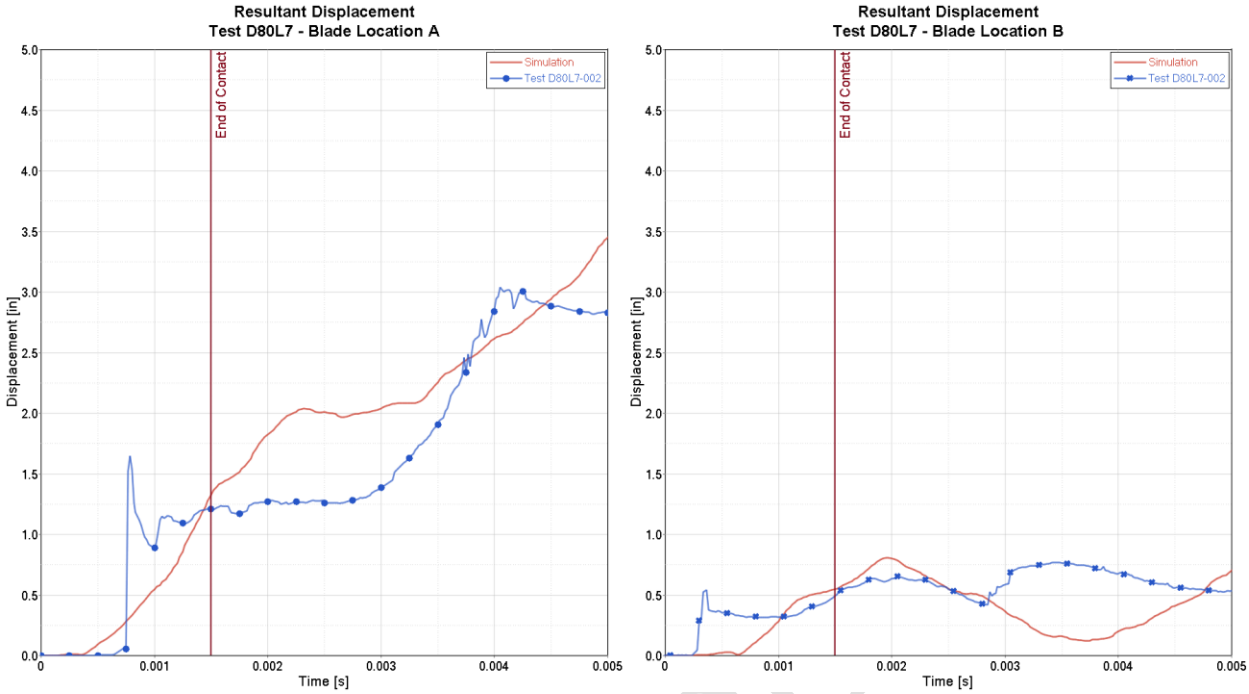

Figure 2.78. Resultant displacement of location A and B time history comparison between simulation and test D80L7-002

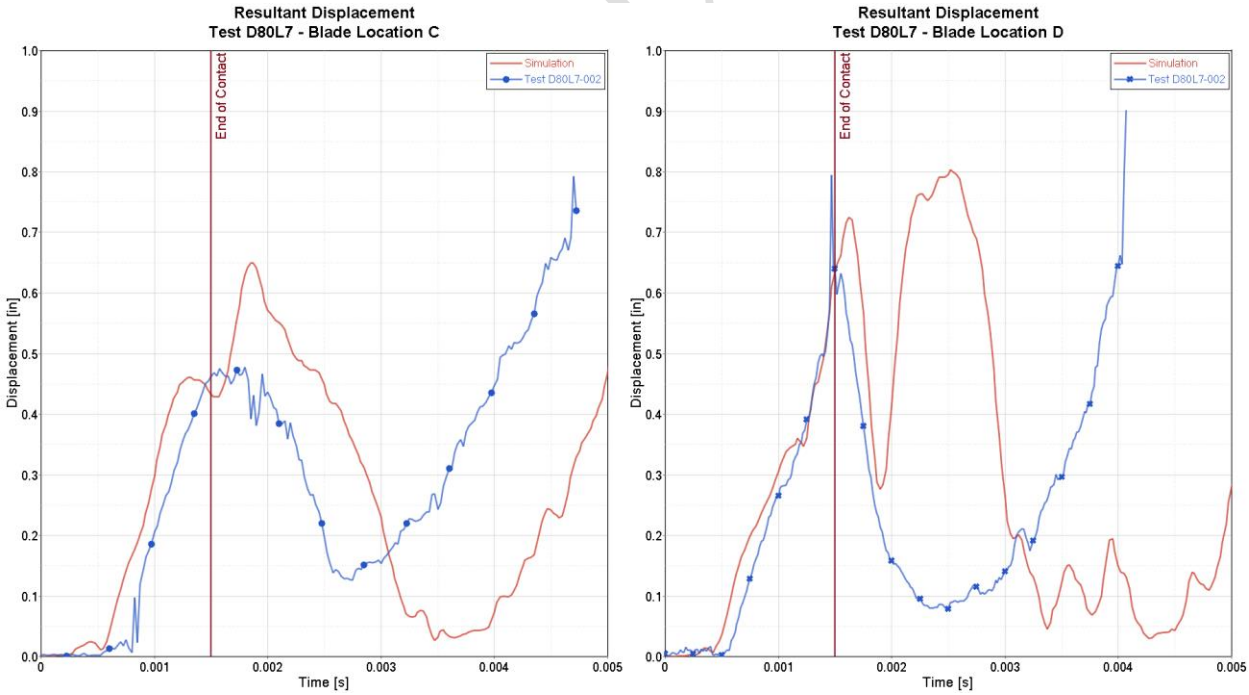

Figure 2.79. Resultant displacement of location C and D time history comparison between simulation and test D80L7-002

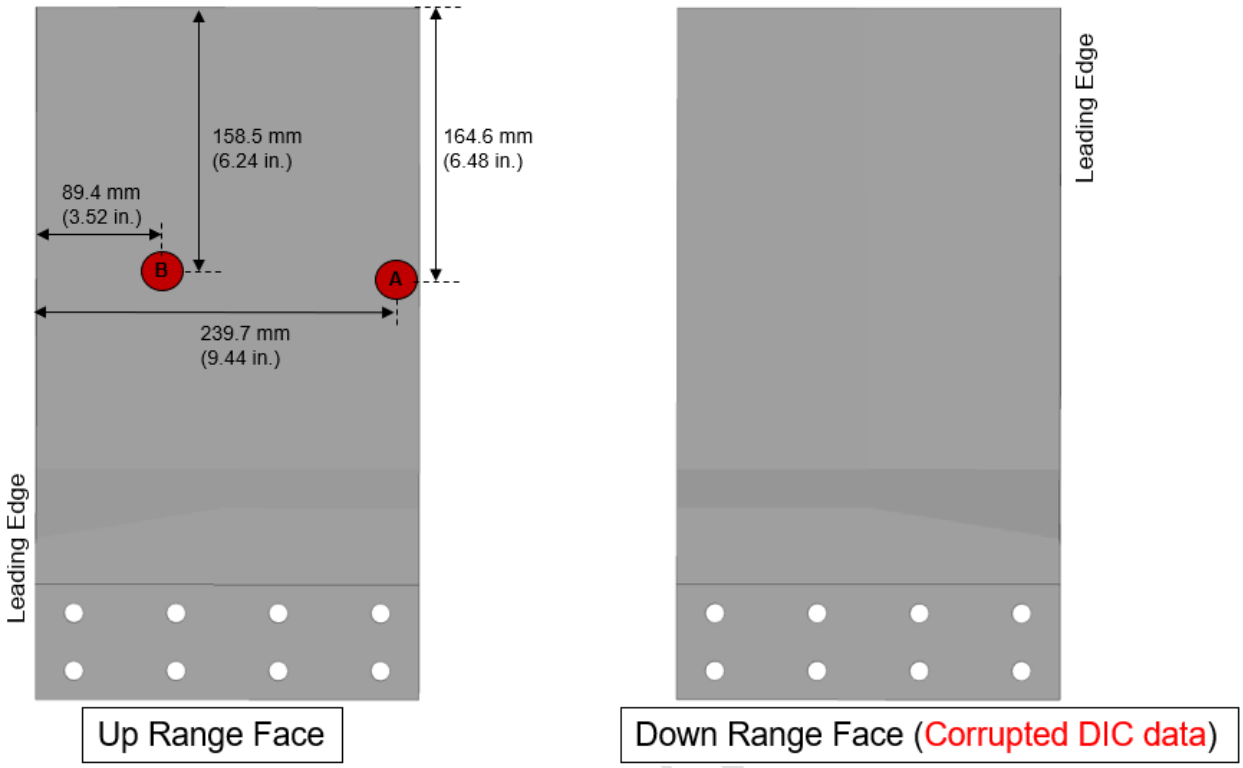

Figure 2.80. Location of points A and B for extraction of DIC resultant displacement time history for test D80L7-003

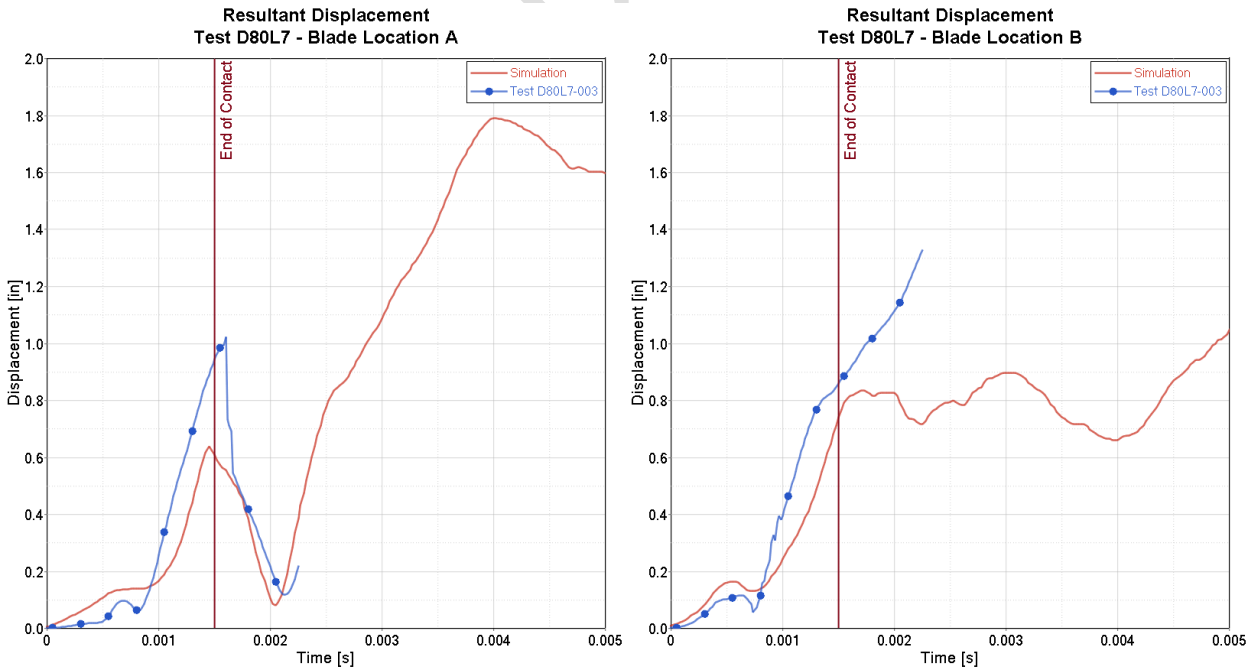

Figure 2.81. Resultant displacement of location A and B time history comparison between simulation and test D80L7-003

Due to the data acquisition system not being triggered, there was no load cell test data for test D80L7-001 shown in Figure 2.82. Figure 2.83 and Figure 2.84 show the load cells' data comparison between the simulation and the two remaining tests. The load cell 3 in test D80L7-002 experienced failure near the time of 0.004s resulting in the “noise” observed in Figure 2.83. The data has no filter, and its sampling rate was 1MHz for both the simulation and tests. The simulation results for the two remaining tests agree well with the test data. The strain gages' data comparison was not possible due to corrupted test data.

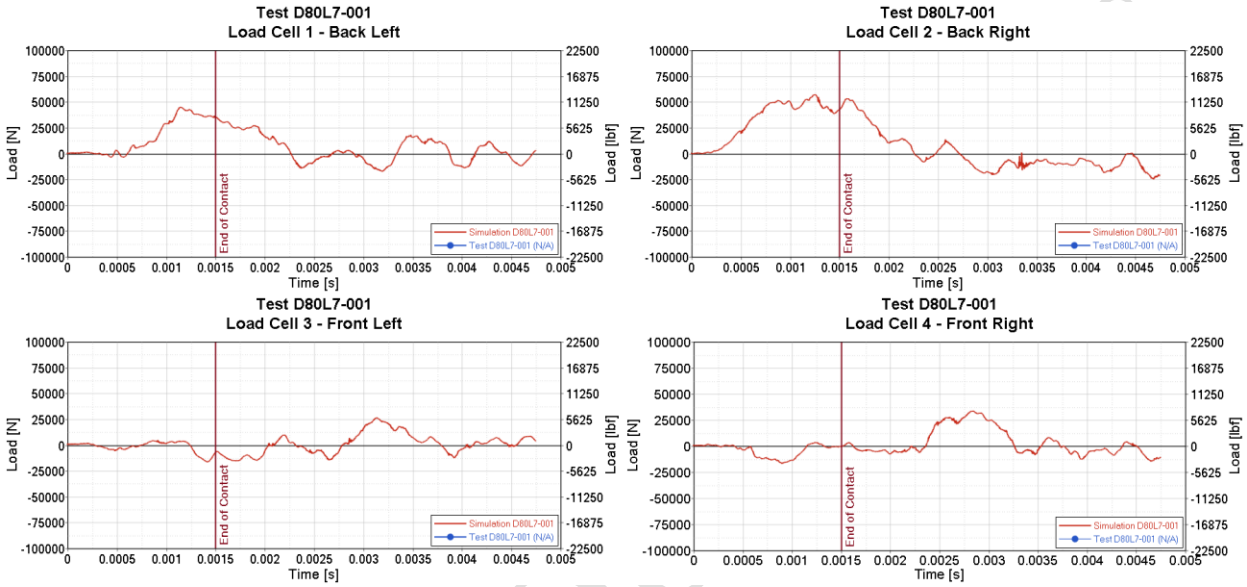

Figure 2.82. Test D80L7-001 load cells data comparison

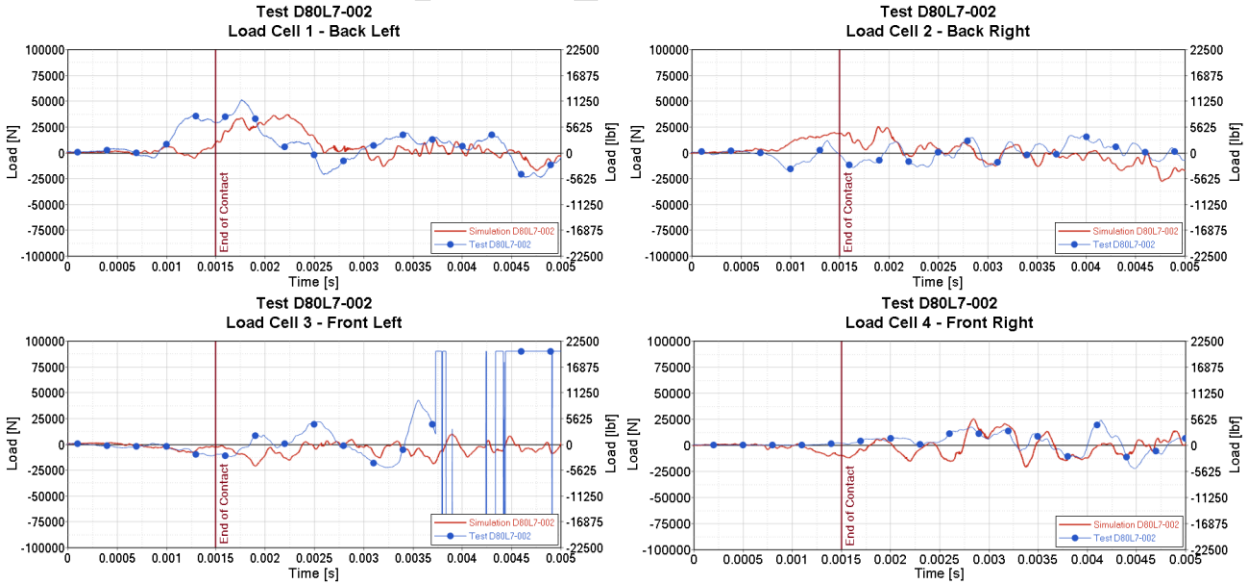

Figure 2.83. Test D80L7-002 load cells data comparison

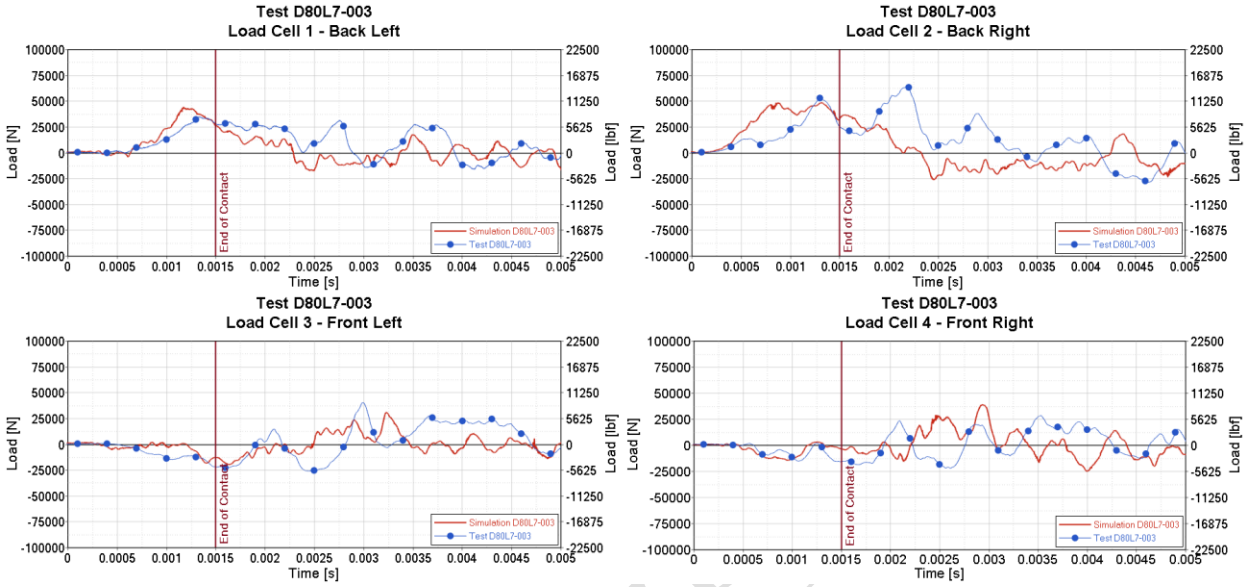

Figure 2.84. Test D80L7-003 load cells data comparison

The results in this section show a good qualitative correlation between simulation and physical test data in terms of blade damage, loads, and DIC points' time histories. Thus, for this D80L7 configuration, the sUAS body is considered validated.

2.2.1.2 D50L5 Test Configuration

For this test configuration, the sUAS body impacts the leading edge of the titanium blade Opt B-5 Rev 3 at the desired velocity of 218.64 m/s (425 knots). The impact location is at 50% radial span of the blade, and the blade is angled at 30 degrees relative to the impact direction. Three repetitions – D50L5-004, D50L5-005, and D50L5-006 – were conducted. Due to the high variability of the sUAS trajectory from launch for all the tests, they were all selected to corroborate with simulations. Figure shows the schematic setup of the D50L5 test configuration.

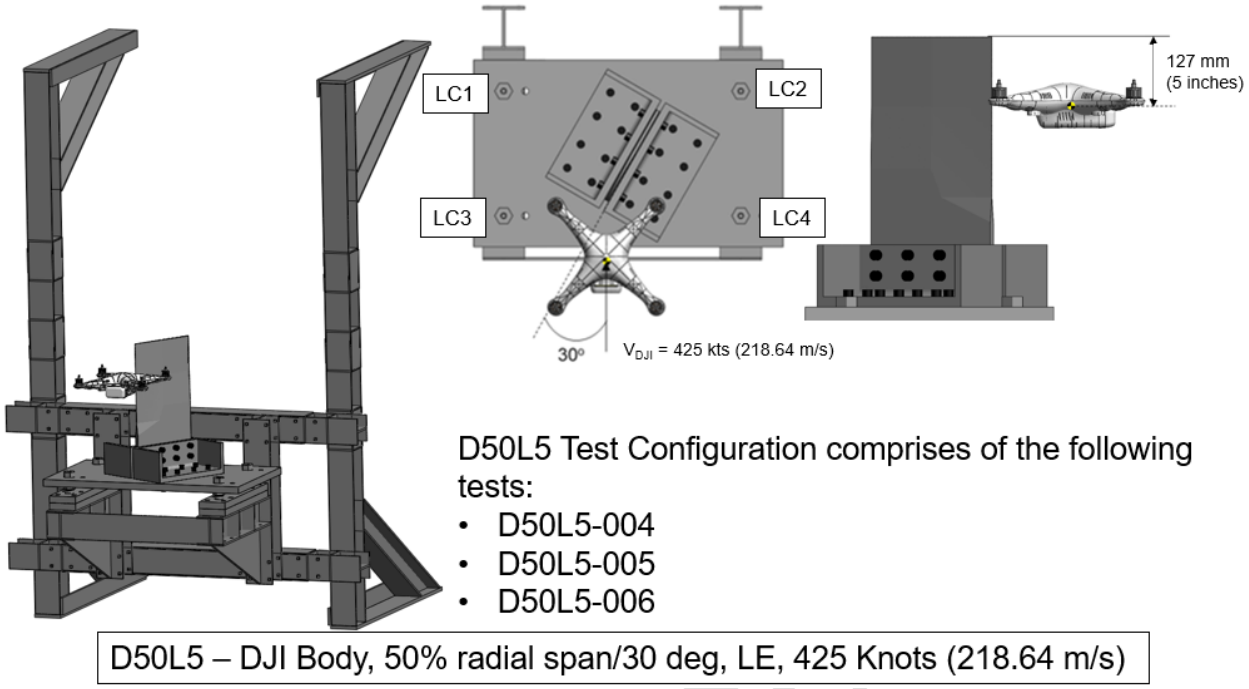

Figure 2.85. D50L5 test configuration setup

The simulations were set up to match the testing conditions for all the tests shown in Table 8.

Table 8. D50L5 test conditions

Test Case	Actual Impact Velocity	sUAS Pitch	sUAS Roll	sUAS Yaw	Impact Location w.r.t sUAS C.G.
D50L5-004	432 kts (222.75 m/s)	-20 deg	9 deg	25 deg	7.2 in. from the top of the blade
D50L5-005	419 kts (215.55 m/s)	-8 deg	-15 deg	3 deg	6.3 in. from the top of the blade
D50L5-006	428 kts (220.18 m/s)	-14 deg	-1.2 deg	0.3 deg	5.6 in. from the top of the blade

Figure 2.86 to Figure 2.88 and Figure 2.89 to Figure 2.91 show the top and side view kinematics comparison between the D50L5 tests and simulations from the start to the end of the impact. Three instances were compared. The first instance at t=0s is the start of the simulation before the impact. The second instance at t=0.001s is during the impact. The last instance at t=0.002s is after the impact.

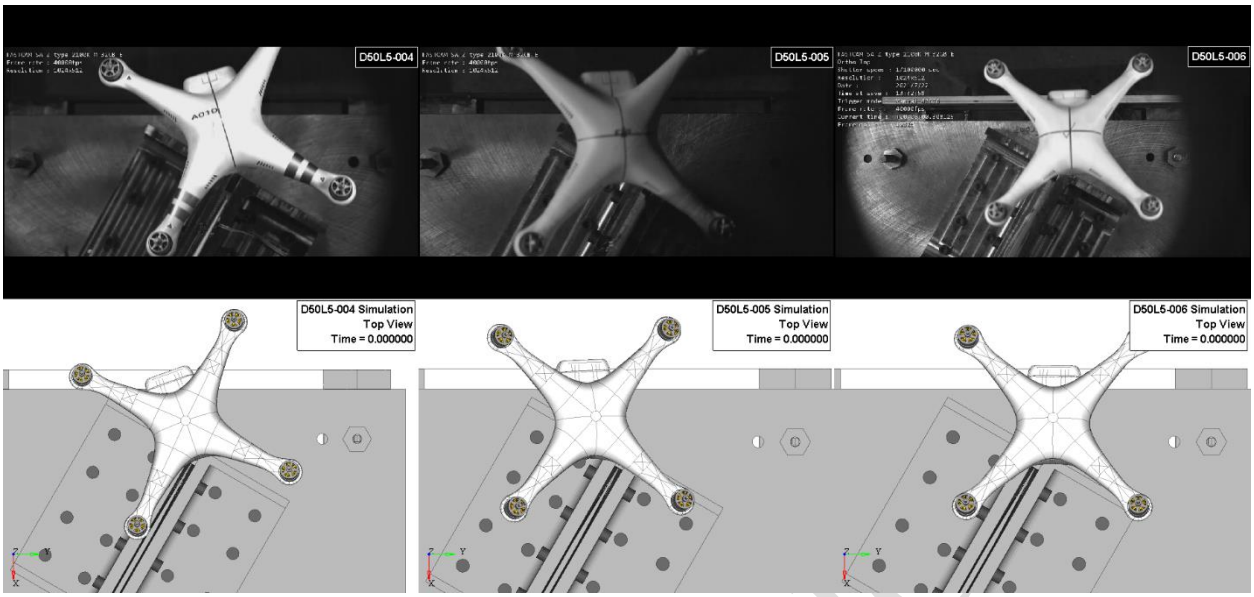

Figure 2.86. D50L5 tests top view kinematics comparison at t=0s

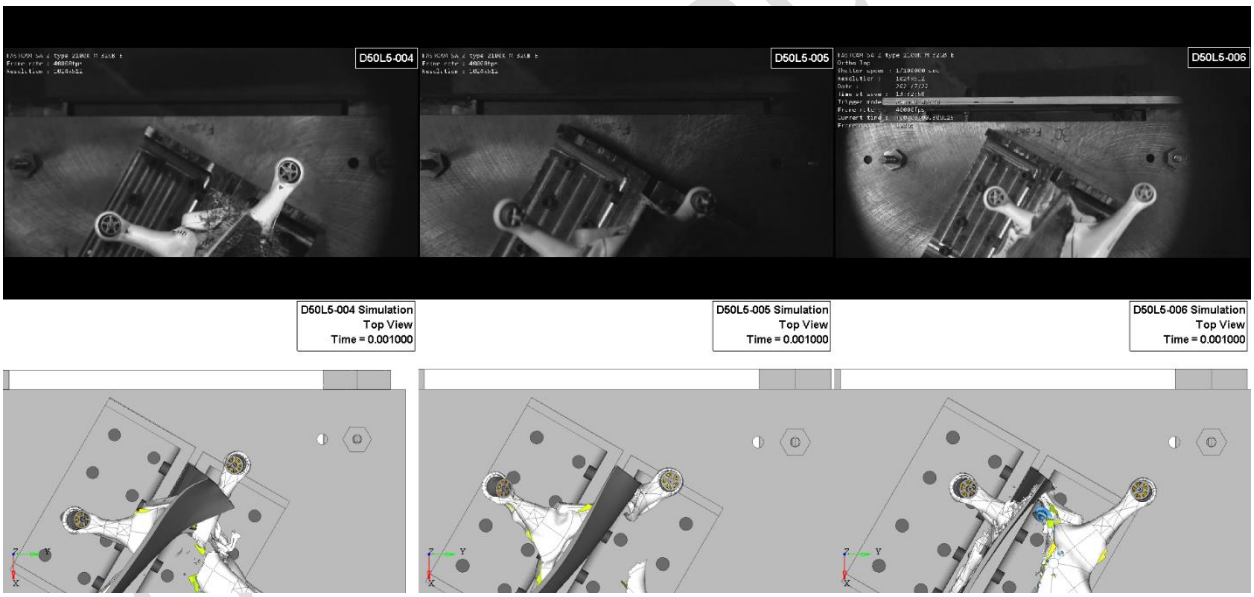

Figure 2.87. D50L5 tests top view kinematics comparison at t=0.001s

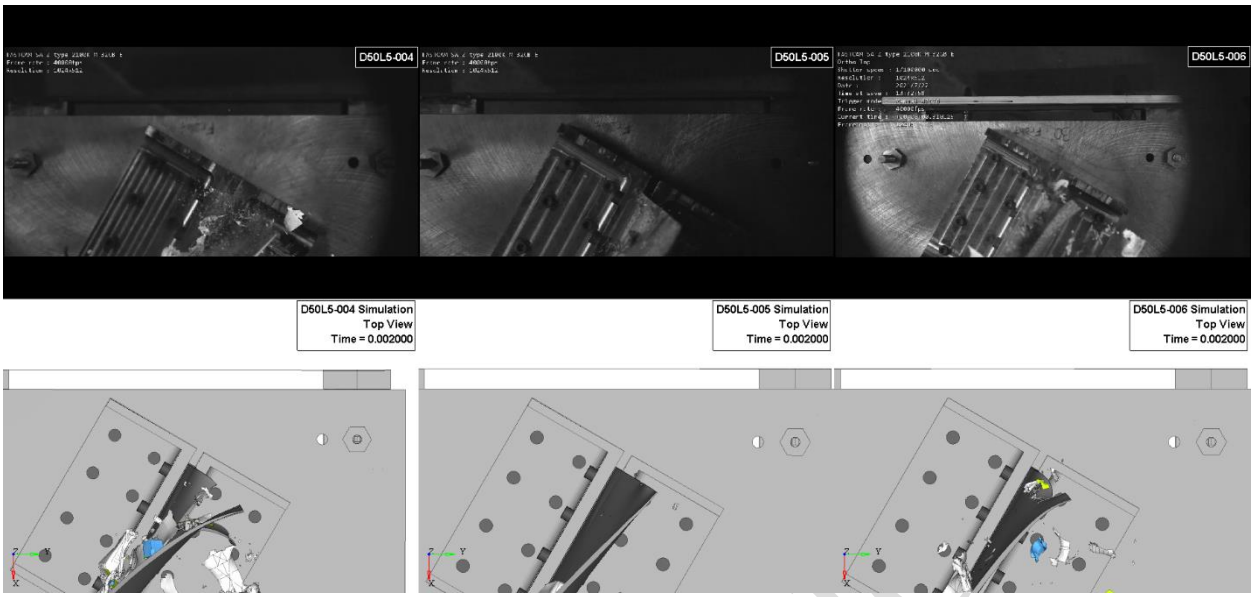

Figure 2.88. D50L5 tests top view kinematics comparison at t=0.002s

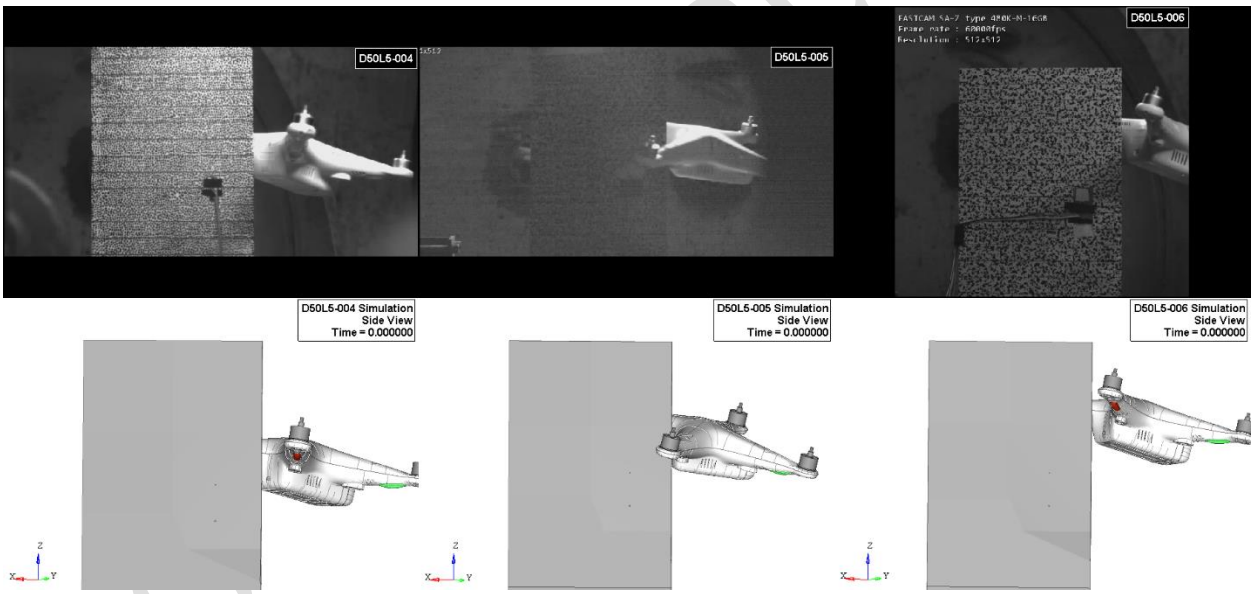

Figure 2.89. D50L5 tests side view kinematics comparison at t=0s

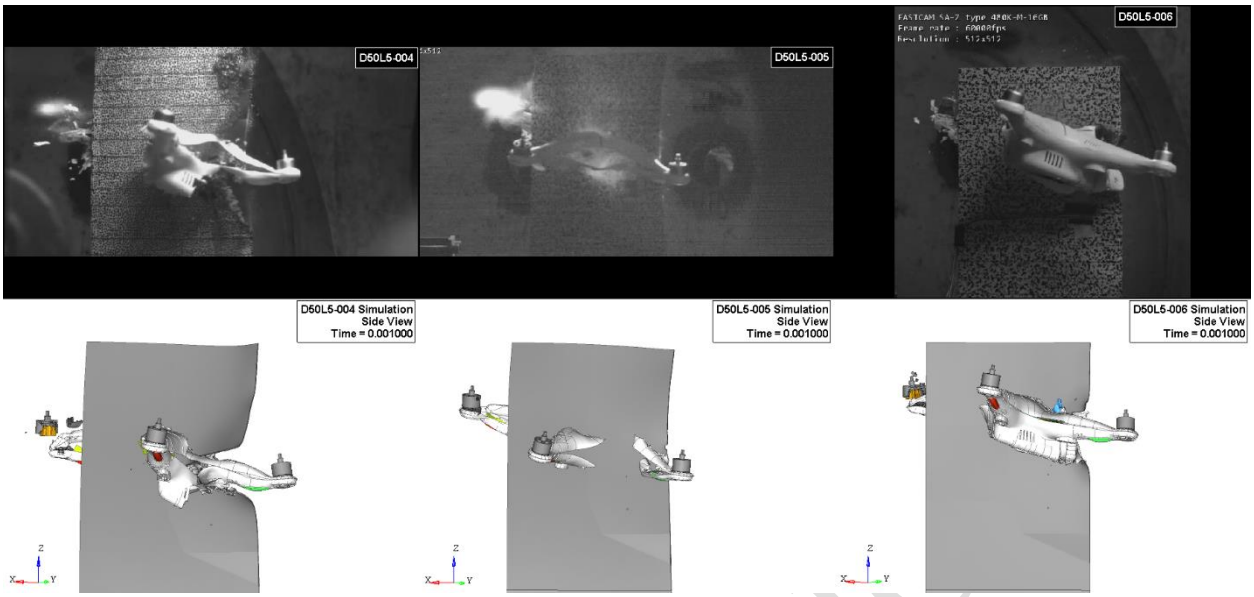

Figure 2.90. D50L5 tests side view kinematics comparison at t=0.001s

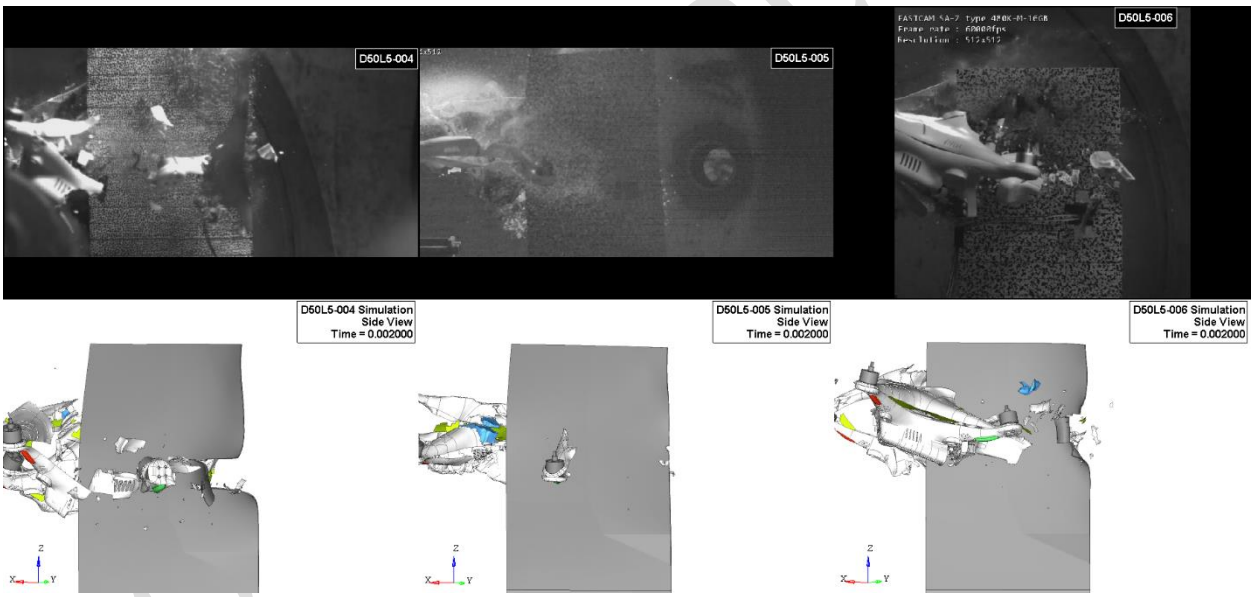

Figure 2.91. D50L5 tests side view kinematics comparison at t=0.002s

After 2ms, shown in all the simulations, the blade continued vibrating due to the impact's residual energy. Thus, an additional spring back analysis was performed on the blade to obtain its final deformed shape at its equilibrium state. Figure 2.92 compares the final blade damage between the spring back analysis prediction and the physical test damage for all the tests. The FE results show tears on the blade's LE for tests D50L5-004 and D50L5-006 that are not observed in the actual tests because of the FE modeling and blade material limitations. Instead of the tears, the physical blades showed significant plastic deformation/big dents in the same areas. Although more

conservative, the FE result for the blade's LE shows a reasonably good correlation with the final deformed shape of the physical blade's LE.

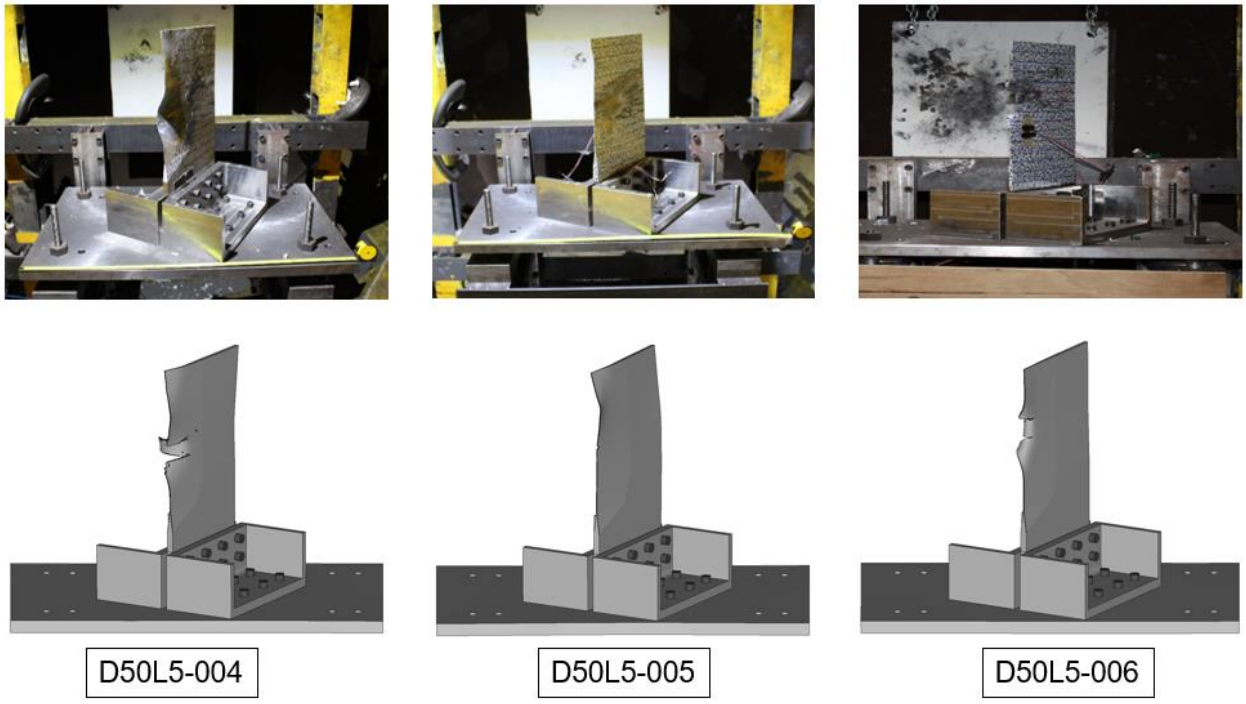

Figure 2.92. Spring back analysis prediction of blade damage vs. physical test damage for all D50L5 tests

Similar difficulty observed in the components' level tests in processing DIC data was present for the full-scale tests. In fact, the sUAS body being larger than its components, produced much more debris that covered most of the blade surface during the impact obstructing the DIC camera views. As a result, it was not possible to obtain good DIC contour data to compare with the simulations. Nevertheless, the time history of the resultant displacement from specific points on the blade surfaces was obtained and used to compare the simulations and three D50L5 tests where possible. Due to debris obstruction, the complete test time history curves were unavailable for the entire impact duration. Figure 2.93 to Figure 2.100 show these points' locations and the displacement comparison results. Overall, the simulation displacement agrees with the D50L5 tests.

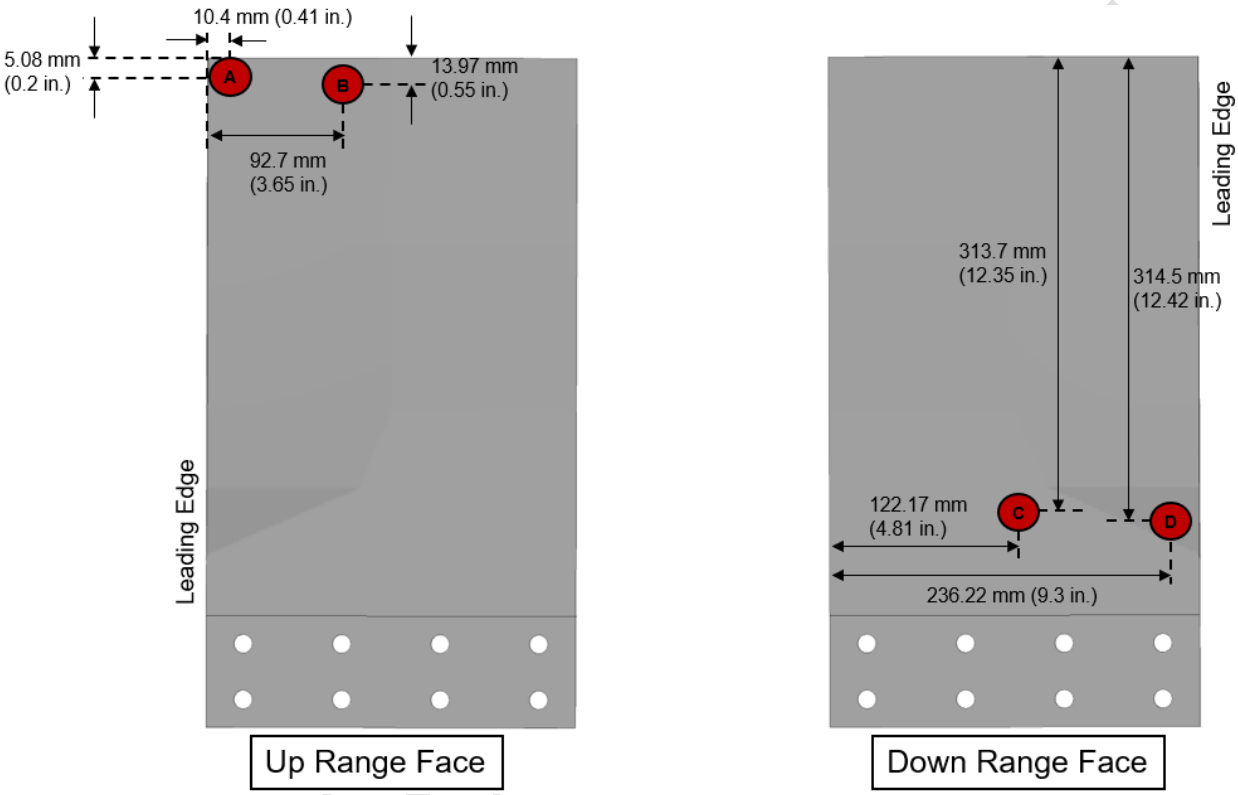

Figure 2.93. Location of points A,B,C, and D for extraction of DIC resultant displacement time history for test D50L5-004

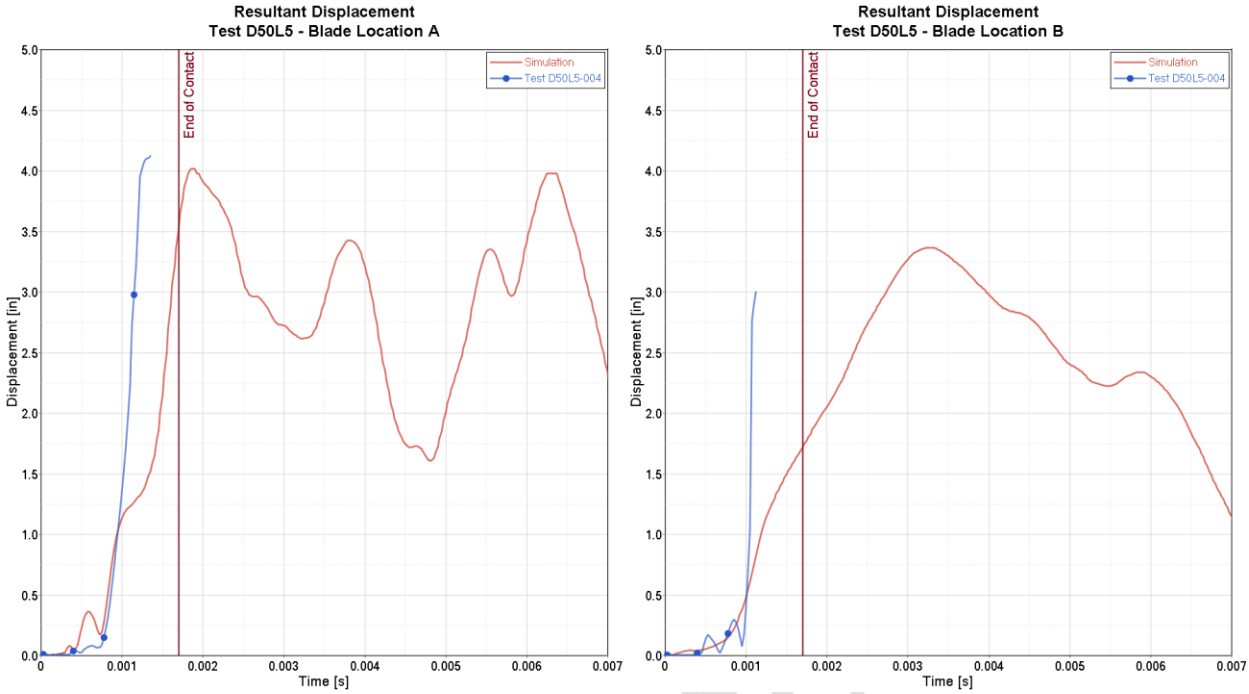

Figure 2.94. Resultant displacement of location A and B time history comparison between simulation and test D50L5-004

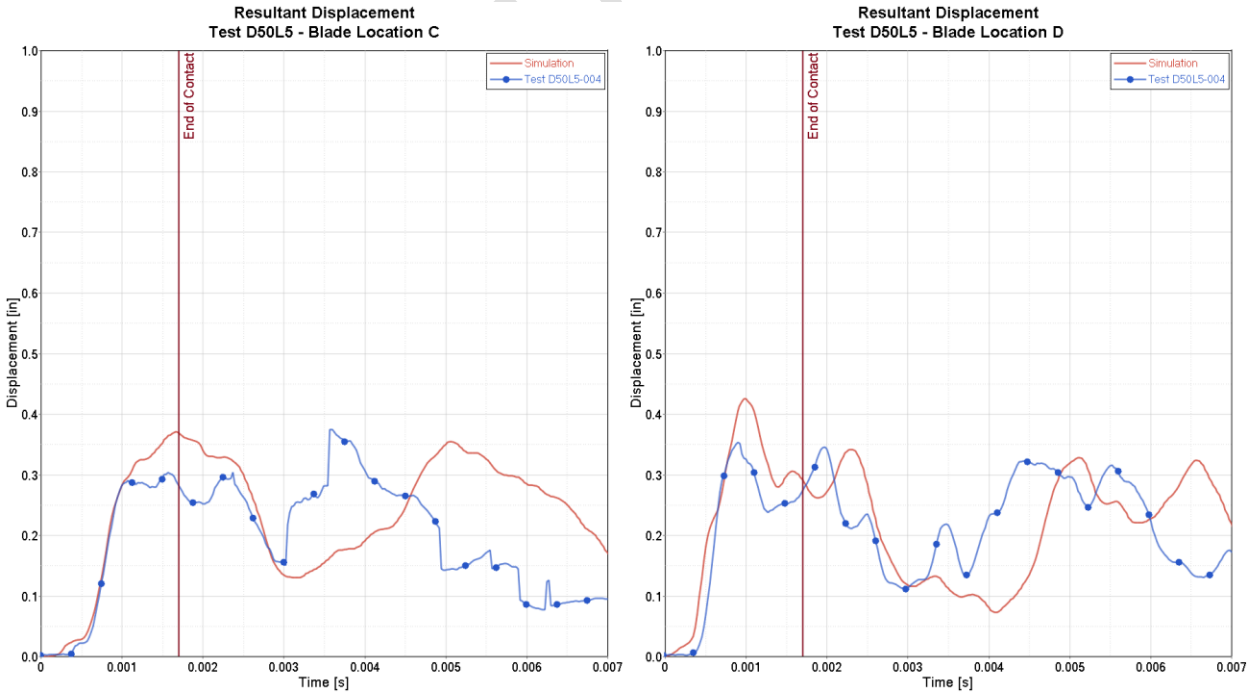

Figure 2.95. Resultant displacement of location C and D time history comparison between simulation and test D50L5-004

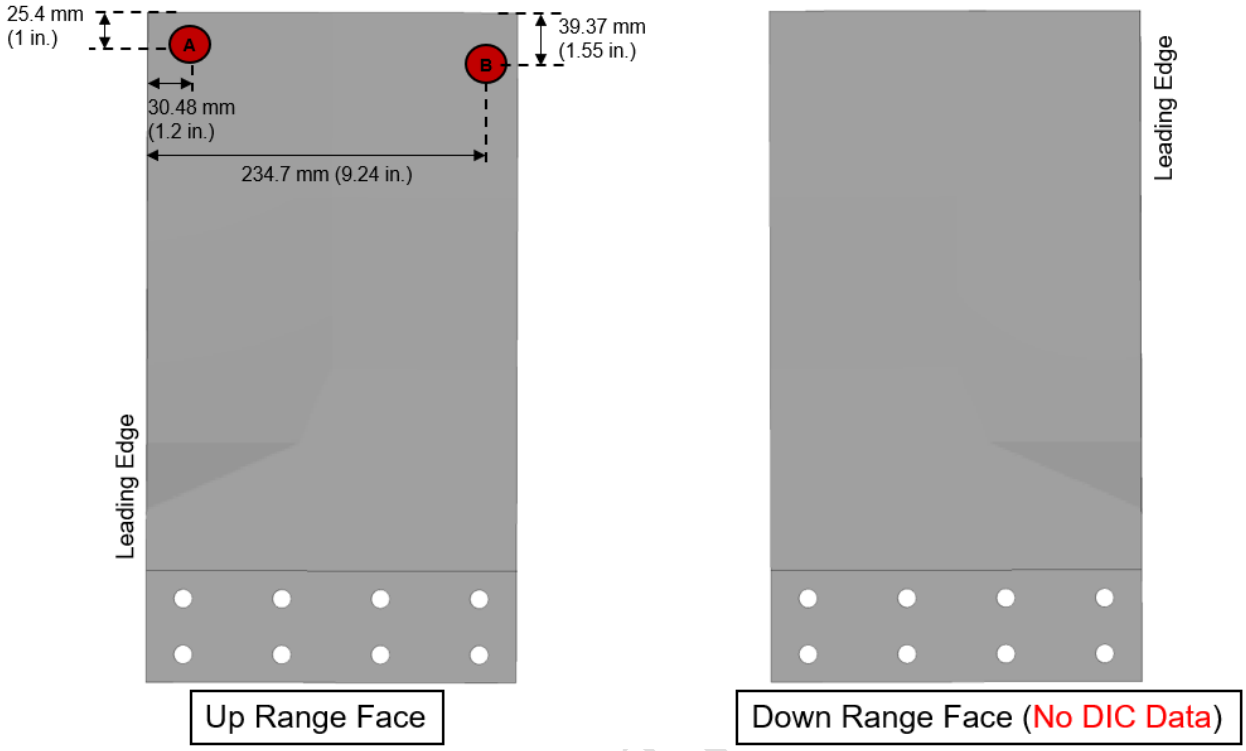

Figure 2.96. Location of points A and B for extraction of DIC resultant displacement time history for test D50L5-005

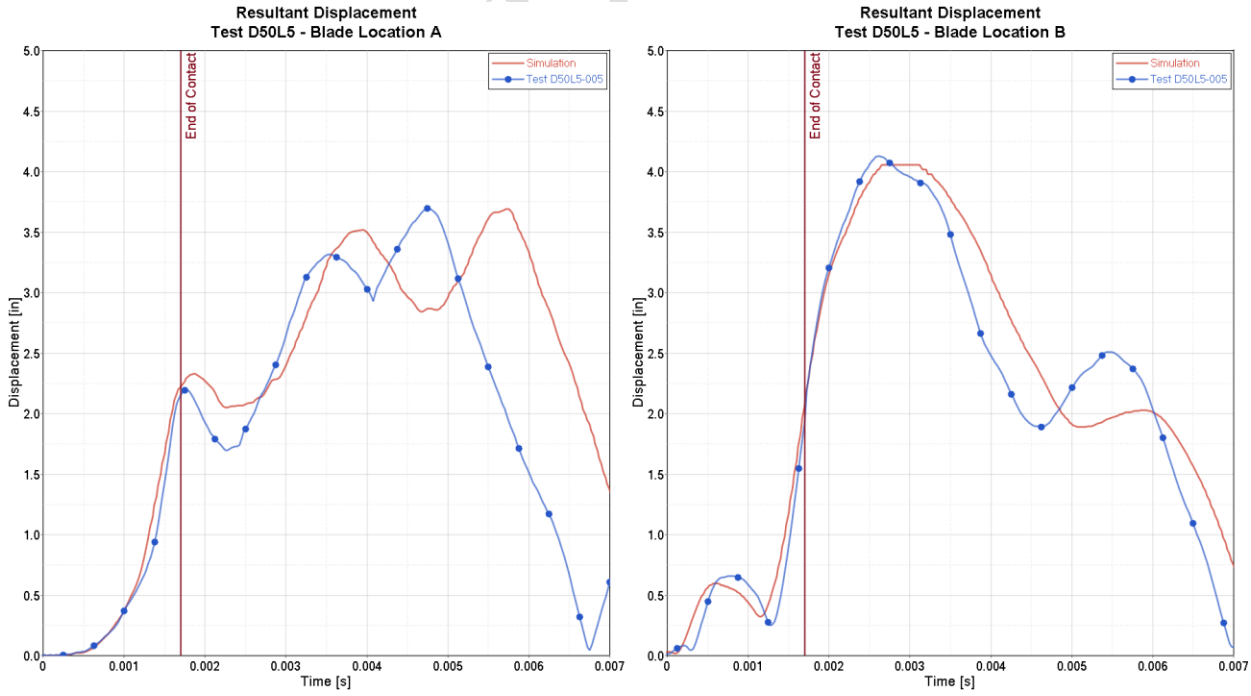

Figure 2.97. Resultant displacement of location A and B time history comparison between simulation and test D50L5-005

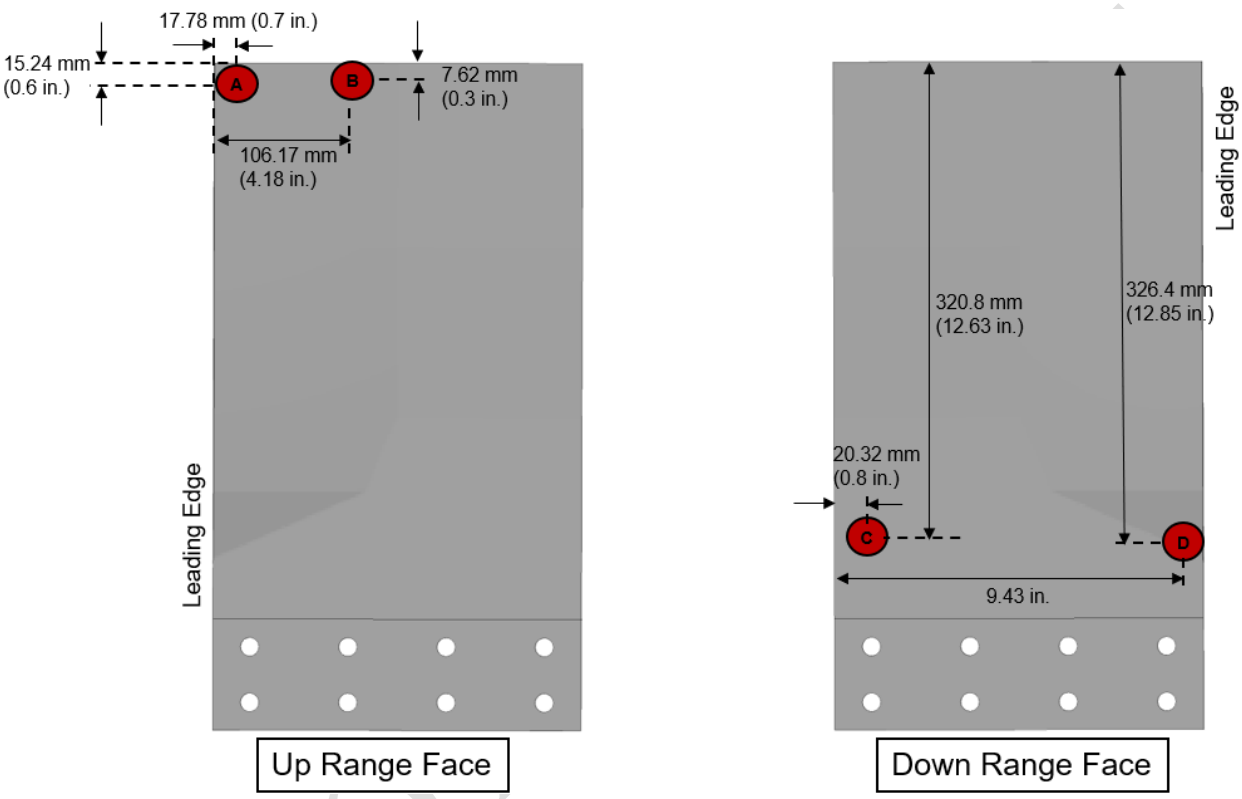

Figure 2.98. Location of points A,B,C, and D for extraction of DIC resultant displacement time history for test D50L5-006

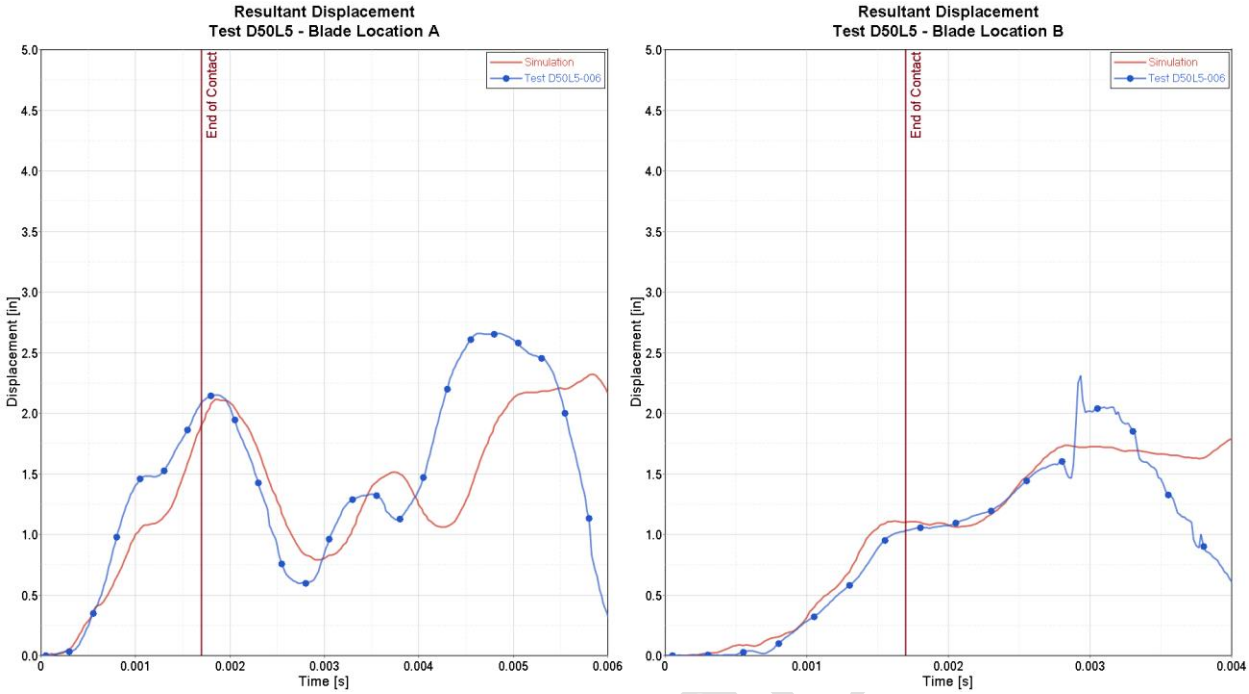

Figure 2.99. Resultant displacement of location A and B time history comparison between simulation and test D50L5-006

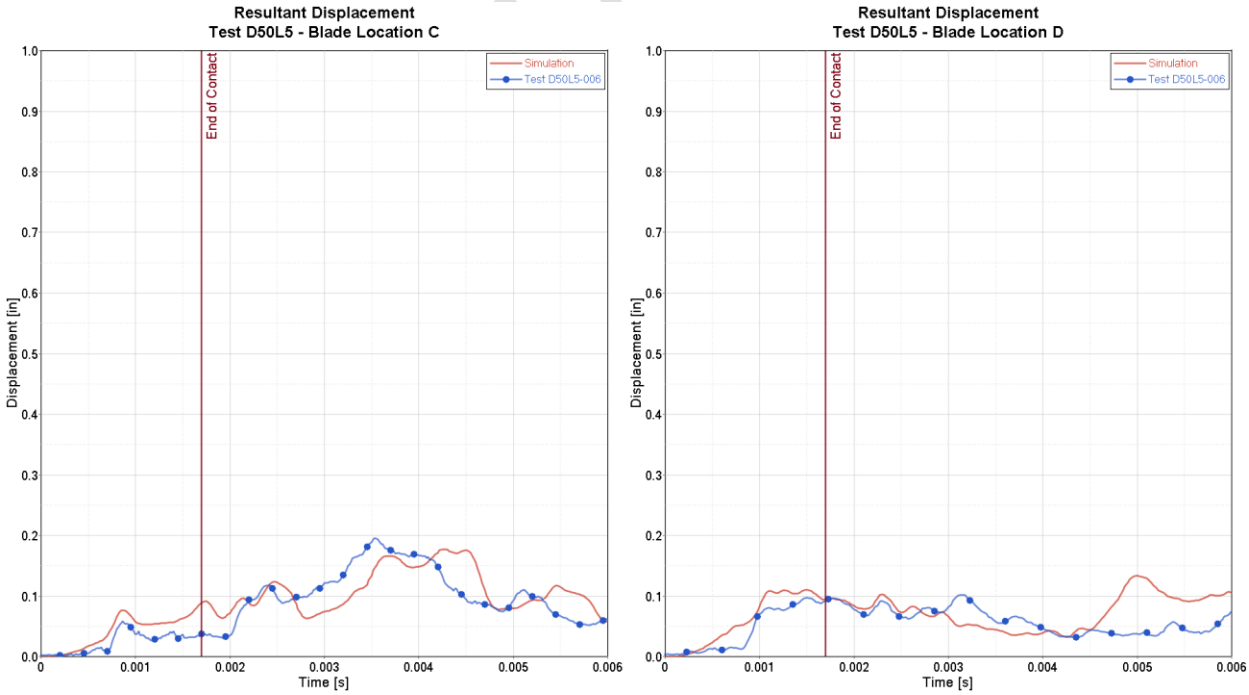

Figure 2.100. Resultant displacement of location C and D time history comparison between simulation and test D50L5-006

Figure 2.101 to Figure 2.103 show the load cells' data comparison between the simulation and three D50L5 tests. The data has no filter, and its sampling rate was 1MHz for both the simulation and tests. The simulation results agree with the test data. The strain gages' data comparison was not possible due to inadequate test data.

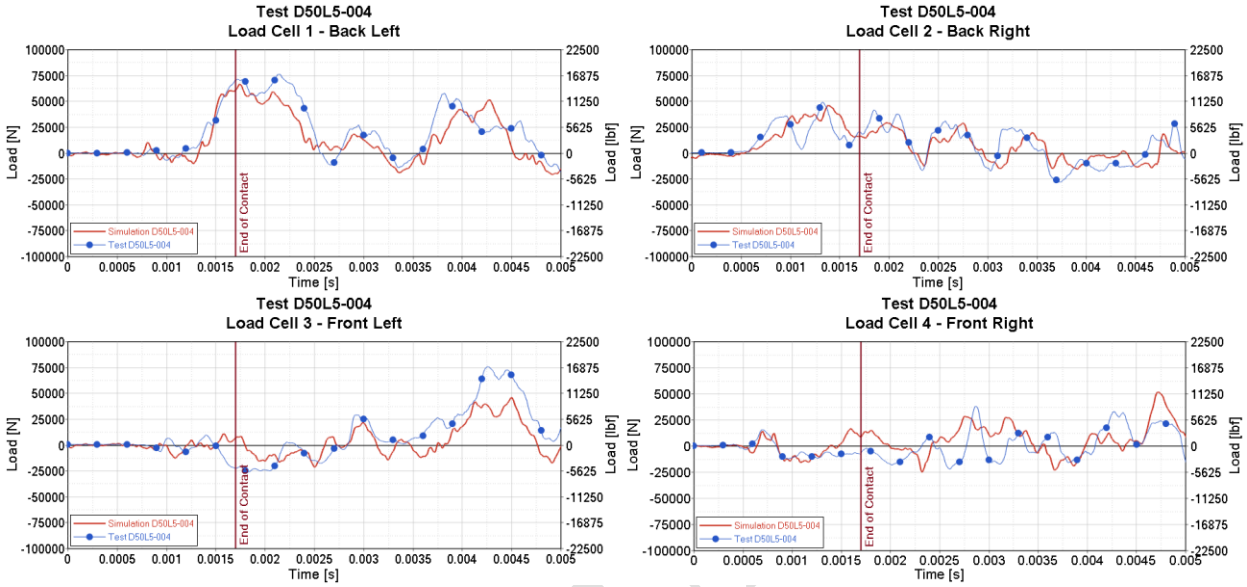

Figure 2.101. Test D50L5-004 load cells data comparison

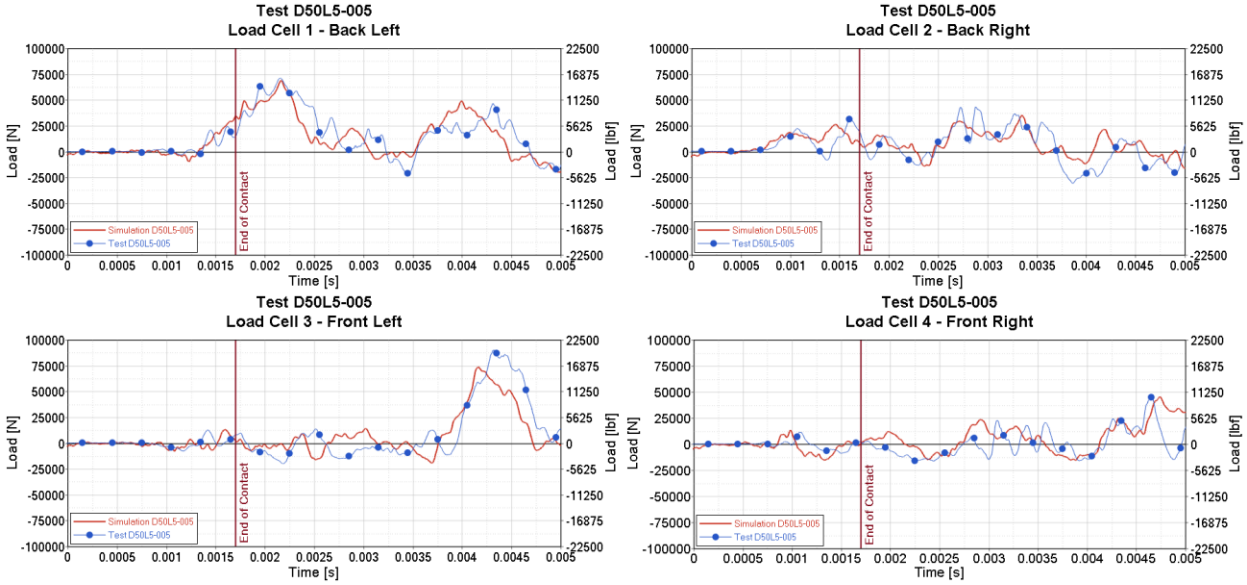

Figure 2.102. Test D50L5-005 load cells data comparison

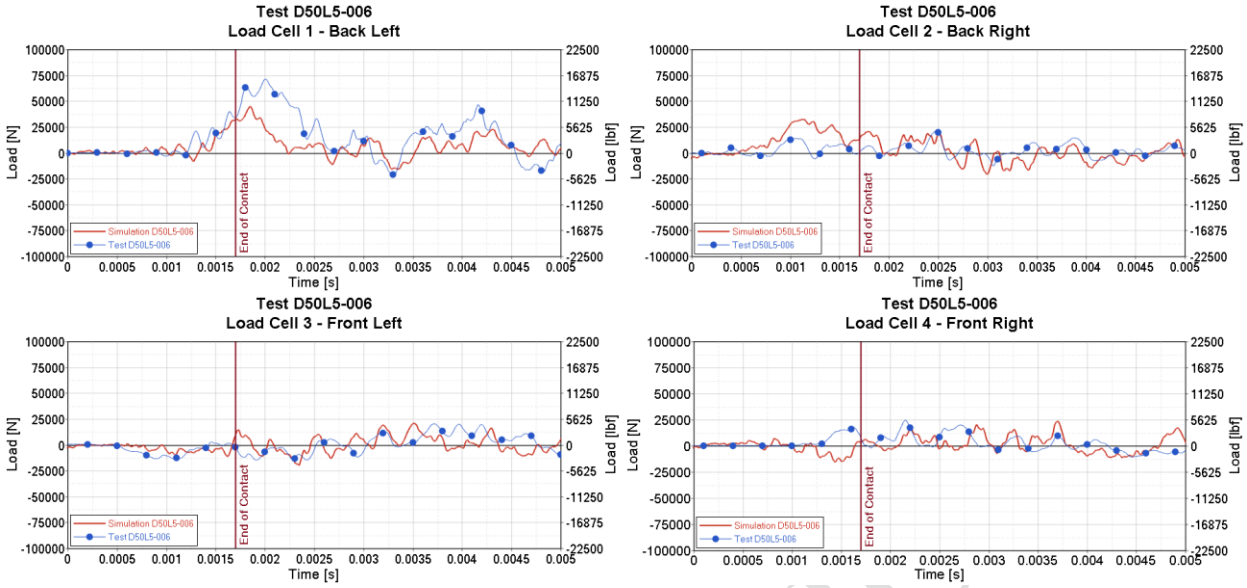

Figure 2.103. Test D50L5-006 load cells data comparison

The results in this section show a good qualitative correlation between simulation and physical test data in terms of blade damage, loads, and DIC points' time histories. Thus, for this D50L5 configuration, the sUAS body is considered validated.

2.2.1.3 FE Information of the Validated UAS

Through the validation works documented in section 2.1 and 2.2 the full UAS FE model leveraged from A3 [1] was updated with the validated key components (motor, battery, and camera) and considered validated under the current study conditions. Figure 2.104 shows the UAS geometry and the location of the updated components. Besides the updates of these components, the rest of FE model definition remains the same as the one in A3 program [1].

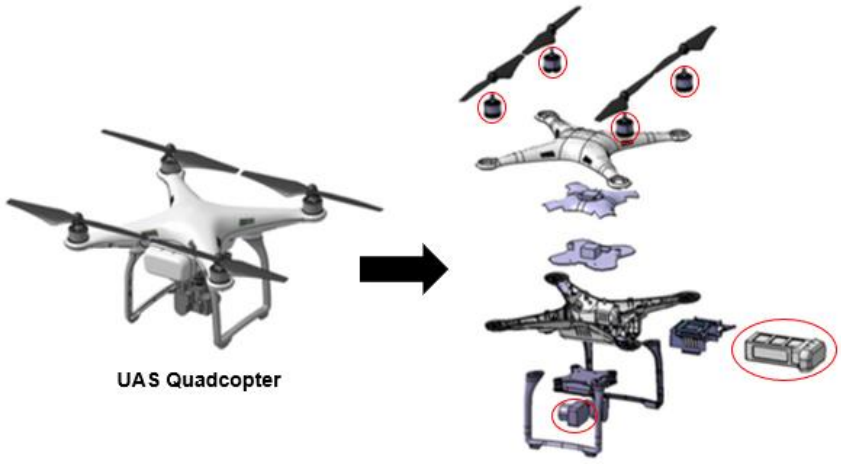

Figure 2.104. Geometry of UAS quadcopter and validated components (highlighted in red)

3. CONCLUSIONS

Leveraging the FAA ASSURE A3 Airborne Collision Studies [1], NIAR updated the full sUAS and its critical components FE models (motors, battery, and camera) to match the engine ingestion conditions under the current research study. The update of these FE models is validated by comparing the numerical analysis and the physical tests conducted at UAH. In particular, there were 17 tests for the sUAS components and 6 tests for the full-scale sUAS. The validation between the simulations and physical tests considers the following data set:

- The kinematics
- The assessment of fan blade damage
- Load cells' data
- Strains data from the DIC

Each FE model went through the above data set to be validated in a meaningful and qualitative manner. Good correlations for these data were observed in all the test comparisons from the components to the full-scale level. Thus, the sUAS and its components are successfully validated under A17 impact conditions and are ready to be integrated with the complete engine model for further research of different engine ingestion scenarios.

4. REFERENCES

1. Olivares, G., Gomez, L., Espinosa de los Monteros, J., Baldridge, R.J., Zinzuwadia, C., and Aldag, T., "Volume II–UAS Airborne Collision Severity Evaluation–Quadcopter.", 2017.
2. Olivares, G., Lacy, T., Gomez, L., Espinosa de los Monteros, J., Baldridge, R.J., Zinzuwadia, C., Aldag, T., Raj Kota, K., Ricks, T., and Jayakody, N., "Volume III–UAS Airborne Collision Severity Evaluation–Fixed-Wing.", 2017.

APPENDIX A— COMPONENT LEVEL MESH SENSITIVITY STUDY

This appendix shows the results of the blade mesh sensitivity study for the component level tests. The study analyzed the final blade damage and the load cell correlations for all of the six (6) tests in section 2.1 where each test represented a different configuration shown in Table 1.

A.1. TEST M80L7-002

Figure A.1 shows the mesh sensitivity study for test M80L7-002 with three different mesh density setups. The original mesh blade has six (6) elements through thickness suggested initially by OSU, whereas the coarse mesh blade has three (3) elements through thickness. The motor has the original mesh carried over from the A3 program and its refined mesh used for this study.

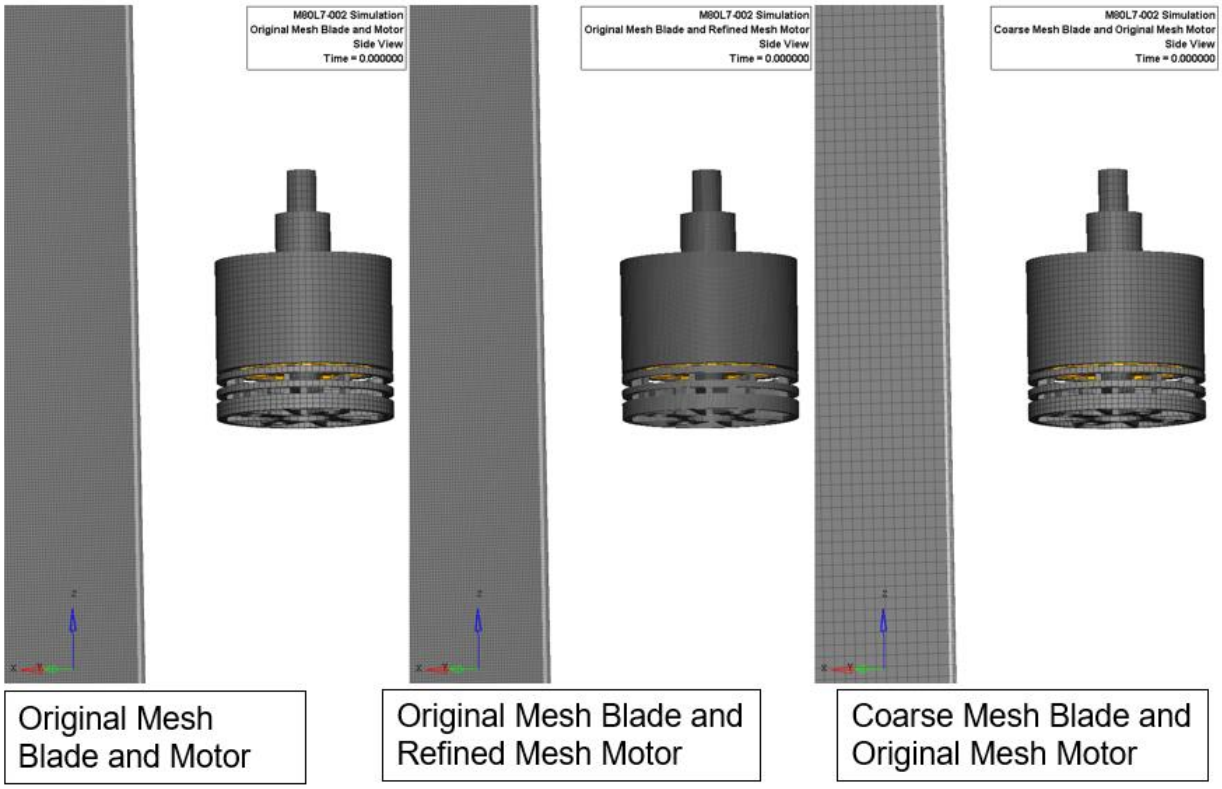

Figure A.1. Test M80L7-002 mesh sensitivity study – FE model setups

Figure A.2 compares the final blade damage between the three FE setups and the physical blade. All three setups were able to capture the visible tear observed on the physical blade's LE.

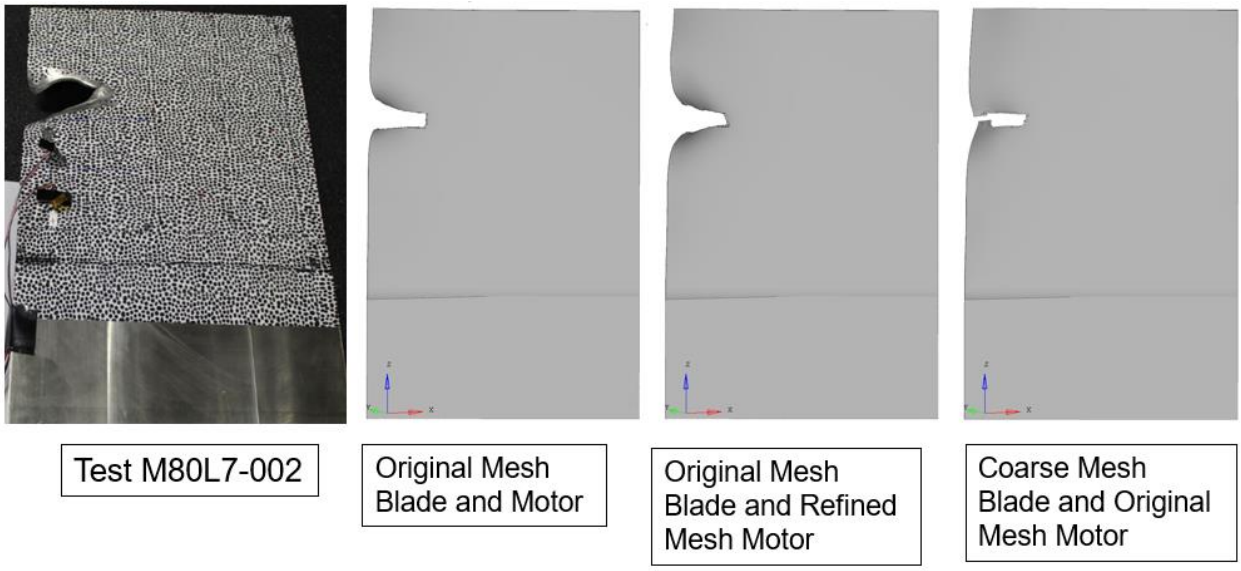

Figure A.2. Test M80L7-002 mesh sensitivity study – Final blade damage

Figure A.3 shows the load cell correlations between the three FE setups and the experimental test results. All three setups agree well with the experimental data. With the results from this sensitivity study, it is concluded that the coarse mesh blade with three (3) elements through thickness and the original mesh motor is the optimal setup because of the most efficient computational time and good final blade damage correlation.

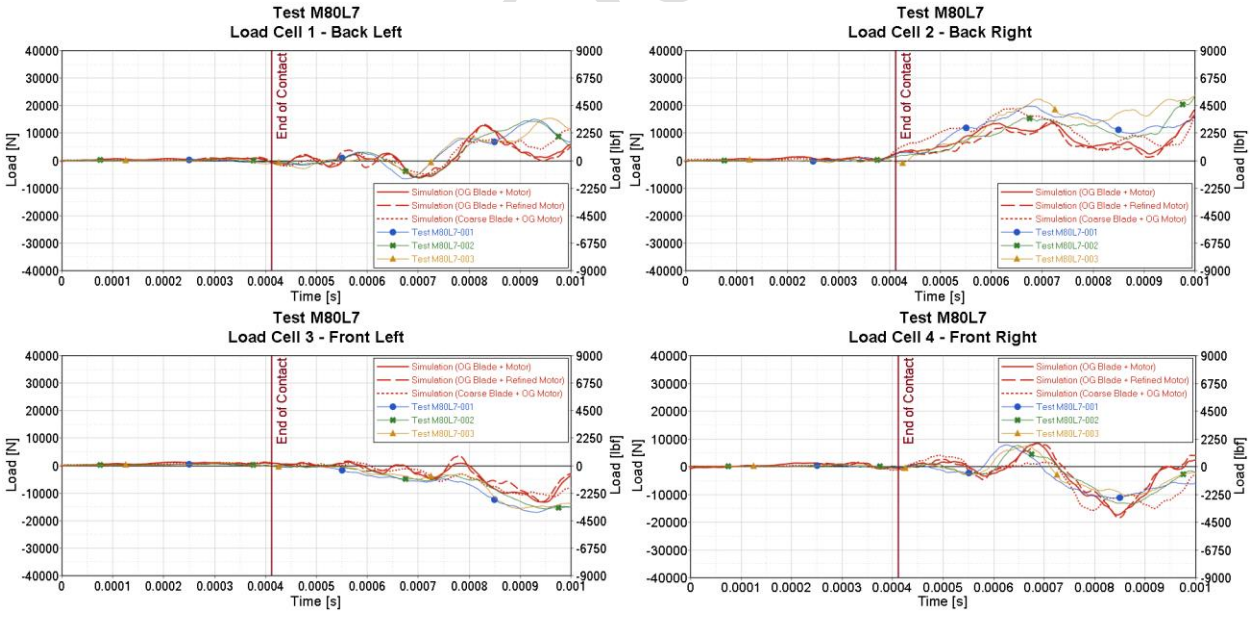

Figure A.3. Test M80L7-002 mesh sensitivity – Load cell correlations

A.2. TEST M50L5-004

Figure A.4 shows the mesh sensitivity study for test M50L5-004 with three different mesh density setups. The original mesh blade has six (6) elements through thickness suggested initially by OSU, whereas the coarse mesh blade has three (3) elements through thickness. The motor has the original mesh carried over from the A3 program and its refined mesh used for this study.

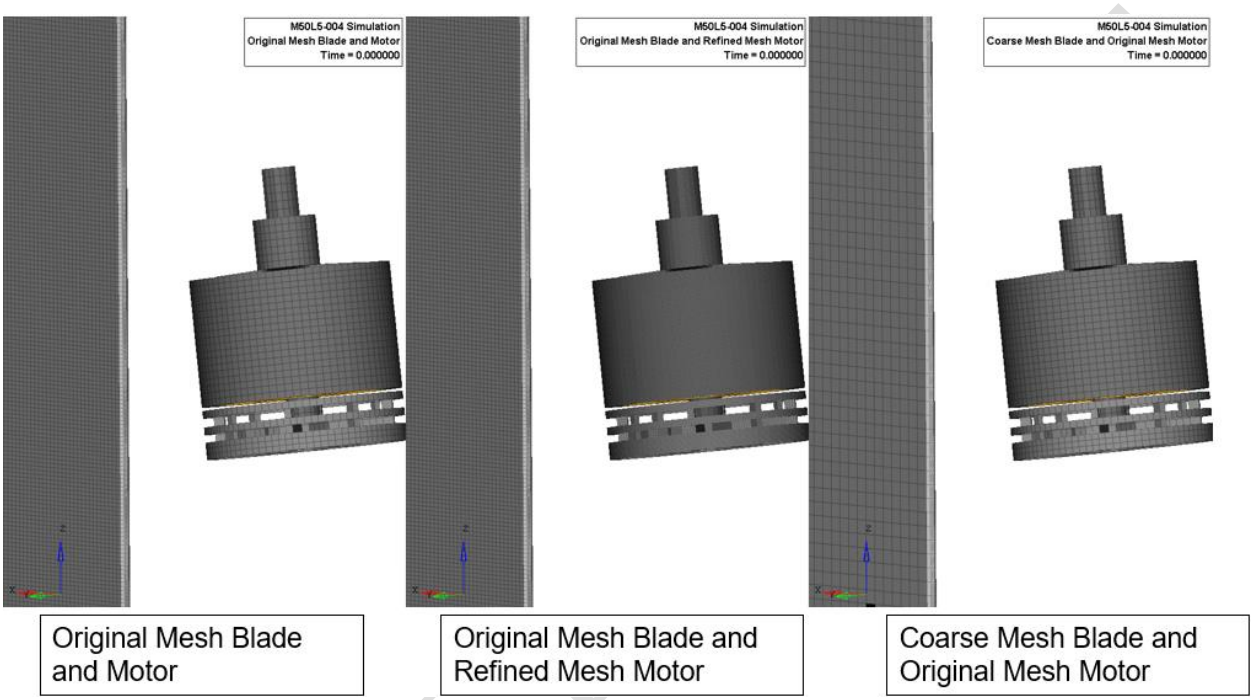

Figure A.4. Test M50L5-004 mesh sensitivity study – FE model setups

Figure A.5 compares the final blade damage between the three FE setups and the physical blade. None of the three setups were able to capture the visible dent observed on the physical blade's LE. Nevertheless, the coarse mesh blade and the original mesh motor setup best compare the line crack instead of the larger tears seen in the other two setups.

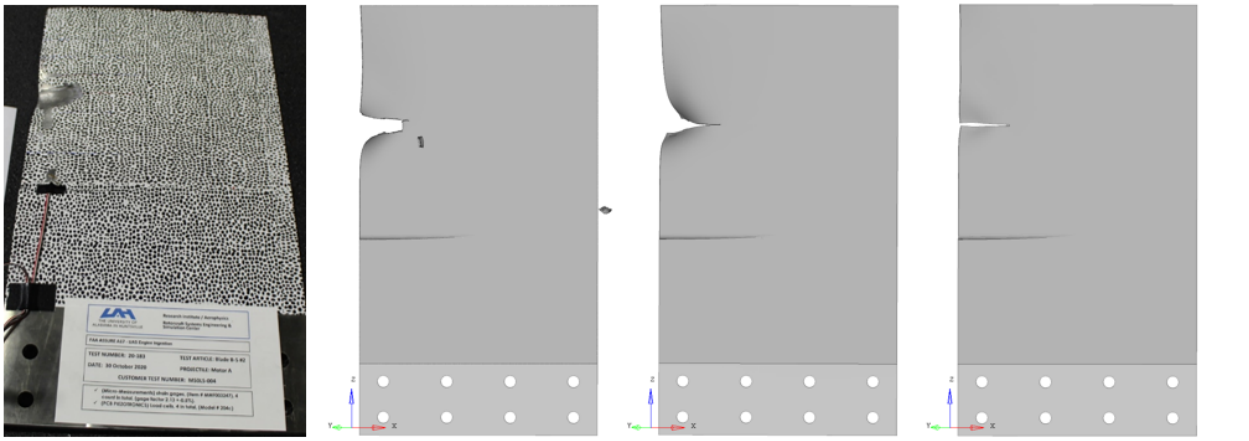

Figure A.5. Test M50L5-004 mesh sensitivity study – Final blade damage

Figure A.6 shows the load cell correlations between the three FE setups and the experimental test results. All three setups agree well with the experimental data. With the results from this sensitivity study, it is concluded that the coarse mesh blade with three (3) elements through thickness and the original mesh motor is the optimal setup because of the most efficient computational time and best final blade damage correlation.

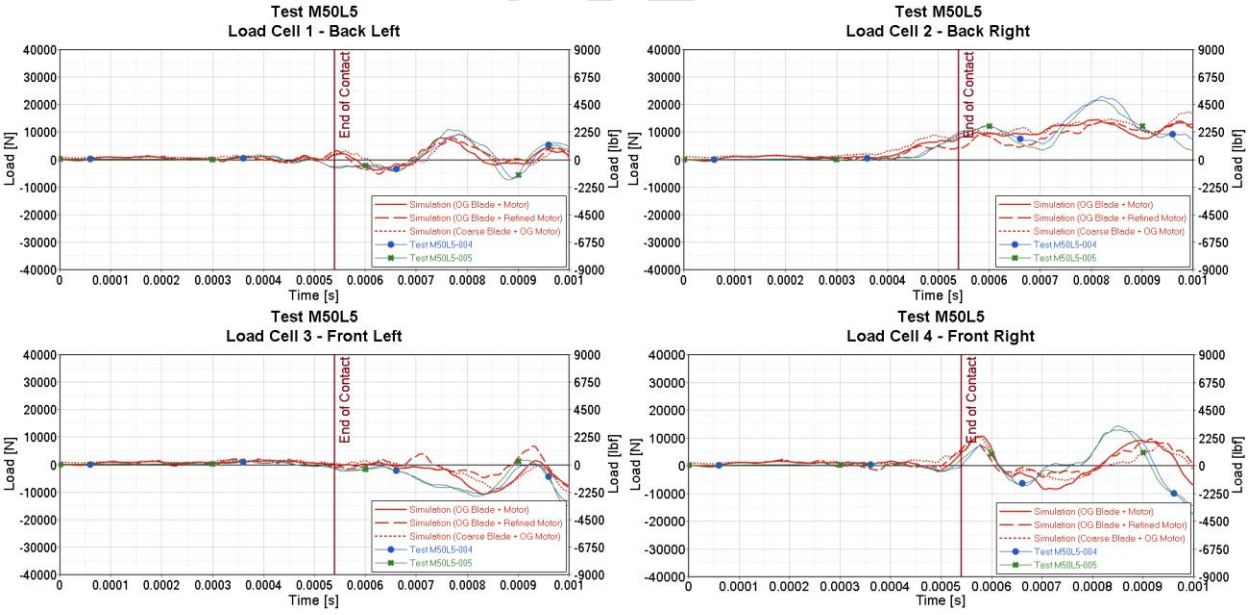

Figure A.6. Test M50L5-004 mesh sensitivity – Load cell correlations

A.3. TEST C80L7-014

Figure A.7 shows the mesh sensitivity study for test C80L7-014 with three different mesh density setups. The original mesh blade has six (6) elements through thickness suggested initially by OSU, whereas the coarse mesh blade has three (3) elements through thickness. The camera has the original mesh carried over from the A3 program and its refined mesh used for this study.

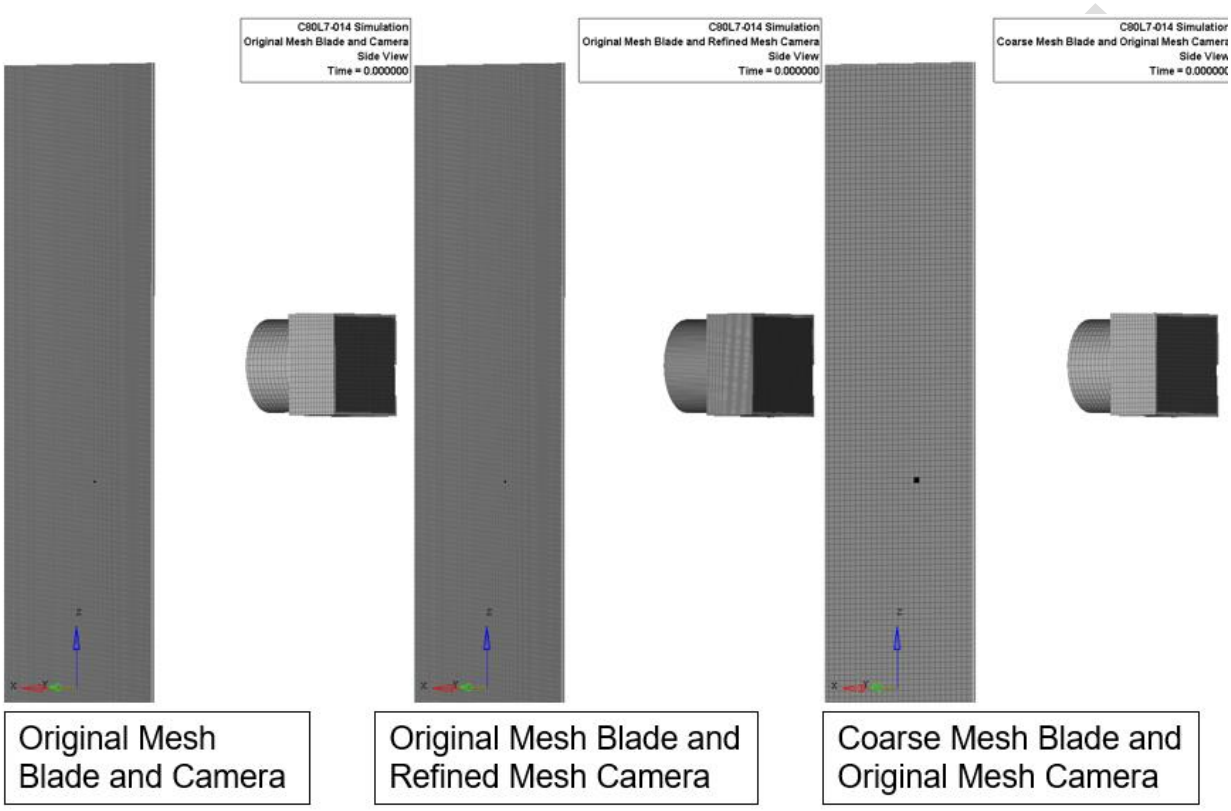

Figure A.7. Test C80L7-014 mesh sensitivity study – FE model setups

Figure A.8 compares the final blade damage between the three FE setups and the physical blade. There was a small visible tear observed on the physical blade's LE. The coarse mesh blade and the original mesh camera setup best compare the similar sized tear to the physical blade instead of the larger tears seen in the other two setups.

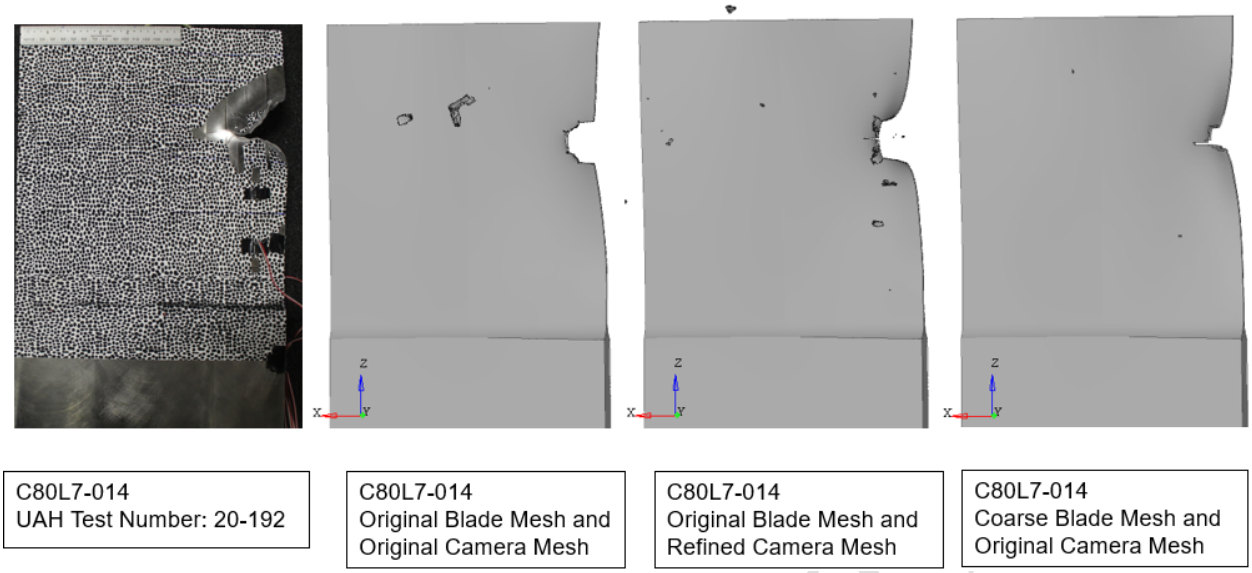

Figure A.8. Test C80L7-014 mesh sensitivity study – Final blade damage

Figure A.9 shows the load cell correlations between the three FE setups and the experimental test results. All three setups agree well with the experimental data. With the results from this sensitivity study, it is concluded that the coarse mesh blade with three (3) elements through thickness and the original mesh camera is the optimal setup because of the most efficient computational time and best final blade damage correlation.

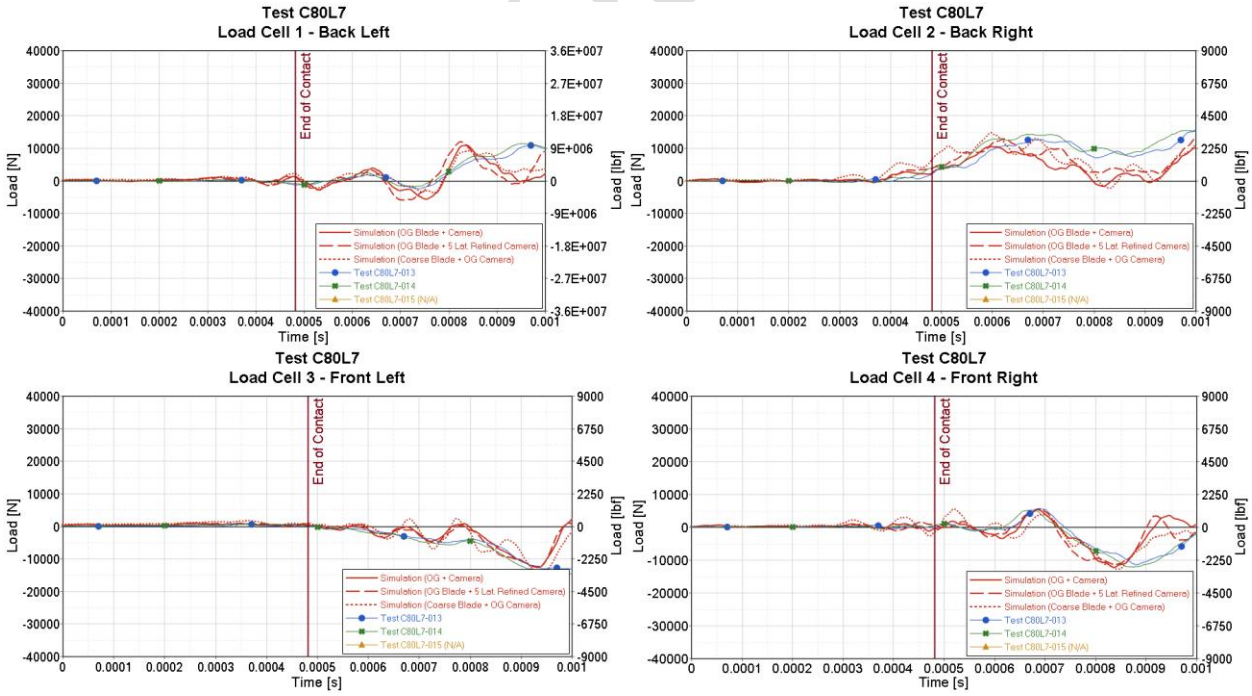

Figure A.9. Test C80L7-014 mesh sensitivity – Load cell correlations

A.4. TEST C50L5-016

Figure A.10 shows the mesh sensitivity study for test C50L5-016 with three different mesh density setups. The original mesh blade has six (6) elements through thickness suggested initially by OSU, whereas the coarse mesh blade has three (3) elements through thickness. The camera has the original mesh carried over from the A3 program and its refined mesh used for this study.

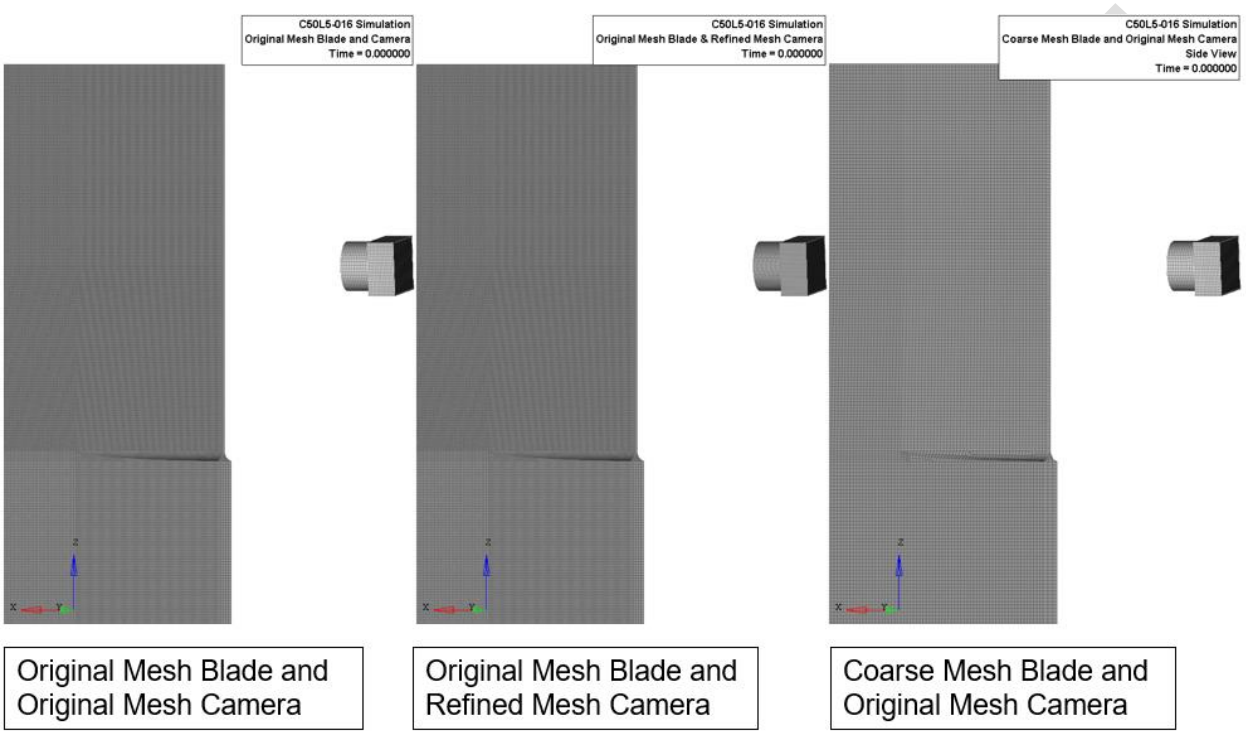

Figure A.10. Test C50L5-016 mesh sensitivity study – FE model setups

Figure A.11 compares the final blade damage between the three FE setups and the physical blade. The coarse mesh blade and the original mesh camera setup was able to capture the line crack observed on the physical blade's LE. On the other hand, the other two FE setups show more conservative blade damage with larger tears in the impact region.

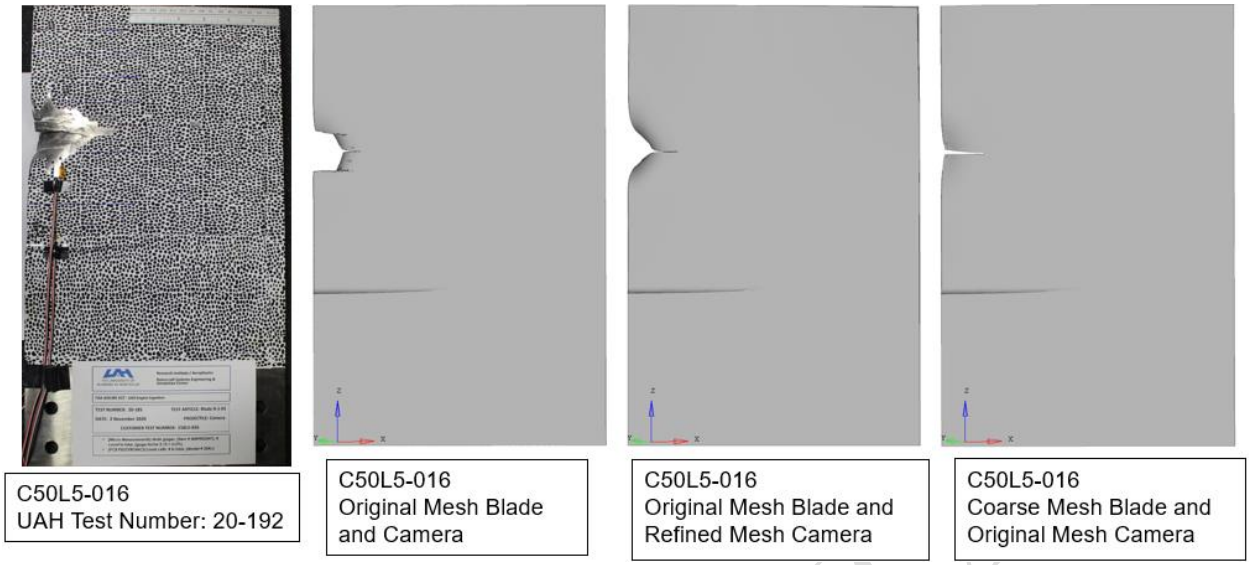

Figure A.11. Test C50L5-016 mesh sensitivity study – Final blade damage

Figure A.12 shows the load cell correlations between the three FE setups and the experimental test results. All three setups agree well with the experimental data. With the results from this sensitivity study, it is concluded that the coarse mesh blade with three (3) elements through thickness and the original mesh camera is the optimal setup because of the most efficient computational time and best final blade damage correlation.

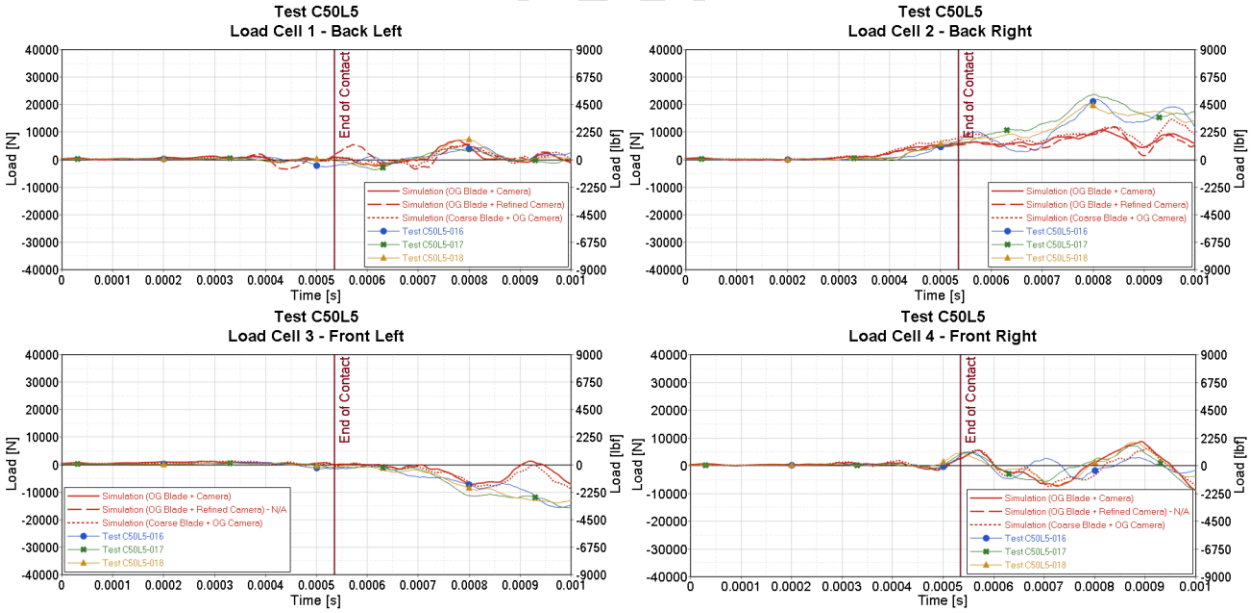

Figure A.12. Test C50L5-016 mesh sensitivity – Load cell correlations

A.5. TEST B80A5-007

Figure A.13 shows the mesh sensitivity study for test B80A5-007 with two different mesh density setups. The original mesh blade has six (6) elements through thickness suggested initially by OSU, whereas the coarse mesh blade has three (3) elements through thickness. On the other hand, the battery only has the original mesh carried over from the A3 program. The battery mesh was not refined to complete this sensitivity study in a reasonable timeframe. Otherwise, its refined mesh would require a much longer timeframe due to the costly computational time and the complexity of the FE battery model.

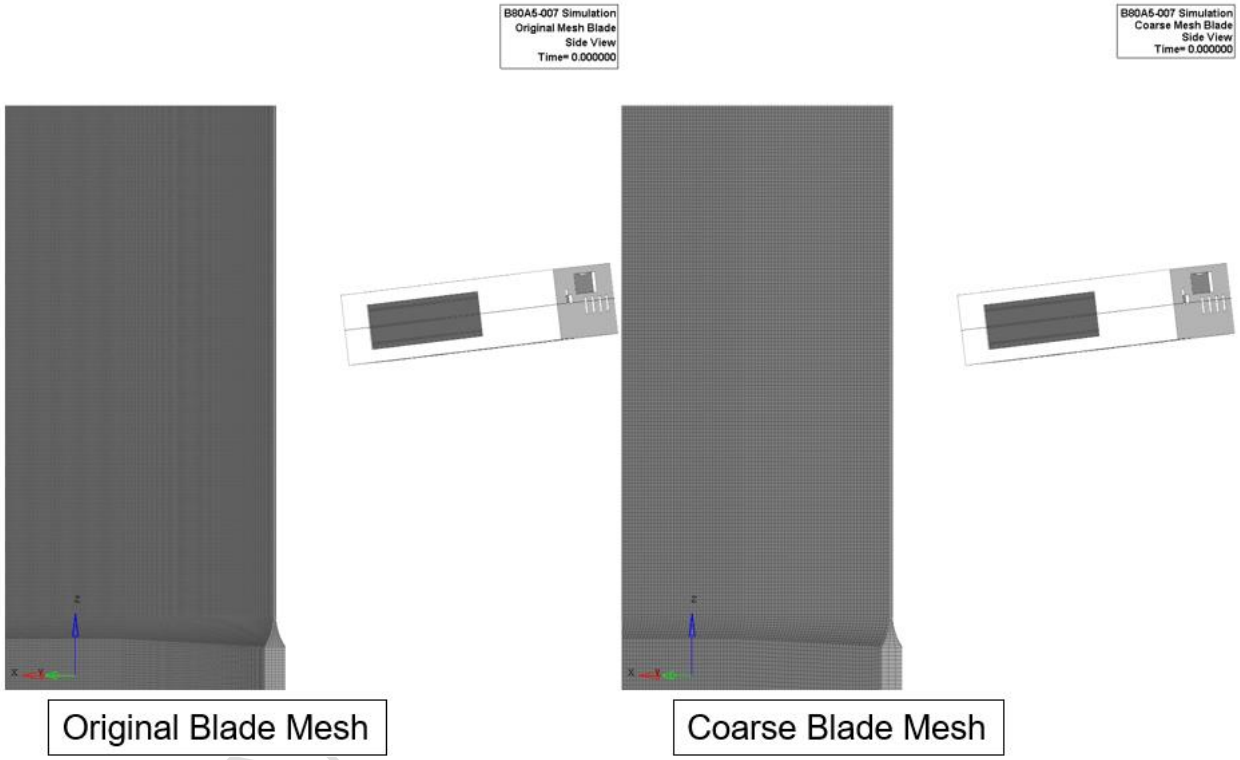

Figure A.13. Test B80A5-007 mesh sensitivity study – FE model setups

Figure A.14 compares the final blade damage between the two FE setups and the physical blade. Both setups were able to capture the bent of the blade to some extent. Since the impact happened near the middle of the downrange face of the blade, there was no damage to the blade's LE observed on the physical blade and the simulated blades in the two setups.

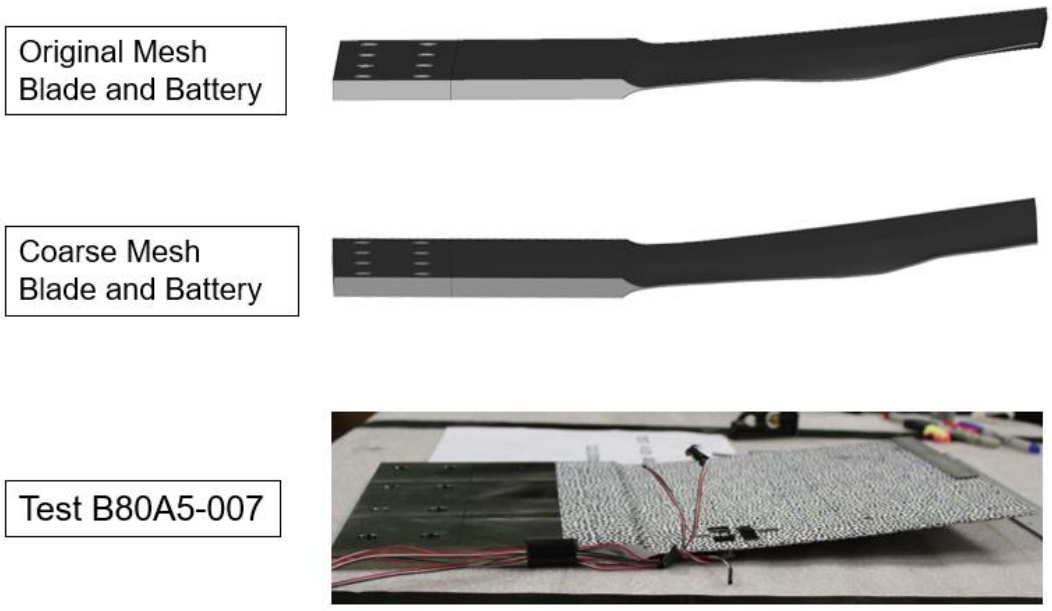

Figure A.14. Test B80A5-007 mesh sensitivity study – Final blade damage

Figure A.15 shows the load cell correlations between the two FE setups and the experimental test results. All the setups agree well with the experimental data. With the results from this sensitivity study, it is concluded that the coarse mesh blade with three (3) elements through thickness and the original mesh battery is the optimal setup because of the most efficient computational time and good final blade damage correlation.

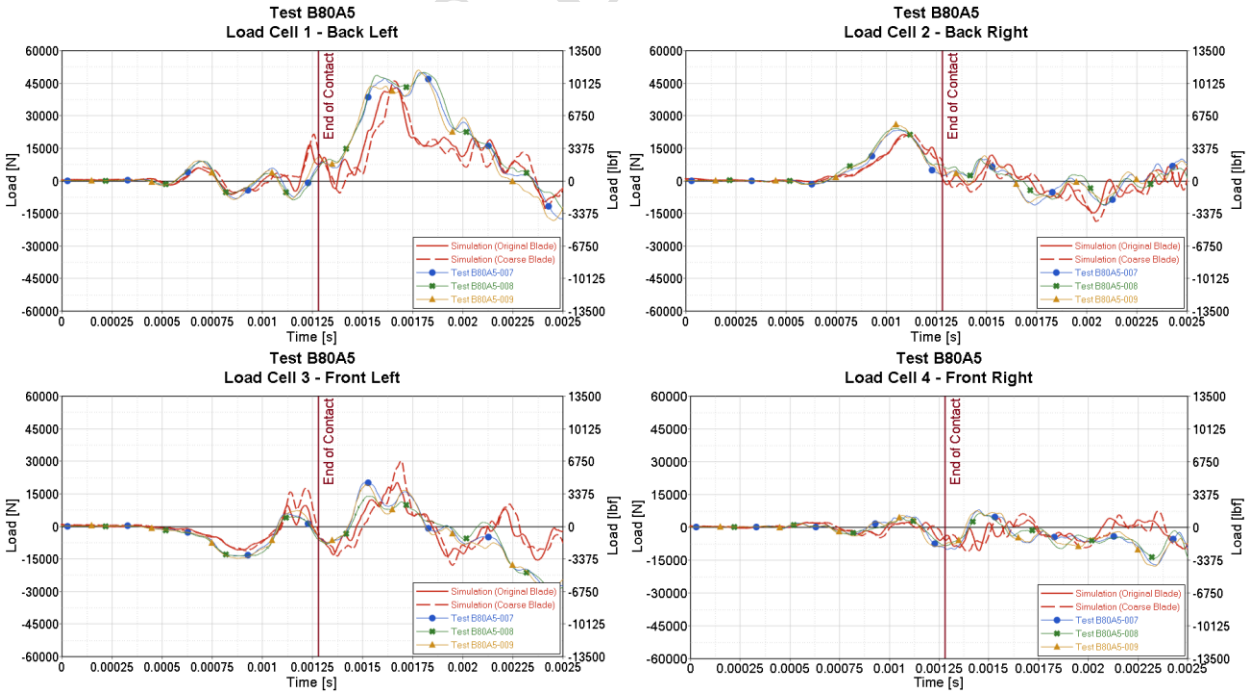

Figure A.15. Test B80A5-007 mesh sensitivity – Load cell correlations

A.6. TEST B50L7-011

Figure A.16 shows the mesh sensitivity study for test B50L7-011 with two different mesh density setups. The original mesh blade has six (6) elements through thickness suggested initially by OSU, whereas the coarse mesh blade has three (3) elements through thickness. The battery only has the original mesh carried over from the A3 program. The battery mesh was not refined to complete this sensitivity study in a reasonable timeframe. Otherwise, its refined mesh would require a much longer timeframe due to the costly computational time and the complexity of the FE battery model.

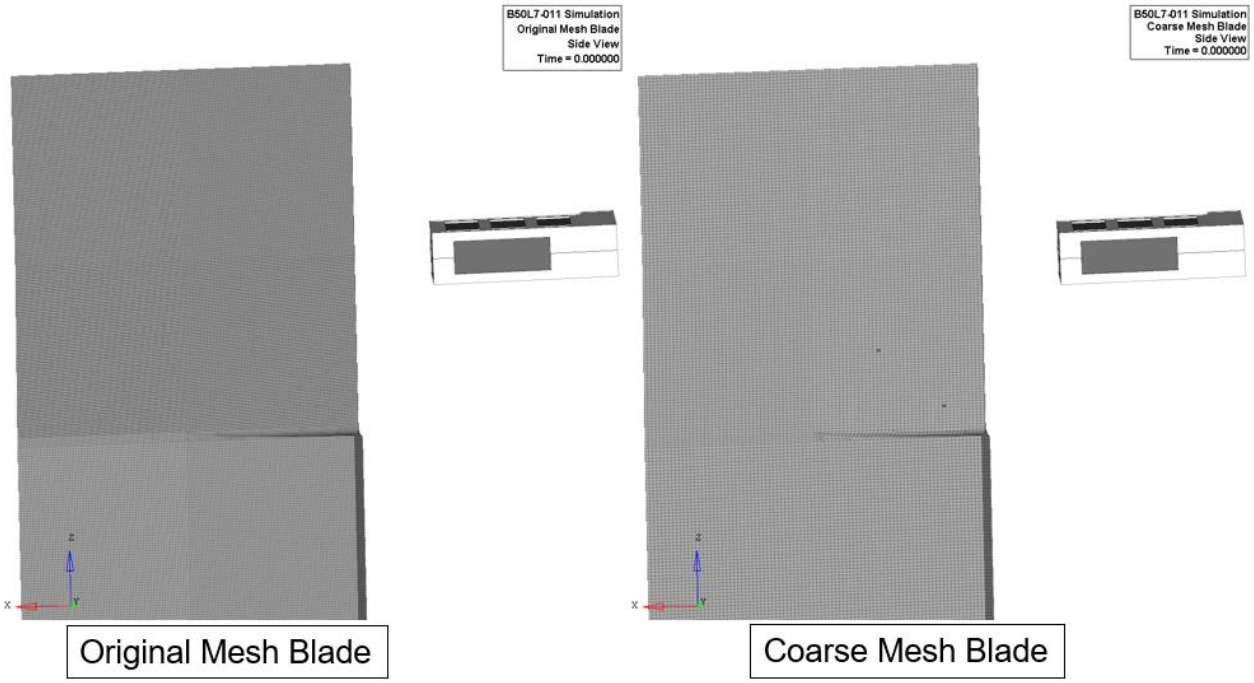

Figure A.16. Test B50L7-011 mesh sensitivity study – FE model setups

Figure A.17 compares the final blade damage between the two FE setups and the physical blade. The coarse mesh blade and the original battery setup was able to capture the initial shear fracture but not the crack propagation path due to mesh size limitation. The other FE setup shows a more significant tear in the impact region but could not capture either the initial shear fracture or the crack path observed on the physical blade's LE.

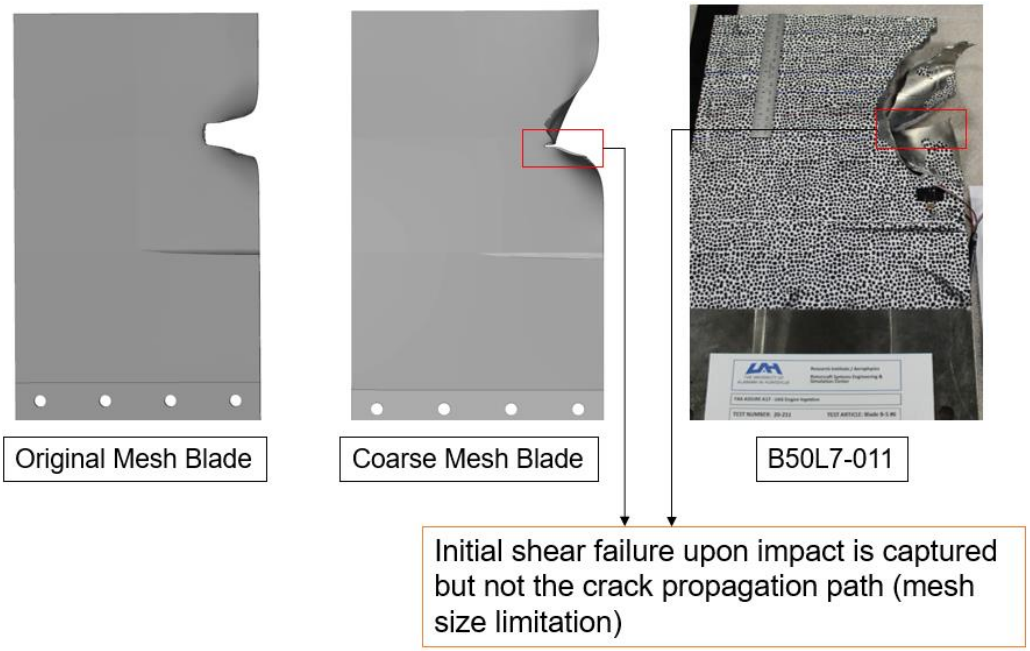

Figure A.17. Test B50L7-011 mesh sensitivity study – Final blade damage

Figure A.18 shows the load cell correlations between the two FE setups and the experimental test results. All the setups agree well with the experimental data. With the results from this sensitivity study, it is concluded that the coarse mesh blade with three (3) elements through thickness and the original mesh battery is the optimal setup because of the most efficient computational time and best final blade damage correlation.

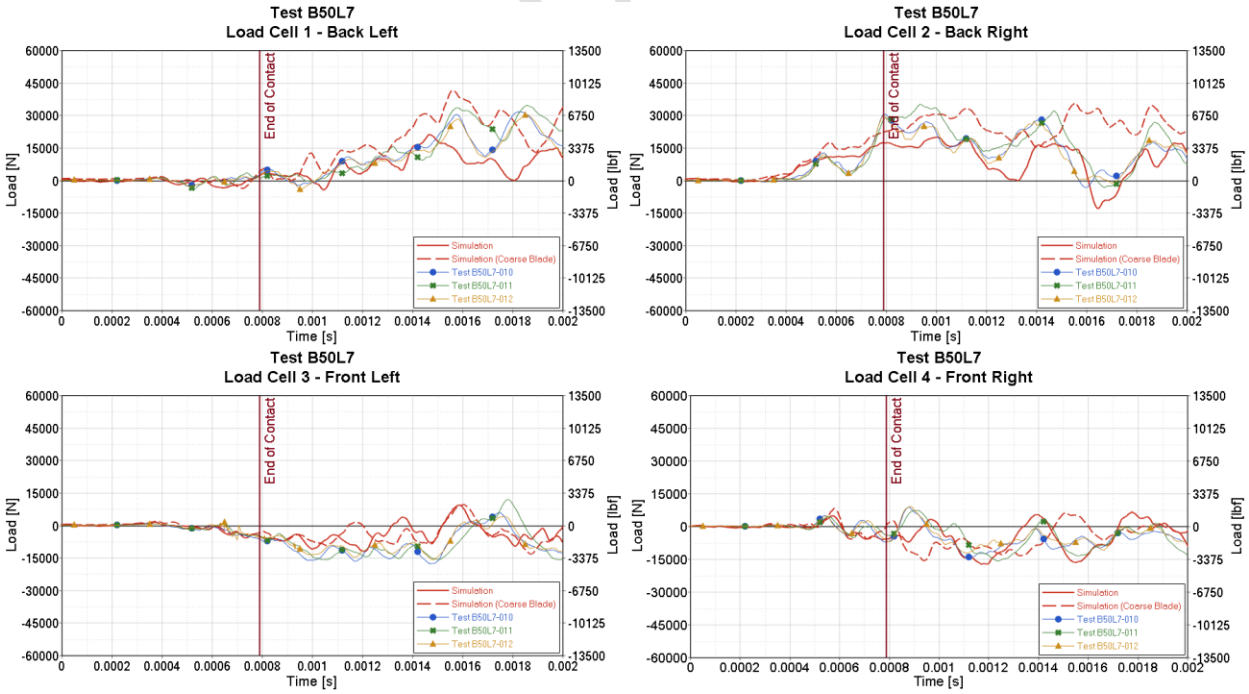

Figure A.18. Test B50L7-011 mesh sensitivity – Load cell correlations

A.7. CONCLUSIONS

The mesh sensitivity study indicated that the target and the projectile mesh must be approximately the same size to achieve good kinematics correlation. In addition, considering the complete engine model studies, the three (3) elements through thickness blade also results in the best option in terms of computationally efficiency (reduced running time). As a result, after agreement from all the parties involved in the research, the coarse mesh blade with three (3) elements through thickness and the original mesh of the sUAS components were selected for the final validation of the component level and full-scale simulations.